January 2017

Investigation Of Rcf Life Of Hollow Components For Additive Manufacturing

Subodh Chandra Subedi

INVESTIGATION OF RCF LIFE OF HOLLOW COMPONENTS FOR ADDITIVE MANUFACTURING

by

Subodh Chandra Subedi

A Thesis

Submitted to Graduate Faculty

of the

University of North Dakota

in partial fulfillment of the requirements

for the degree of

Master of Science

Grand Forks, North Dakota

December

2017

This thesis, submitted by Subodh Chandra Subedi in partial fulfillment of the requirements for the Degree of Master of Science from the University of North Dakota, has been read by the Faculty Advisory Committee under whom the work has been done and is hereby approved.

_____
Dr. Marcellin Zahui (Committee Chair)

_____
Dr. George Bibel (Committee Member)

_____
Dr. Meysam Hagsenas (Committee Member)

This thesis is being submitted by the appointed advisory committee as having met all of the requirements of the School of Graduate Studies at the University of North Dakota and is hereby approved.

_____
Grant McGimpsey
Dean of the School of Graduate Studies

Date: November 2, 2017

PERMISSION

Title	Investigation of RCF life of Hollow Components for Additive Manufacturing
Department	Mechanical Engineering
Degree	Master of Science

In presenting this thesis in partial fulfillment of the requirements for a graduate degree from the University of North Dakota, I agree that the library of this University shall make it freely available for inspection. I further agree that permission for extensive copying for scholarly purposes may be granted by the professor who supervised my thesis work or, in his absence, by the Chairperson of the department or the dean of the School of Graduate Studies. It is understood that any copying or publication or other use of this thesis or part thereof for financial gain shall not be allowed without my written permission. It is also understood that due recognition shall be given to me and to the University of North Dakota in any scholarly use which may be made of any material in my thesis.

Subodh Chandra Subedi
November 2, 2017

TABLE OF CONTENTS

LIST OF FIGURES

LIST OF TABLES

ACKNOWLEDGEMENTS

This thesis document is a record of all work that was performed as a part of my Graduate Studies. It's an evidence to the countless number of hours of research, experiment and writing. It could not have been possible without the generous support and guidance of my advisory committee members Dr. Marcellin Zahui, Dr. George Bibel and Dr. Meysam Haghshenas. I am indebted to Jay Evenstad and Joshua Logan for their help and guidance in making the experimental specimens. I would like to thank everyone at the Mechanical Engineering Department for their assistance during my graduate studies at UND. I cannot thank Dr.Zahui enough, for his time and support during these 2 years. Finally, I would like to thank all my family and friends who have always been there by my side during all this time.

ABBREVIATIONS

σ_a, S	Alternating stress
σ_m	Mean stress value
σ_{max}	Maximum stress
σ_{min}	Minimum stress
$\Delta\sigma$	Stress range
N	Number of cycles
$\in$	Strain
G	Energy release rate
E	Young's Modulus of Elasticity
ϑ	Poisson's ratio
K	Stress Intensity factor
S_e	Endurance limit
S_{ut}	Ultimate Tensile Stress
S_{uc}	Ultimate Compressive Stress
S_{yt}	Tensile Yield Stress

S_{yc}	Compressive Yield Stress
q	Ratio of inside radius to outside radius
P_{max}	Maximum Contact Pressure between the Cylinders
P	Applied Compressive Load
b	Half Contact Width
l	Length of Contact
E_1, E_2	Modulus of Elasticity for the Two Cylinders in Contact
D_1, D_2	Radii of the Cylinders
R_i	Inside Radius of Cylinders
R_o	Outside radius of cylinders
v_1, v_2	Poisson's Ratio for the Cylinders
DfMA	Design for Manufacture and Assembly
DfAM	Design for Additive Manufacturing
AM	Additive Manufacturing
σ_T	Maximum Tensile Stress at the Center of Disc
σ_C	Compressive Stress at the Center of Disc
D	Diameter of the Disc
w	Thickness of the Disc

σ_{rr}	Radial Stress
θ	Angle from Horizontal Axis along which stress is being measured
$\sigma_{\theta\theta}$	Hoop Stress
$\sigma_{r\theta}$	Shear Stress
D_i	Inside Diameter
D_o	External Diameter
r	Radial distance, $R_i<r<R_o$
CS_CH	Circular Specimen with Circular Hole
CS_SH	Circular Specimen with Square Hole
SS_CH	Square Specimen with Circular Hole
SS_SH	Square Specimen with Square Hole
P_{maxFE}	Maximum Contact Stress Calculated by FEA
Δ_{pmax}	Percentage Difference in Contact Stress Values
G_f	Gage Factor
ΔR	Change in Resistance of the Wheatstone Bridge Circuit
R	Resistance of the Wheatstone Bridge Circuit
V_o	Voltage Drop across the Wheatstone Bridge Circuit
V_{in}	Input Voltage to the Wheatstone Bridge Circuit

ΔV	Input Voltage to the Wheatstone Bridge Circuit
Y-axis	Loading Axis
X-axis	Axis Normal to Loading Axis
Side A	Front Side of the Flat Specimens
Side B	Back Side of the Flat Specimens
ECD	Effective Case Depth
RCF	Rolling Contact Fatigue failure
VSR-RCF	Variable Slip Ratio Rolling Contact Fatigue Tester
Ex	Experimental
Fe	Finite Element
Q	Resolution of the Measuring Instrument
E_{FS}	Full Scale Voltage of the Measuring Instrument
$\Delta X = 13$	13mm Distance from the outside edge along X-axis
$\Delta X = 19$	19mm Distance from the outside edge along X-axis
$\Delta Y = 13$	13mm Distance from the outside edge along Y-axis
$\Delta Y = 19$	19mm Distance from the outside edge along Y-axis

ABSTRACT

Advancements in manufacturing and material technology has redefined the approach of design for machine components. Additive manufacturing processes have enabled designers to manufacture for design and functionality. With Design for Additive Manufacturing (DfAM) approach, components can be manufactured with holes in them, including rolling contact components. These hollow components save material, weight, have shorter manufacturing lead times and possibly a higher rolling contact fatigue resistance. Hollowness is defined as the volume percentage of intentional void in load carrying member. Finite element analysis is performed to obtain compressive and tensile stresses on rings and square plates with centric holes in them. The values obtained, are then plotted against the distance from center and hollowness. Observations from numerical analysis are further confirmed with experimental results using strain gages. The results show a moderate increase in strain up to about 20% to 35% hollowness depending on the type of specimen and loading in both finite element and experimental results. Beyond these values, which represent the optimum hollowness, the strains increase along a steep curve. The above results form a basis to examine the effect of hollowness for rolling contact machine elements for their fatigue life. RCF life of solid and hollow discs are examined using theoretical analysis, finite element tools and experiments. The results indicate that some hollow load bearing machine components with enhanced RCF life can be fabricated, leveraging recent advances in Additive Manufacturing.

CHAPTER 1

INTRODUCTION

1.1 Overview

Machines have been in use to human help for centuries now. Discovery of wheel can be taken as the first step in building the first machine, humans ever built. Today, almost every human activity is assisted by a machine, directly or indirectly. Various components in a machine work together to provide an intended output. Each component has its own function and is designed for a specific purpose. A good component design satisfies all the functional requirements by using best suited material, optimum weight, size, shape and product life. Traditional manufacturing processes involve more than one-step to modify the existing stocks to obtain a final product. For example, to manufacture a simple cylindrical shaft, a round stock is taken and then reduced to the required dimension by cutting, turning and facing. Manufacturing of components such as gears, bearings, cams etc., that require complex geometrical, mechanical and metallurgical properties involve lot more steps, time, energy and cost. With the advancements in material science and manufacturing technology,

improvements in design have significantly reduced the size and weight of machines. Bulkier engines have become compact with higher power, efficiency, and sophistication. Tasks that required heavy machines can now be accomplished with lighter and smaller but better efficient machines.

High density aluminum wing panels are being replaced with light weight carbon fibers on airplanes, storage hard disks of megabyte sizes that required a big room to fit in can now be carried in pockets with 1000 folds in their capacity, and conventional farm tractors that required multiple operators can now be easily operated by a single person with the ability to handle multiple operations at once. Making complicated parts have become easier and faster. From conventional manufacturing processes involving casting, shaping, welding and many more to unconventional processes such as laser cutting, plasma arc welding to 3D printing, the evolution in the last decades have been phenomenal. These technologies have enabled manufacturing of complicated parts with utmost precision, unparalleled strength at lower cost and lead times, thus significantly reducing the human effort required. With these innovations in product manufacturing, the design processes have also evolved with time.

Design processes can be categorized based on their purpose. Design for Manufacturing and Assembly (DfMA) simultaneously considers design goals and manufacturing [1]. First it offers guidelines to adapt a design to a given set of downstream constraint which could be related to process, feature or activity [2][3]. Second, it aims to understand and quantify the effect of the design process on manufacturing (and vice versa) [4][5]. Finally, DfMA defines the relationship between design and manufacturing and its impact on the designer,

the design process and design practice [6][7]. These processes and process chains are equally valid for another design approach; Design for Additive Manufacturing (DfAM). There are additional advantages of DfAM such as, there might not be a need for design for assembly, meaning machine components can be designed focusing mainly on the functionality and not on the tooling as it is often the case in gear design. Additive Manufacturing (AM) or 3D printing is the process of joining materials to make objects from 3D computer model data. [8], usually layer upon layer in contrast to subtractive techniques associated with traditional manufacturing processes such as casting, machining, molding etc. Additive manufacturing machines, commonly called 3D printers are now easily available and can print complicated geometry components like gears and cams with utmost precision and accuracy. Thus, any part can now be produced with a single manufacturing process, meaning there is a significant reduction in the material needed and also the number of processes required for manufacture. Processes like drilling, cutting and welding could be easily avoided to produce complicated parts as shown in Figure (1.1) [9].

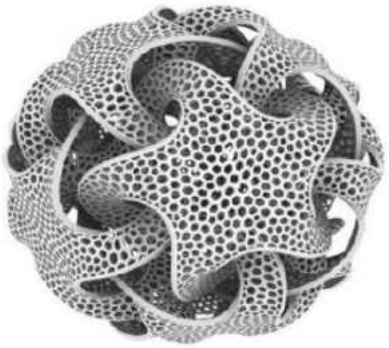

Figure 1.1 Qunitrino Lampshade by Bathsheba Grossman.

3D printing has saved time in product research and development, making it possible to try out different permutations and combinations of design variables to achieve the best output in shortest possible time, effort, material consumption and costs. Apart from their use for rapid prototyping in the last 30 years, they have been used in rapid manufacturing as well [9]. Obvious benefits of this technology are reduction of life cycle, material mass, energy, scrap and harmful auxiliary processes etc. One major advantage of AM is that it has redefined the approach of product design and development. This technology has enabled designers to choose 'manufacturing the design' vs. 'design for manufacturing' approach [10]. Designers are no longer constrained by manufacturing processes and have the liberty to create and manufacture parts that would be more efficient and better at their functionality across all industries including aerospace, biomedical and automotive.

Hollow components such as hollow gears, bearings, cams etc., which were unimaginable, can now be easily designed and manufactured to required precision. They have larger surface areas, allowing lubricants to dissipate more heat from the bodies. In addition, if AM printed, these hollow components could be saving time and cost as well. Though they might not be stronger than their solid counterparts, the benefits of their ability to flex could be used to possibly extend the fatigue life under rolling contact.

As the manufacturing industry is already incorporating Additive Manufacturing into their mainstream production lines, it is imperative to have more test data and experiments for the DfAM approach to be trustworthy. An optimum hollowness based on the weight of the component should be defined prior to their use to leverage the advantages of weight, time, and cost saving. More tests and validation could be significant to finding possible areas of use too. One of such areas would be the manufacture of hollow load bearing components.

1.2 Orientation

This document comprises five chapters that identify the problem, define the objectives and validate the hypothesis with results, and then discuss further course of work. Chapter 1 outlines the differences between Design for Manufacture and Assembly (DfMA) and Design for Additive Manufacturing (DfAM) approaches and provides the background and objectives of the presented research.

Chapter 2 provides a detailed literature review on the study of stresses in hollow components and their advantages in different application. It also discusses various advances in additive manufacturing techniques and material properties for the AM printed components. Current approaches and techniques on the study of rolling contact fatigue are discussed and supporting research in rolling contact fatigue life enhancement are presented. Chapter 3 discusses the Finite Element approach of the work described herein. It comprises all the details about FE models created, their meshing and loading approaches, boundary conditions. The results obtained by FEA are discussed for the strain and contact stress investigation on hollow models. In Chapter 4, experimental approach in determining optimum hollowness in different loading conditions for different specimens is discussed. It details the experimental setup, specimen design and experimental process, and the results obtained while investigating the fatigue failure life for hollow specimens.

In Chapter 5, the results from finite element analysis and experiments are discussed to draw a conclusion from this research. Then, future course of action is outlined with the intended approach and possible areas of application.

CHAPTER 2

LITERATURE REVIEW

2.1 Overview

In this chapter, a comprehensive literature survey on stress and hollowness investigation on rings is presented. It details the existing stress analysis approaches in hollow components, the concept of hollowness, and the work of other researchers that are relevant. It also looks into the possibility of extending the approach of hollowness to load bearing components. Published works of different researchers regarding hollow load bearing components to extend the rolling contact fatigue failure life are discussed. Then, it looks into the current advances in AM processes in reference to the mechanical properties of metals for their suitability towards manufacturing of load bearing components. This chapter thus provides a basis for the thesis with the understanding of existing approaches and work by other researchers.

2.2 Stress in Rings

Not much of an investigation has been done regarding the stress field variation with hollowness of machine components. Circular rings have been studied in greater depths to find the tensile strength of brittle materials such as concrete and rock using a widely known

technique called Brazilian Disc test as shown in Figure (2.1). Brazilian Disc test is an indirect testing method where tensile strength of rocks is determined by the stresses at failure of rings loaded in uniaxial diametric compression. For the normally loaded disk, stresses induced are compressive and tensile along the loading axis and the axis normal to that, respectively. The tensile stress is almost constant near the center of the disk under compression. It is assumed that failure occurs at the point of maximum tensile stress, i.e. at the center of the disc [11], [12]. Eqn. (2.1) is used to calculate tensile stress using the Brazilian Disc test.

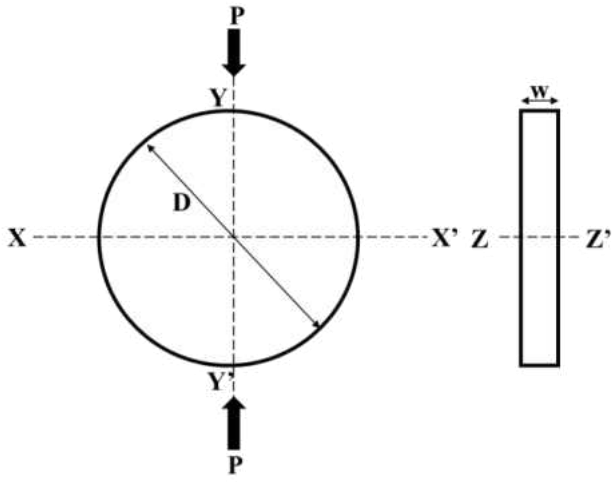

Figure 2.1 Schematics of Brazilian Disc Test.

$$\sigma_T = \frac{2P}{\pi Dw} = 0.636\frac{P}{Dw} \quad (2.1)$$

where,

σ_T is the maximum tensile stress at the center of the disc

P is the applied compressive load

D is the diameter of the disc

w is the thickness of the disc

No specific focus on stress variation with change in size of holes or hollowness were found in literature except for the test for failure of rock samples in Brazilian disc test, thus, all the reference made herein are based on the same. The procedure and results of Brazilian Disc test can be related with the work described in this document as it assumes that even rocks are homogenous, isotropic and linearly elastic before brittle failure occurs [13]. Initiation of crack is considered as a failure criteria and most of the study has been focused on defining the failure criteria based on the location of crack initiation site. Yanagidani et al. [14], Chen et al. [15] have shown that the crack initiation site would be located at the center of the Brazilian disc based on the Griffith fracture criterion. Fairhurst [16], Hooper [17], Hudson et al. [18], Swab et al. [19] have shown that the crack initiation points are located away from the center of the discs. Yanagidani et al. [14] first made use of strain gages to study the stress field on rock samples.

Filon (1924) came up with the methods of calculating stresses in rings that are point loaded on the inside boundary [20]. Stress field on a diametrically compressed circular disc was discussed by Timoshenko in 1951. His results for total stress distribution in hollow rings of unit thickness were based on two assumptions,

i. The surface remains plane and the normal stresses over the cross section is hyperbolic.

ii. The total stresses are distributed linearly.

The results from his work based on these assumptions were good for the stresses along X-axis but gave significant error in predicting the stress along Y-axis for rings [21].

Most of these studies have been used to examine the stress on hollow components or to determine the tensile yield strength of rock samples as in the case of Brazilian Disc Test [11], [12]. Hobbs was skeptical of the results of the test as he observed multiple wedge shaped fractures from close to the loading platens, leading to prior tensile failure along the loaded diameter [13]. To avoid the stress concentration at the disk-jaw interface, he proposed the use of a circular disc with a small central hole. He studied the effect of the size of hole in the stress variation within these specimens and came up with the following equations to determine stress on the discs with holes. The stresses in a ring loaded diametrically are given by Eqn. (2.2), (2.3) and (2.4).

$$\sigma_{rr} = \frac{1}{r^2}\frac{\partial^2(X)}{\partial\theta^2} + \frac{1}{r}\frac{\partial(X)}{\partial r} \tag{2.2}$$

$$\sigma_{r\theta} = -\frac{\partial}{\partial r}\frac{1}{r}\frac{\partial(X)}{\partial\theta} \tag{2.3}$$

$$\sigma_{\theta\theta} = \frac{\partial^2}{\partial r^2}(X) \tag{2.4}$$

Where X is the stress function assumed by Filon and defined in the his paper [20].

r is defined as $R_i > r > R_o$ where R_i is the inside radius and R_o is the outside radius of the ring

σ_{rr} is the radial stress

θ is the angle from the horizontal axis along which stress is being measured

$\sigma_{\theta\theta}$ is the hoop stress

$\sigma_{r\theta}$ is the shear stress

For a disk as shown in Figure (2.2), with central hole radius R_i, external radius R_o, thickness w being compressed along the vertical diameter with a load of P, the maximum tensile stress σ_T along $\theta = \pm\frac{\pi}{2}$ and maximum Compressive stress σ_C at $\theta = 0\ and\ \pi$ are approximately given by,

$$\sigma_T = \frac{P}{\pi R_o w}(6 + 38q^2) \quad (2.5)$$

$$\sigma_C = \frac{P}{\pi R_o w}(10 + 10q^2) \quad (2.6)$$

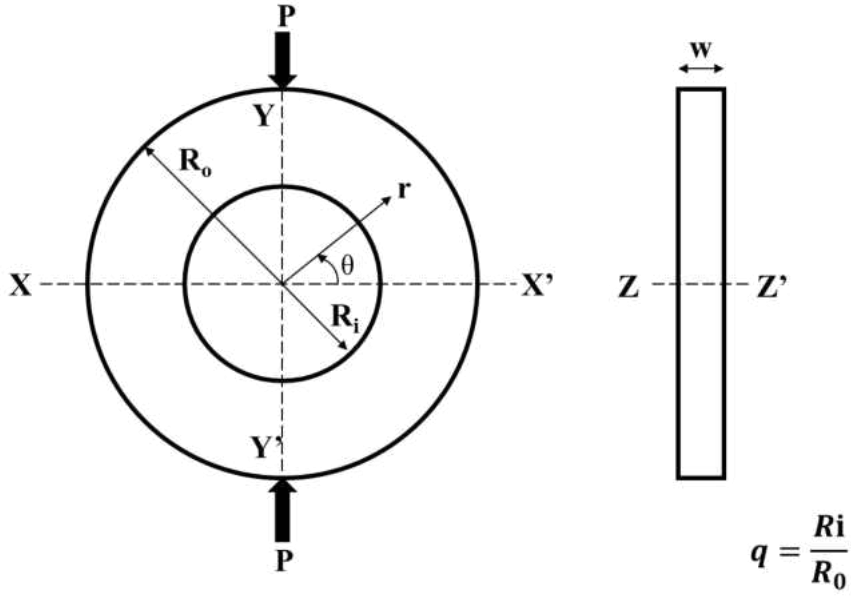

Figure 2.2 Ring under Normal Diametric Compressive Loading.

where q is the ratio of internal to external radius [13]. Kourkoulis and Markides [22] concluded that the stress field strongly depends on the kind of externally imposed load that influences the results, when inner radius approaches the outer one.

2.3 Hollowness of Components

Load bearing components such as gears, shafts, bearings are critical components in machine design. A precise selection of size, material, mass and shape is necessary for proper functioning and utmost efficiency. Hollow components are obviously lighter and susceptible to collapse under different loading conditions. These components on the other hand, could possibly minimize inertial mass, reduce material consumption, increase power efficiency and durability, and provide larger surface areas for cooling.

Hollowness has mostly been defined for cylindrical roller bearing as the ratio of inside diameter to outside diameter. Researchers have defined optimum hollowness for these cylindrical hollow bearings that have maximum rolling contact fatigue failure lives. Darji and Vadkharia [23] have defined optimum hollowness for cylindrical rolling element of bearings based on finite element simulation for minimum contact stress and longest fatigue life under normal loads. They have found that fatigue life for the cylindrical bearings under normal load is maximum in between 60% to 70% hollowness. This corresponds to 36% to 49% hollowness in terms of volume ratio of intentional void to the total volume. Jadayil et al. [24] compared the fatigue lives of solid and hollow rollers in pure rolling contact, where rollers were subjected to combined normal and tangential loads. It was found that due to flexibility of hollow cylinders, contact stresses are redistributed, peak stress is decreased and thus fatigue life is maximum at around 60% hollowness. Beyond these values the cylinders become too flexible and compromise their load bearing capacity.

2.4 Fatigue Life

Fatigue is the third most common mode of failure in machine components [25]. Fatigue is progressive and localized damage that occurs when a material is subjected to cyclic loading. Under fatigue, a time varying force causes premature failure of parts, which would otherwise, easily withstand the static load with the same amplitude. ASTM defines fatigue as '*The process of progressive localized permanent structural change occurring in a material subjected to conditions that produce fluctuating stresses and strains at some point or points and that may culminate in cracks or complete fracture after enough fluctuations*' [26]. Machine components like gears, bearings, cams, rails are highly susceptible to fatigue as microscopic cracks initiate and nucleate at the contact surfaces due to cyclic loading. Fatigue failures are completely unavoidable and occur without any prior warning signs so neglecting the probability of fatigue failure might be disastrous.

Fatigue can be classified as high cycle fatigue and low cycle fatigue. Though there is no clear demarcation between the number of cycles, high cycle fatigue tests are usually carried out for 10^7 cycles [27]. The cause for low cycle and high cycle fatigue are different. Low cycle fatigue is due to significant plastic deformation at microstructural level, whereas, localized plastic deformation has no effect in high cycle fatigue. Typical cyclic loading parameters are shown in Figure (2.3).

Exact determination of fatigue life is impossible because of its stochastic nature so, safety factors in designing components do not account for fatigue failure life. Thus, approximate fatigue life can only be defined for the endurance limit of different components based on their loading, work history, surface finish and operating conditions.

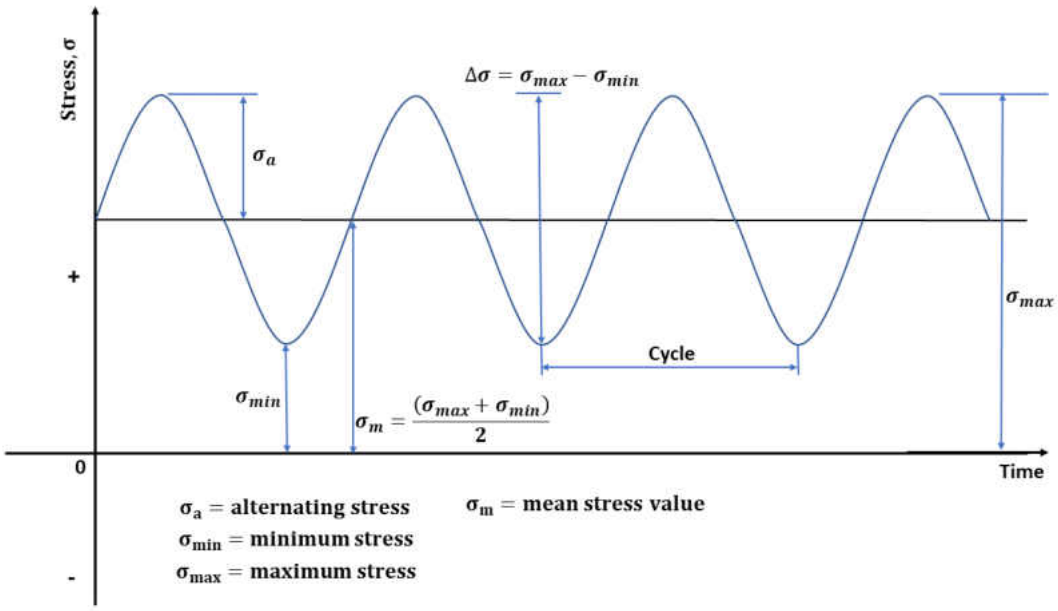

Figure 2.3 Cyclic Loading Parameters in Fatigue Analysis.

2.4.1 Fatigue Life Models

There are different models devised to predict the fatigue life for components based on the type of stress cycles.

A. **S-N model**. Alternating Stress (S) versus number of cycles (N) is plotted on log-log plot to obtain an S-N diagram. It uses nominal stresses and relates these to local fatigue strengths for notched and non-notched members. This is a common model used in the design for infinite life, with an intent to prevent crack growth with strength criterion. It cannot be used to predict fatigue failure life for cases other than those, for which the curve was plotted. It does not account for low cycle fatigue and also doesn't describe the crack growth.

B. $\in -N$ model. This model is based on strain and is accurate for crack initiation and damage prediction. It is used for low cycle fatigue prediction and deals directly with local strain at a notch. This is a complicated approach as it is only used when crack growth and damage assessment is of utmost priority. It allows to integrate the damage due to crack on the material over the time.

C. Linear Elastic Fracture Mechanics (LEFM) model. This model is similar to $\in -N$. It is based on the existing cracks to predict the remaining life of a part, which is predominantly linearly elastic during fatigue. It is very sensitive to the accuracy of stress intensity factor (K) defined by the Eqn. (2.6) and (2.7) as given below,

For plane stress,

$$G = \frac{K^2}{E} \tag{2.6}$$

For plane strain,

$$G = \frac{K^2}{E}(1 - \vartheta^2) \tag{2.7}$$

where, G is the energy release rate, E is the modulus of elasticity and ϑ is the Poisson's ratio.

S-N models are commonly used in fatigue failure life prediction. A typical S-N diagram is shown in Fig (2.4) for UNS G41300, Steel Normalized, S_{ut}=116 kpsi, Maximum S_{ut}=125 kpsi [28].

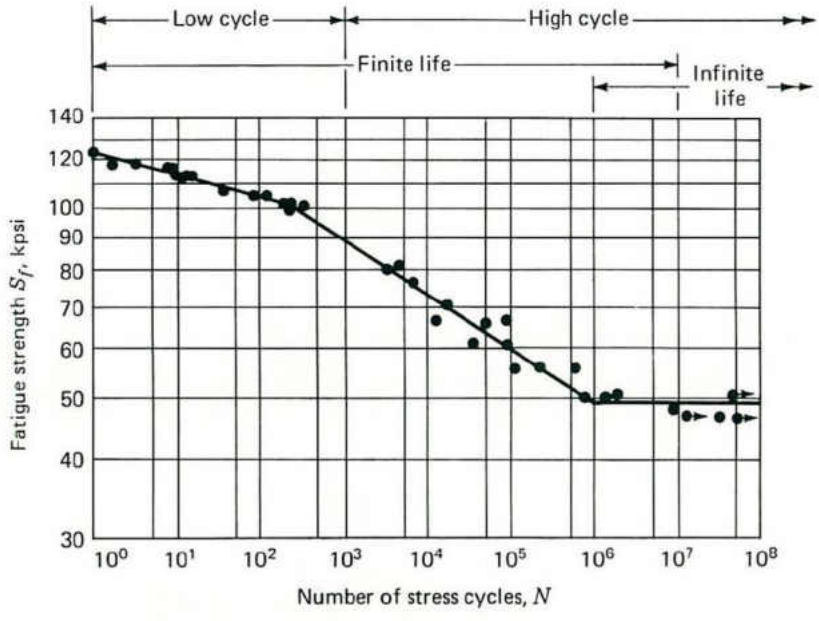

Figure 2.4 S-N Diagram for Completely Reversed Axial Fatigue Tests.

2.4.2 Fatigue Design Criteria

Machine component design under fatigue is defined based on their desired cycle life. They can be categorized as, [25]

A. **Infinite life design**. Local stress or strain induced in the components are essentially elastic and are safely below the pertinent fatigue limit. They are used in design of engine valve springs, railroad axles.

B. **Fail-safe design**. If a part fails, the system does not fail. Fail safe design recognizes that fatigue cracks may occur and structures are arranged such that cracks will not lead to failure of the structure before they are detected and repaired. Multiple load paths, load transfer between members and crack stoppers are built at intervals into the system to achieve fail-safe design.

C. **Damage tolerant design**. This approach assumes that crack will exist and uses fracture mechanics analysis to determine whether cracks will grow large enough to produce failures before they are detected by periodic inspection. It is used for materials with slow crack growth and high fracture toughness.

D. **Safe limit design:** Parts are designed for a finite limit under maximum induced stress. The calculations may be based on stress life, strain life or crack growth relations but the allowable service life is always less than the test life or calculated life. The following methods have been devised to predict the safe limit for fatigue failure in general.

   i. ***Goodman diagram***. For a completely reversed cycle, the safe stress limit is same as the endurance limit. On this diagram, the mean stress is marked along the X-axis while the stress amplitude along the Y-axis. When the amplitude is zero, it is the case of static loading. Lines connecting Endurance limit (S_e) and Ultimate tensile stress (S_{ut}) and Ultimate compressive stress (S_{uc}) are drawn as shown in Figure (2.5). As per the Goodman analysis, safe limit for the stress amplitude designed at Ultimate tensile or ultimate compressive stress is the endurance limit. For all other cases, the same limit lies on the straight line connecting these three points. Goodman diagram provides the safe stress amplitude value for a particular mean stress.

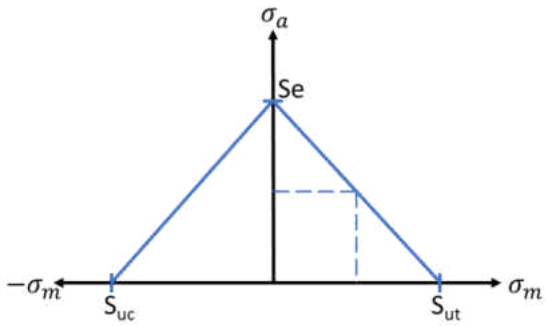

Figure 2.5 Goodman Diagram.

ii. Soderberg diagram. The method for obtaining safe stress amplitude is same as in Goodman diagram, except the ultimate strengths are replaced by yield strength values (S_{yt} and S_{yc}) as shown in Figure (2.6). Goodman diagram is more preferred over the Soderberg diagram.

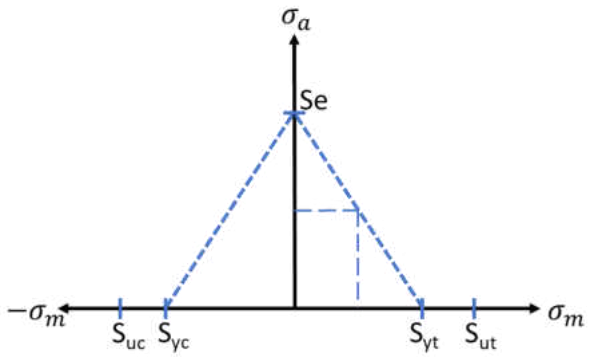

Figure 2.6 Soderberg Diagram.

iii. Modified Goodman diagram. When the stress amplitude nears zero($\sigma_m = 0$), it has been observed that the Goodman line deviates much from ultimate strength values. It almost tends to reach the yield strength values so it is better to modify the Goodman diagram to incorporate this deviation. A line

connecting the yield strength values along the mean stress axis and stress amplitude axis is drawn. Until the intersection of two lines, the safe stress values follow the yield strength line and then, they greatly agree with the Goodman line. This is the Modified Goodman Diagram. Figure (2.7) shows the Modified Goodman Diagram for safe design for fatigue life.

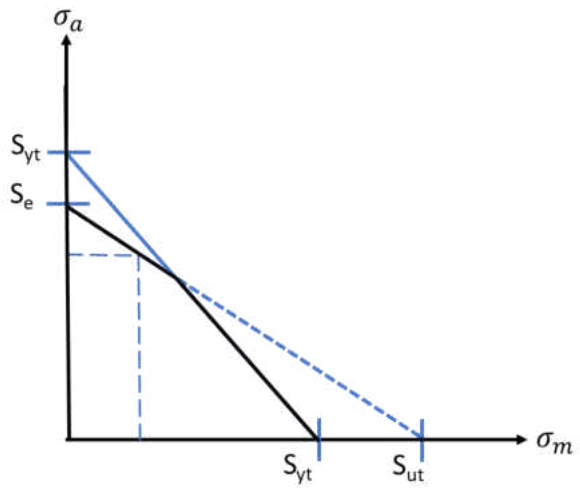

Figure 2.7 Modified Goodman Diagram.

2.4.3 Reasons for Fatigue

As stress fluctuates with time on particular location dislocations, inclusions, and defects reconfigure. Slip is the inelastic shear deformation within metals. Slip occurs when the dislocations move along the slip planes within the individual grains. For softer metals, the dislocation density is low so they have higher mobility. Due to cyclic loading, the dislocation density increases as dislocations, inclusions and defects reconfigure, and thus reduce the mobility within the crystallographic planes, meaning slip is reduced. This leads to hardening of the material, making its cyclic yield strength higher than the monotonic

yield strength. For hard materials, inelastic strain cycling causes the existing dislocations to reconfigure, leading to a higher mobility. Thus, the material softens making its cyclic yield strength lesser than the monotonic yield strength.

Cyclic hardening or softening might occur over a large area or just a localized area with metallurgical discontinuities, inclusions or defects. These act as the areas for crack nucleation or formation. After certain cycles, there is an increase in the number and thickness of slip lines within the metals. This area with concentrated slip lines act as the source of crack in due course of time. These fatigue cracks mostly tend to grow on the plane of maximum shear stress. The rate of growth is dependent on slip characteristics of the material, material grain size and the extent of plasticity near the tip. As the crack tip is confined within a few grain diameters, fatigue crack growth occurs predominantly by a shear process called microcrack growth.

Some cracks nucleate at or near the material discontinuities, on or below the metal surfaces. Discontinuities include pores, inclusions, second-phase particles, corrosion pits, grain boundaries, twin boundaries, voids, and slip bands. These cracks grow to micro-cracks as the slip bands are impinged to the boundary of the discontinuity due to high localized stress [25].

2.4.4 Rolling Contact Fatigue

Rolling contacts are mostly used to transfer high energy with minimal load loss. Load transfer occurs over a very small area making the process highly efficient, though the smaller area of contact results in higher stress [29]. Rolling contact fatigue is defined as

'*the mechanics of crack propagation caused by the near surface alternating stress field within the rolling-contact bodies, which eventually leads to material removal*' [30]. When two surfaces roll cyclically against each other, stresses induced in them change the microstructure in the vicinity of defects/dislocations or any inclusions near the surface. Micro-plastic deformation occurs at areas with microstructural discontinuities such as inclusions or dislocations, leading to a higher resultant stress than the local micro-yield limit at that fatigue cycle [31]. Such areas at the location of maximum shear stress act at the site for crack nucleation. After a number of cycles, this crack grows and reaches the surface, thus breaking off a chunk of material from the surface, causing a failure.

Rolling contact fatigue might occur due to of micropits or macropits. Contact failure modes might be Surface origin (S-O) or Sub-surface origin (SS-O) based on the location of crack nucleation [32]. SS-O failure modes arise from macropits and can be separated into two classes. The two classes are inclusion originated (IO) and subcase fatigue. IO macropits develop in random locations where a defect in the bulk material is present, such as an inclusion or microstructure alteration. Subcase fatigue macropits originate at the interface of the case/core where the case hardness and core strength are lower than the hertzian shear stress field. S-O pits result from asperity (surface roughness changes) and tractive (pulling) forces acting on defects or surface discontinuities on the surface or in the immediate subsurface. The three classes of S-O failure modes are point-surface origin (PSO), Geometric stress concentration (GSC), and micropitting. PSO failure forms random macropits like IO macropits; however, the PSO macropits originate on the surface and have no inclusion as an initiation site. GSC macropits result from misalignments, deflections under loading and contact geometries, which increase the Hertzian stress field at the

surface. Micropitting occurs at low operating speeds when a low viscosity lubricant is used and a thin elasto-hydrodynamic lubrication (EHL) layer is present. The onset of micropitting is a glazed surface due to plastic deformation that contains microscopic cracks. If severe enough, micropitting can lead to macropitting. The failure modes occur when Hertzian stress field is greater than the material's strength. Since the significant stress in contact fatigue is the alternating shear stress, the shear strength of material is important. In pure rolling condition, the plane of maximum shear stress is slightly below the surface but with a sliding condition, the frictional forces and temperature change increase the magnitude and distribution of the shear stress field [33].

2.4.5 Factors Affecting Rolling Contact Fatigue

RCF is a complex phenomenon and is greatly dependent on material properties, operating conditions, work history and the applied loads. These factors can be grouped to into two types,

A. **Process induced factors.** These factors are dependent on the fabrication process of the rolling parts under contact.

   i. ***Surface inclusions and defects.*** Surface asperities, inclusions, defects induced on or below the surface of material during the forming processes act as the site for crack nucleation.

   ii. ***Surface finish.*** A rough surface creates areas of higher stress concentration as well as provide sites for Surface origin cracks for fatigue failure. Also,

during lubricated operation, the lubricant gets trapped in the rough areas and early failure occurs due to wedge action of the trapped liquid.

iii. ***Work history*.** Pre-stressed materials, materials with impurities induced during heat treatment are susceptible to early failure. Insufficient depth of case hardening of materials might result in Subcase fatigue.

B. **Operational and environmental factors**. These factors are based on the operational environment of the rolling components.

i. ***Contact load***. This is the most important factor in contact fatigue. The magnitude of the force determines the stress induced in the contact surface. Contact stress is often called Hertzian stress based on the works of Heinrich Hertz. He studied the effect of material properties and loads on the contacting elastic bodies. Higher the contact pressure, higher is the stress in the components leading to early failure. Hertzian Theory is based on the following assumptions

- Surfaces are continuous and non-conforming (initial contact is a point or line)
- Bodies in contact are elastic.
- Surfaces in contact are elastic and the strain on them is small.
- The contact is non-adhesive.

When two cylinders are in contact and are being axially pressed against each other, the resulting pressure changes the line contact to an area contact. This area is elliptical in shape with a width of $2b$ as shown in the Figure (2.8).When bodies come in contact, complex forces and moments are transferred between

them, making contact stresses non-linear. So, a frame of reference is defined in which the bodies are static and all the calculations are based on this frame of reference. For areas very close to pressure contact, tensile stresses might be induced on compression. When bodies are rolled, these areas are simultaneously in tension and compression, thereby creating a complete reversed cycle of stress. This leads to fatigue in bodies under rolling contact. And higher the stress amplitude, higher is the chance of fatigue.

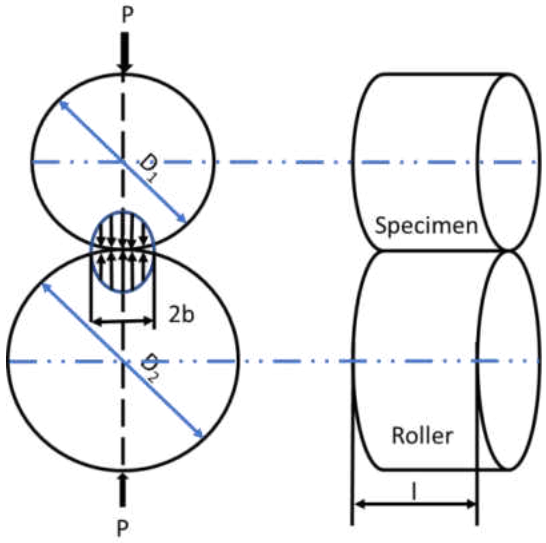

Figure 2.8 Cylinder on Cylinder Contact.

The maximum contact pressure is given by the Hertzian equations,

$$P_{max} = \frac{2P}{\pi bl} \tag{2.8}$$

$$b = k\sqrt{P} \tag{2.9}$$

$$k = \sqrt{\frac{2}{\pi l}\frac{\frac{(1-v_1^2)}{E_1}+\frac{(1-v_2^2)}{E_2}}{\left(\frac{1}{D_1}+\frac{1}{D_2}\right)}} \quad (2.10)$$

where,

P_{max} is the maximum contact pressure between the cylinders

P is the applied force

b is the half contact width

l is the length of contact

E_1, E_2 are the modulus of elasticity for the two cylinders in contact

D_1 and D_2 are the radii of the cylinders

v_1, v_2 are the Poisson's ratio for the cylinders

ii. ***Slip ratio.*** It is the ratio of surface velocities in contact. A zero-slip ratio indicates, that the bodies are in a perfect roll. Difference between the velocities creates a difference in the number of load cycles on the components in contact.

iii. ***Lubrication.*** Influence of lubricant on RCF mechanism is difficult to determine due to a large scatter of data in RCF life. Lubricants act as coolants and dissipate the heat induced during the rolling contact. In case of dry operation, surfaces rub against each other causing large wear and tear, leading to early failure. Generally, lubricants reduce the friction and wear by

interposing a film of oil between the contacting surfaces. In cases where tribofilms are formed, they effectively prevent the initiation and propagation of RCF crack by acting as a barrier between the rolling bodies. Presence of solid particles in lubricants however, assist development of abrasive wear. Lubricant might help in the crack propagation and pitting on the surface due to wedging action of the entrapped fluid in cracks to prevent large scale damages as compared to dry conditions. The nature of fluid film determines the effectiveness of lubrication in rolling motion. For rolling contact fatigue, ElastoHydrodynamic Lubrication (EHL) is preferred as it reduces the direct metal on metal contact.

2.4.6 Rolling Contact Fatigue of Hollow Components

Ever since the identification of RCF as a major cause of rail-wheel failure, significant number of researchers have tried to understand and explain the mechanism, and ways to predict and prevent rolling contact fatigue failures. Lundberg-Palmgren [34] investigated the failure life of rolling elements (rollers or balls) and derived the first relationship between individual component lives and system life, using the Weibull distribution curve. Zaretsky [35] simplified the Lundberg-Palmgren theory to relate rolling element fatigue life with the maximum stress. Ioannides and Harris in 1985 modified the Lundberg-Palmgren theory and tried to fix the shortcomings of the theory. Ioannides and Harris believed that most part of the bearing life is consumed during the crack initiation stage and the crack propagation stage is relatively short [36]. Ioannides and Harris defined a fatigue

limit, for a stress level below this limit, bearings will have infinite life. Lundberg-Palmgren theory is only valid for a perfect geometry and for normal contact between components whereas, Ioannides and Harries theory defines a risk volume that considers stress values at any depth for a defined fatigue limit.

Numerous attempts have been made to investigate the effects of hollowness in load bearing components regarding their fatigue life. Hollowness has been defined by different researchers as the ratio of inside radius to outside radius for cylindrical bearings. Effect of hollowness in load bearing components were first studied by Hanau [37]. Harris [38] patented hollow bearings for their superior benefits over the solid ones. Bowen and Bhateja [39], through their experiment concluded that the best hollowness for roller could be between 60 to 70%. Murthy and Rao [40] used experimental methods to investigate the effect of contact stress on hollow cylindrical elements. They concluded that the outer surface of hollow elements in contact have a maximum contact stress whereas the inner surface is subjected to bending stress. Barabas and Fota [41] have shown that the reduction of inertial mass, decreased material consumption and increased power efficiency make hollow roller advantageous over the solid ones. Darji and Vakharia [23] used finite element method to determine optimum hollowness for cylindrical roller bearings. The bearings were considered elastic and FE models for five different cylindrical roller bearings were created with 10% to 80% hollowness to examine the effect of contact stress on them. They concluded that hollowness is dependent on magnitude of applied load, geometry of roller and mechanical properties of the material. Jayadil and Jabber [42] used FE simulation to obtain stress distribution and then analyzed the results using Ioannides and Harris fatigue theory to estimate the fatigue life of hollow rollers. They conclude that the optimum

hollowness for Hollow contact roller bearings (HCRB) is around 50%. Few of the researchers have attempted to find the optimum hollowness using the experimental methods. More experimental data is needed to validate the hypothesis that hollow machine components under rolling contact have higher fatigue life than the solid ones.

2.5 Additive Manufacturing of Load Bearing Components

Additive manufacturing has been in use for quite some time now. It is mostly used in industries that focus on highly customized parts for specialized applications, especially in the medical arena [43]. From polymers and ceramics to metals and structural materials, 3D printing technologies have evolved greatly over the last decade in terms of printable materials.

Though there are challenges that come up with the layer-wise manufacturing of metals such as thermal stress gradient, microstructure size, density, defects and voids, rough surface finish, AM metallic specimens have shown promising results. Setup costs make up the highest amount for AM (Laser additive manufacturing) whereas the manufacturing costs for mass produced parts would reduce by a significant percentage [44].

Merklein et. al. [45] pointed out that AM printing of metals using laser beam melting has a very high potential, but also needs more research to optimize the technology. The grains of metals used in AM increase the strength in the as-build case [46]. Luecke and Slotwinski [47] studied the mechanical properties of AM Stainless steel and concluded that the tensile properties of AM printed steel are lower than the structural alloys but hardness is uniform across the built surface.

Functionally, AM metallic components exhibit comparable mechanical properties, as do the conventionally manufactured parts as evident from Figure (2.9) [48]. Also promising results have been obtained for fatigue lives between the machined and as-built specimens at High Cycle Fatigue, observed by Yadollahi and Shamsaei [49] meaning, AM parts performed equally well as the machined ones. Figure (2.10) shows fully reversed uniaxial fatigue stress life data for L-PBF Inconel 7018 in machined and as-built conditions at room temperature [50]. Bai et al. showed that AM printed T6 2219-Al exhibited comparable strengths to the conventional casting Al [51]. These studies indicate a possibility of AM printing of hollow load bearing components such as gears and bearings. This could revolutionize the design process and transform the manufacturing industry.

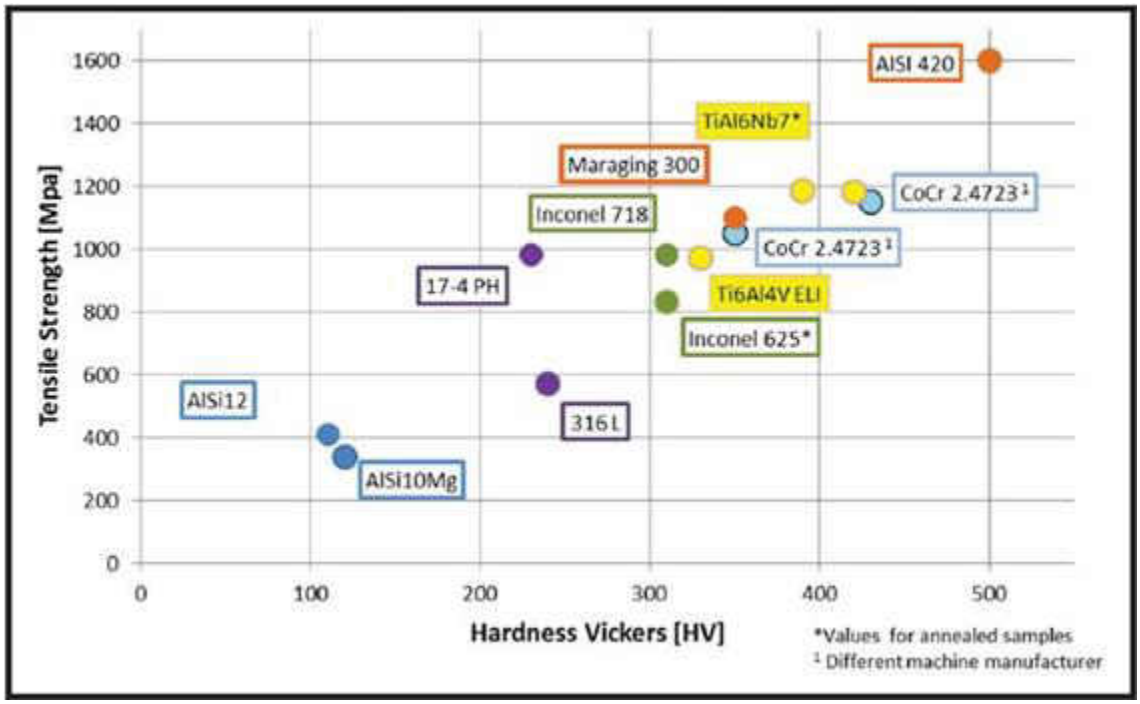

Figure 2.9 Mechanical Properties for Different AM Printed Samples.

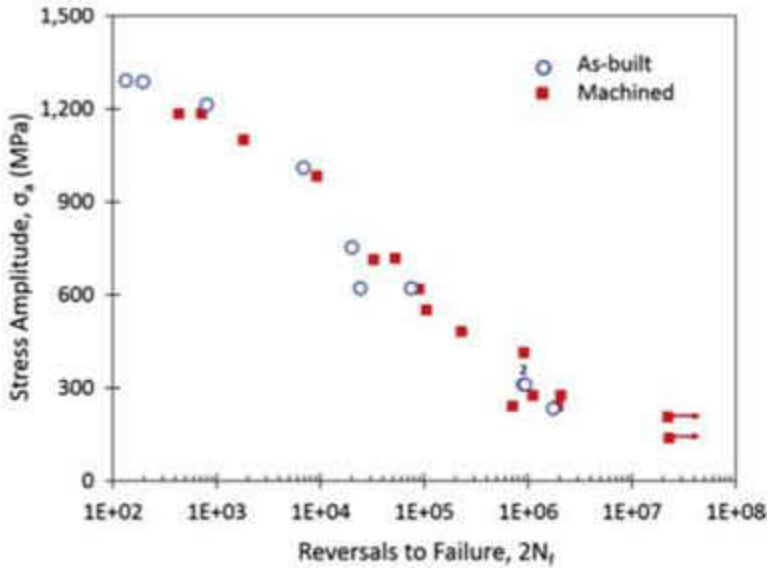

Figure 2.10 Fully Reversed Uniaxial Fatigue Stress Life Data for L-PBF Inconel.

2.6 Objectives

The objective of the work presented here is to examine the effect of hollowness in machine components and define the optimum hollowness of these components as well as Rolling contact components under fatigue loading.

One of the current constrains in part of Design for Manufacture and Assembly (DfMA) approach is that, it hardly supports the manufacture of hollow components to be used instead of solid machine components. Lack of machining ability and insufficient data about the use of hollow machine components, make their use very rare. Load bearing components such as bearings, gears, shafts, cams, wheels could be manufactured with hollow cores and used, if only, their response in terms of functionality and reliability were further studied.

Studies have shown that hollow components are better than their solid counterparts, especially in the case of handling contact stresses. Hollow components can flex under normal compressive loading and thus better distribute contact stresses [23], [24].

With all these probable functional advantages of using 3D printing technology for hollow component design, there is a need to define the limit of hollowness that any of these components can possess and still perform satisfactorily. Hollowness can be defined based on different criteria under consideration. Most of the researchers have defined hollowness for hollow bearing design as the ratio of internal diameter to external diameter of bearings [23], [24]. Hollowness can also be defined as the ratio of hollow cross section area to the total cross section area for slender components. Since the focus of the work herein described is to understand the benefits of using hollow components in terms of material/mass saving, hollowness is better defined in the same way. Hollowness is the mass or volume of material removed from the solid component to make it hollow. Thus, hollowness is defined as the volume percentage of intentional void to the total volume of the component. This definition is valid for any type of geometry and resonates well with the purpose of the work described herein.

Unfortunately, additive manufacturing of metallic parts is relatively new, and there still are challenges to deal with. There have been numerous studies to address the issues of surface roughness, variable density, unavoidable voids, and thermal stress in AM parts [1]. A better understanding of design parameters and testing procedures are needed before load carrying and power transmitting components fabricated with Additive Manufacturing to replace the traditionally manufactured components. The present work is an attempt to examine the effect of intentional void produced with AM process in machine components under contact

fatigue loading conditions. Firstly, it focuses on theoretical and experimental determination of optimum hollowness of rings and square plates with central holes under normal loading. Then, it attempts to extend the concept of optimum hollowness from rings and hollow square plates to load bearing components such as gears and bearings under rolling contact loading. This would open avenues for the DfAM approach in design and manufacturing of hollow components such as Truss Reinforced Gears (TRG) as shown in Figure (2.11).

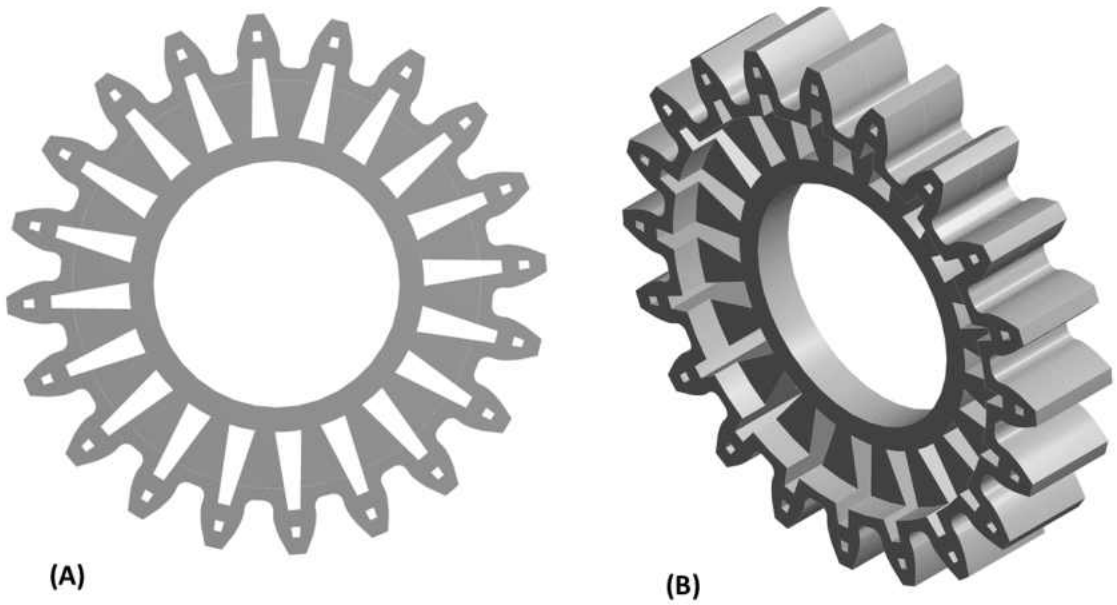

Figure 2.11 Hollow Gears or Truss Reinforced Gears (TRG). (A) Front View of TRG (B) Isometric View of TRG.

2.7 Problem Statement

Load bearing components under rolling contact are often bulkier and are the ones to fail first in a machine. What if, these components, in spite of their complex geometry, could be manufactured with intentional voids in them saving weight, manufacturing lead time, and cost?

In the conventional design process, a designer has to consider manufacturing constraints while designing any part. Significant amount of time and effort are to be invested in determining the manufacturability of a part during the design process itself. What if any components could be manufactured without any constraints on the manufacturing process? This could enable design of components with holes or intentional voids saving considerable amount of material and lead time.

With all these functional advantages of using 3D printing technology in hollow component design, there is a need to define the limit of hollowness that any of these components can possess. Hollowness can be defined based on different criteria under consideration. As described earlier, hollowness can be defined in terms of radius, area, or volume of the voids. What if the geometry of void is different from the geometry of the component? What could be the saving in the mass or material if components are hollow? It is imperative to have a definition of hollowness that is valid for any type of geometry. Thus, the most suitable criteria to define hollowness would be in terms of mass or volume of material removed from the solid component to make it hollow.

The problem is to identify the possible relation between stress and hollowness on any machine component and then define an optimum hollowness for the component based on its ability to perform its functions satisfactorily. Optimum hollowness is the maximum hollowness that any component can have and still satisfy its functional requirements as compared to their solid counterparts. The judgement for optimum is relative and needs a careful investigation of the distribution of stress field on a defined cross section. Since AM components have comparable strength and are at par with the conventionally manufactured components, hollow 3D printed components can be used instead of solid ones. If so, what

could be the maximum hollowness that these components can have? As already discussed, prediction of RCF life for any component is impossible without experimental data. Its dependency on multiple number of variables pertaining to operating condition and process induced parameters creates a lot of scatter in the failure life data. Lack of sufficient data and experimentation is another reason contributing for this process to remain complicated. RCF is the major cause of failure in load bearing critical components so there must be more focused research on ways to alleviate the effects of stress concentration on rolling elements.

As suggested by various researchers, hollow components are believed to have better ability to distribute contact stress. If so, how do they compare with their solid counterparts? How can hollowness be defined? What could be the optimum hollowness of these components in terms of better fatigue life? These are the questions that need to be addressed by the research community before 3D printed hollow bearings can be used in the industries.

2.8 Significance of the Work

The objective of this research work is an attempt to answer some of those questions and determine the optimum hollowness for load bearing components. The works cited above form the basis for the possibility of using additive manufactured hollow load bearing components that have higher rolling contact fatigue failure life than their solid counterparts.

According to the available literature, hollow components have promising strength and durability. Also, with the benefits of time, cost, and material saving, AM technology in rapid manufacturing is the future. This work could provide a ball park value for hollowness of a load bearing machine component, if it were to be made using AM processes

The significance of this work can be summarized as follows,

- Examine the applicability of hollow components against the existing solid machine components under normal loading
- Determine the optimum hollowness of hollow components for defined loads and stress criteria
- Provide experimental verification for the concept of 'Design for Additive Manufacturing (DfAM)' to be used in industry.

The following chapters present theoretical, finite element, and experimental approaches to address these objectives of the research.

CHAPTER 3

FINITE ELEMENT ANALYSIS

3.1 Overview

This chapter deals with the finite element method employed to obtain stress, deformation, and strain values for the specimens. It defines the models for specimens and then discusses the meshing and loading techniques along with the boundary conditions used to solve the finite element model for strain investigation as well as contact stress variation. The finite element models for solid specimens are validated with the theoretical results available in literature and then the same models are extended incorporating varying percentages of hollowness in the models. The results have been presented in form of plots for optimum hollowness of specimens.

3.2 Hollowness under Normal Loading

To investigate the effect of hollowness on different specimens, finite element analysis was performed using ANSYS Workbench®. Wang et al. [52] carried out stress analysis on a flattened Brazilian disc specimen, using ANSYS® but, their intent was to determine the

elastic modulus, tensile strength, and fracture toughness for brittle rocks [52].

3.2.1 Specimen Classification

Finite element models are created in ANSYS®. Normal Stresses and deformation along X and Y axes for 4 types of models were then studied in detail. These models can be categorized based on the following two criteria,

A. **Loading.** The loading techniques on the specimens are different. They can be classified as,

   i. ***Concentrated loading.*** This type of loading is applied on circular specimens where the top plate and bottom plate make line contact along the z-axis, meaning, there is a line of contact between each of the loading plate and the circular specimens as indicated as A and C in Figure (3.1).

   ii. ***Distributed loading.*** There is an area contact between loading plates and specimens for this type of loading. Square Specimens compressed using flat plates are the examples of distributed loading as shown as B and D in Figure (3.1).

B. **Shape of Voids.** The 4 types of specimens can further be categorized based on the shape of their holes giving them hollowness.

   i. ***Concentric regular.*** These specimens have identical shape voids in them as their outer shape. Square specimens with square holes and circular specimens

with circular holes fall under this category. They are presented as A and D in Figure (3.1).

ii. ***Concentric irregular***. The voids in these specimens have different shapes than their outer shapes. Circular Specimens with square holes and Square specimens with circular holes fall under this category. They are presented as B and C in Figure (3.1).

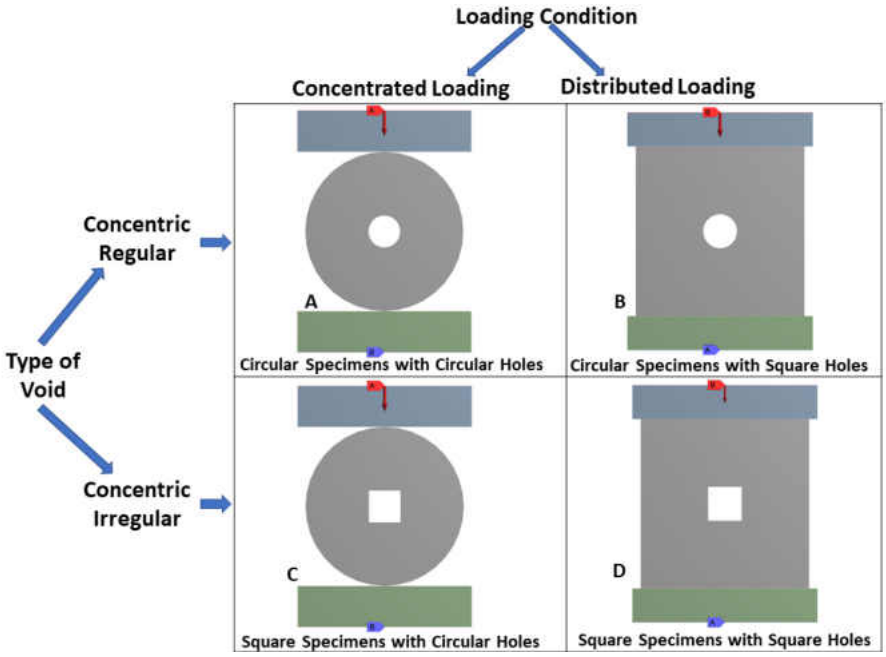

Figure 3.1 Different Categories of Specimens.

3.2.2 Preprocessing

It covers all the preparation needed before the solution of any problem using Finite Element method. It includes modeling, meshing loading and boundary conditions.

A. **Models.** 2D analysis of four types of aluminum specimens was carried out. Circular and Square models with Circular holes or Square holes were built in

ANSYS Workbench®. 2D surface bodies with a thickness of 0.5 inches were created in ANSYS DesignModeler®. The models were made of Aluminum Alloy (Density=2770 kg/m3, Modulus of Elasticity=71 GPa, Poisson's ratio=0.33) whereas the loading plates were made of fictitious high strength steels (Density=7850 kg/m3, Modulus of Elasticity=20,000GPa, Poisson's ratio=0.3). The FE models have been presented in the Table (3.1), where CS and SS represent Circular Specimen model and Square Specimen model respectively. CH and SH indicate the Circular Hole and Square Holes in the models respectively. All of the FE models are shown in Appendix A.

B. **Mesh.** Fine mesh was created on the models using mesh sizing and meshing methods. Convergence of results for FE analysis depends on the quality of mesh on the models. For 2D models, quadrilaterals elements are the best suited ones. Finely meshed models for all four types are shown in Figure (3.2). These models have PLNE183 elements. These are higher order 2-D, 8-node or 6-node elements with two translational degrees of freedom on each of the nodes.

For FEA of the created models, mesh metrics were obtained with small element sizes on the outer and inner edges. These values presented in Table (3.2) are within the recommended range for each of the mesh metrics [53].

Table 3.1 Finite Element Models with Different Hollowness.

S.N.	Cross Section of Specimen	Designation	Outside Dimension (inches)	Hole Diameter (inches)	Percentage Hollowness
1	Square	SS_SH_1	5	0	0.00
2	Square	SS_SH_2	5	1	4.00
3	Square	SS_SH_3	5	1.5	9.00
4	Square	SS_SH_4	5	2	16.00
5	Square	SS_SH_5	5	2.5	25.00
6	Square	SS_SH_6	5	3	36.00
7	Square	SS_SH_7	5	3.5	49.00
8	Circular	CS_SH_1	5	0	0.00
9	Circular	CS_SH_2	5	1	3.14
10	Circular	CS_SH_3	5	1.5	7.07
11	Circular	CS_SH_4	5	2	12.57
12	Circular	CS_SH_5	5	2.5	19.64
13	Circular	CS_SH_6	5	3	28.27
14	Circular	CS_SH_7	5	3.5	38.48
15	Square	SS_CH_1	5	0	0
16	Square	SS_CH_2	5	1	3.14
17	Square	SS_CH_3	5	1.5	7.07
18	Square	SS_CH_4	5	2	12.57
19	Square	SS_CH_5	5	2.5	19.64
20	Square	SS_CH_6	5	3	28.2
21	Square	SS_CH_7	5	3.5	38.48
22	Circular	CS_CH_1	5	0	0
23	Circular	CS_CH_2	5	1	4
24	Circular	CS_CH_3	5	1.5	9
25	Circular	CS_CH_4	5	2	16
26	Circular	CS_CH_5	5	2.5	25
27	Circular	CS_CH_6	5	3	36
28	Circular	CS_CH_7	5	3.5	49

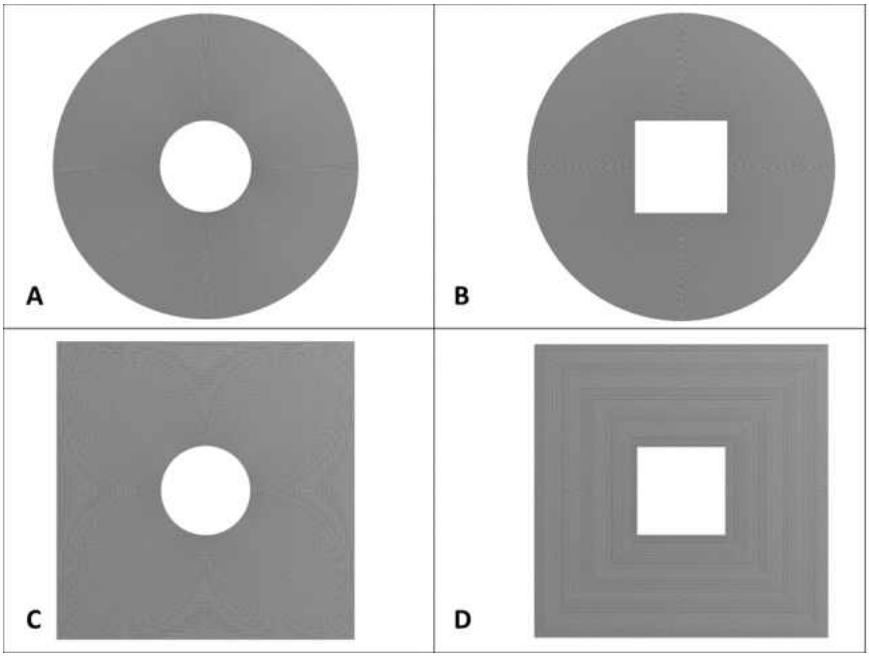

Figure 3.2 Finite Element Models. (A) Circular Model with Circular Holes (B) Circular model with Square Holes (C) Square Model with circular Hole (D) Square Model with Square Holes.

Mesh parameters such as skewness, aspect ratio and orthogonal quality were maintained to the recommended values for all four types of models. Comparative charts for Mesh metric for Circular Specimen with circular holes have been shown in Appendix B as an example. Finite element convergence plots for total deformation for the solid specimen (CS_CH_1) and hollow specimen with 1% (CS_CH_2) have also been added in Appendix C.

Table 3.2 Mesh Metrics for FE Models.

Models		CS_CH (1 to 7)	SS_CH (1 to 7)	CS_SH (1 to 7)	SS_SH (1 to 7)
No. of elements	Max	214589	25468	54962	21031
	Min	13223	10052	8032	7152
Element Quality	Max	0.99	1	0.98	1
	Min	0.92	0.82	0.78	0.81
Aspect Ratio	Max	1.49	1.75	1.91	1.73
	Min	1.09	1	1.11	1
Jacobian Ratio	Max	1.04	1.03	1.07	1.03
	Min	1.01	1	1.02	1
Parallel Deviation	Max	1.32	1.3	2.14	1.08
	Min	0.74	0	0.79	0
Skewness	Max	0.07	0.24	0.31	0.28
	Min	0	0	0.07	0
Orthogonal Quality	Max	1	1	0.99	1
	Min	0.99	0.91	0.86	0.88

C. **Loading and Boundary Conditions.** The Circular and Square models were loaded from the top plate. Load was applied to the upper edge of the top plate. The bottom edge of the lower plate was fixed in all of its DOF to prevent any translation or rotation during loading. The contacts between the plates and models were taken to be bonded. The loading and boundary conditions are shown in Figure (3.3) as an example.

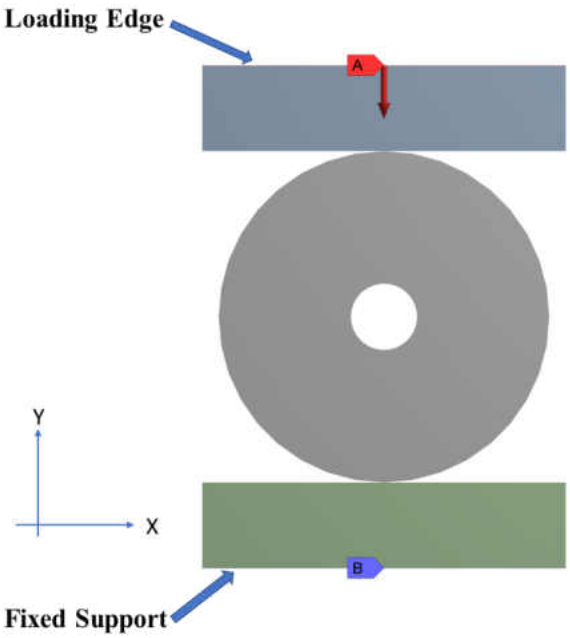

Figure 3.3 Loading and Boundary Condition on FE Models.

3.2.3 Postprocessing

The finite element models were validated using the analytical results from Hobbs' investigation of stress in rings [13]. Figure (3.4) shows a comparison between analytical results and maximum stress along two perpendicular axes in the finite element model for circular specimen with circular holes. Maximum compressive and tensile stress values along loading axis and axis perpendicular to that are compared to the maximum compressive and maximum tensile stress obtained from Eqn. (2.5) and Eqn. (2.6).

After running the solution, the results were obtained for stress, strain and deformations. Two paths were created along the Y and X axes from the outer edge of each model to the center of the models. Equivalent stress, equivalent strain, normal stress, normal strain, total

deformation and directional deformation along these two paths were obtained and the values were analyzed.

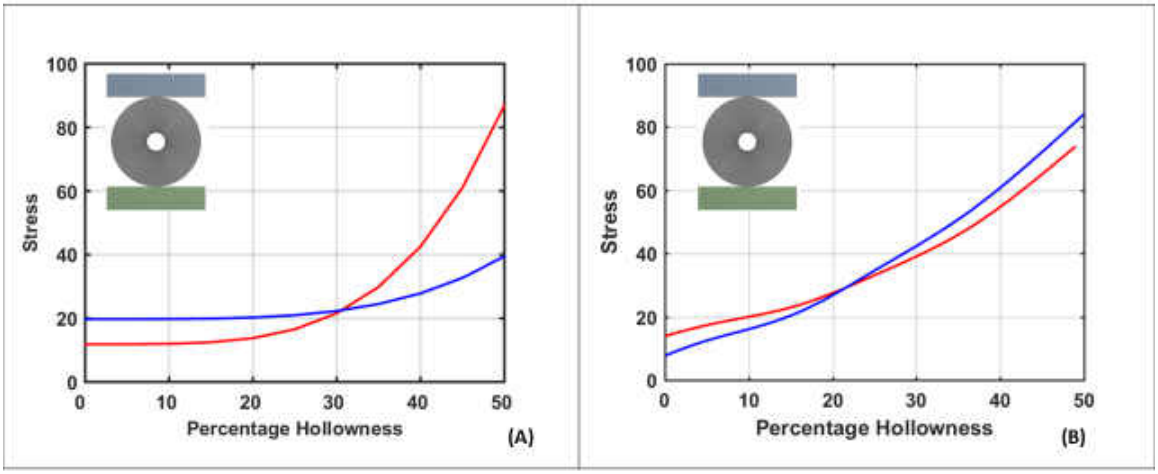

Figure 3.4 Maximum Stress Variation with Hollowness. (A) Results from Hobb's Equation (B) Results from Finite Element Analysis. Red line is for Maximum Tensile Stress; Blue line is for Maximum Compressive Stress.

3.2.4 Results

Results from the FEA of hollow circular disc and square plates are presented herein. Stress and strain values are extracted along the vertical loading axis and the horizontal axis.

A. Stress Variation along Axes. Figure (3.5) to Figure (3.7) show variation of different type of stresses along the two axes due to hollowness in the circular specimens of 5-inch diameter. The stresses are plotted against hollowness percentages in these normally loaded aluminum models. Y is the loading axis whereas X is the horizontal axis. The plots indicate that all types of stresses increase steeply beyond 40% hollowness, meaning the chances of failure is very high

beyond 40% hollowness. Thus, the investigation for optimum hollowness is focused on specimens below 40 % hollowness.

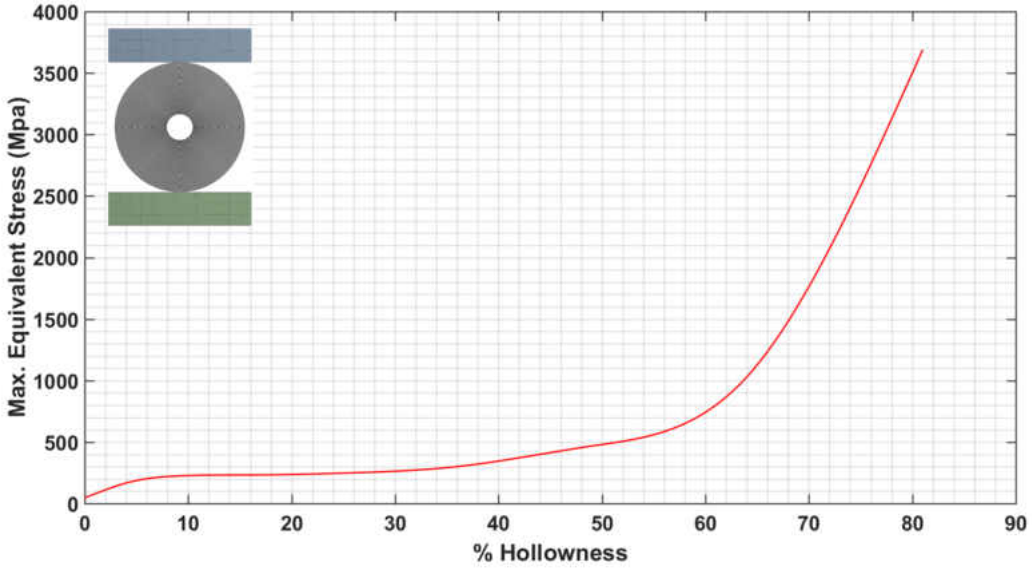

Figure 3.5 Max. Equivalent Stress Variation with Percentage Hollowness.

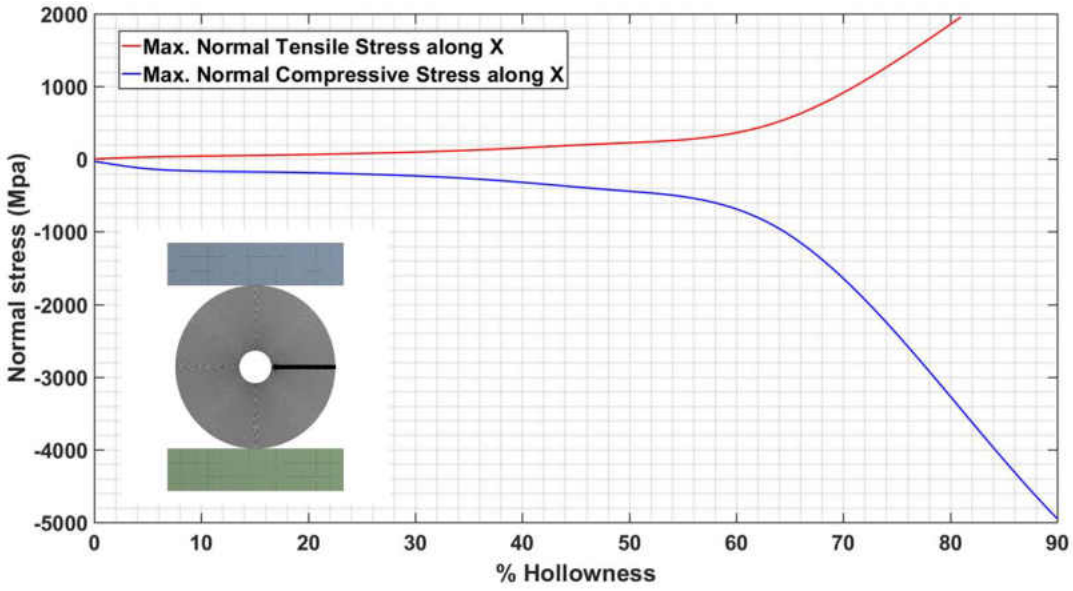

Figure 3.6 Maximum Normal Stress variation with Hollowness along X-axis.

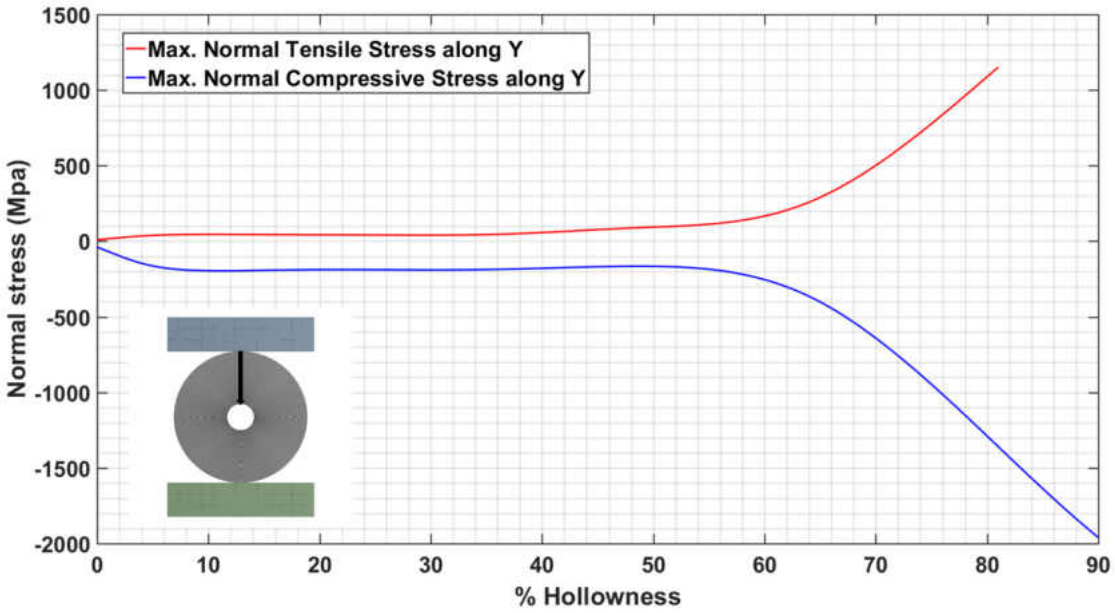

Figure 3.7 Maximum Normal Stress Variation with Hollowness along Y-axis.

B. Stress and Deformation Analysis. Stress and deformation values were analyzed for all four type of specimens from Figure (3.2). All of specimens were compressed with 10kN load along the Y-axis. Stress and deformation values along the Y-axis and X-axis were recorded and plotted against the distance from outside edge to inside edge.

i. Circular Specimen with Circular Holes (CS_CH). Figure (3.8) to Figure (3.11) show stress and deformation variation in Circular Specimens with Circular Holes. The results can be summarized as

- Normal stress along Y is maximum for specimens with solid specimens (0% Hollowness). It is initially compressive, then it rises, goes tensile almost near the inside edge and then drops to zero for all specimens of different

hollowness. As the bending stresses get dominant on the inside edges, stress on the 49% hollow specimen changes to tensile.

- Normal stress along X is maximum for 49% hollowness specimen. The stress is tensile for the solid specimen whereas for other specimens, it is compressive, reaches the peak and then bounces back to zero at the inside edge.
- Maximum deformation along X and Y are both experienced for 49% hollow specimens. The deformation values are almost constant along both the axes.

Figure (3.12) shows the variation of maximum equivalent stress on the specimens. Stress is concentrated at the edges along the Y-axis where the specimens are in contact with the plates. Stress distribution is symmetric along both X and Y-axis but with increase in hollowness, higher stress is observed at the inside edge along X and Y-axis. This could possibly be, due to the bending stress being prominent than tensile and compressive stresses.

Deformation variation for circular specimens with circular holes under normal compressive loading is shown in Figure (3.13). The deformation is symmetric along the loading axis and is minimum at the bottom edge for increase in hollowness. Deformation does not vary much along the X-axis with the change in hollowness.

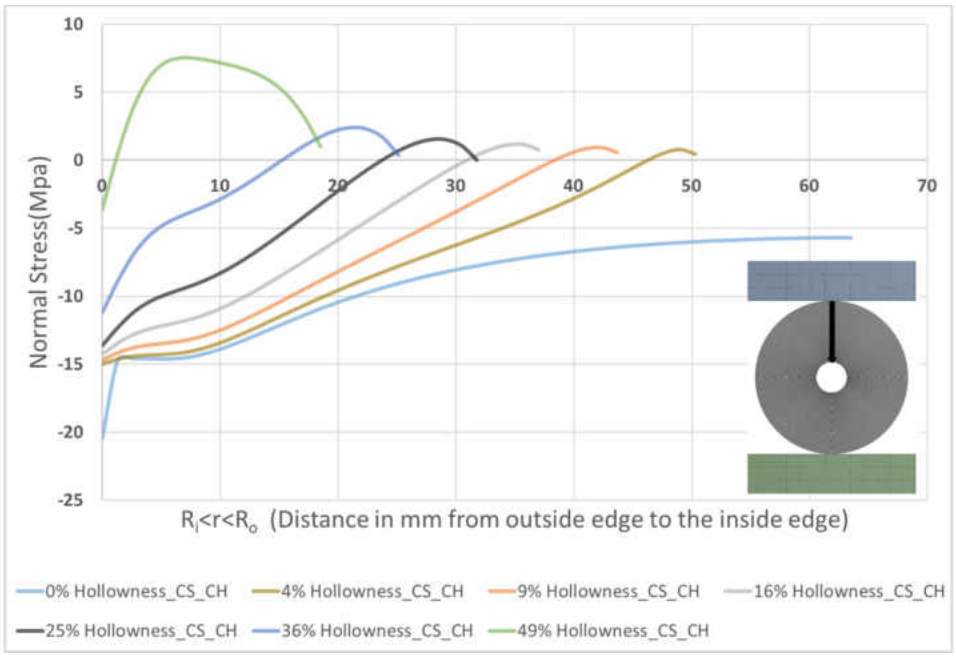

Figure 3.8 Normal Stress Variation along Y

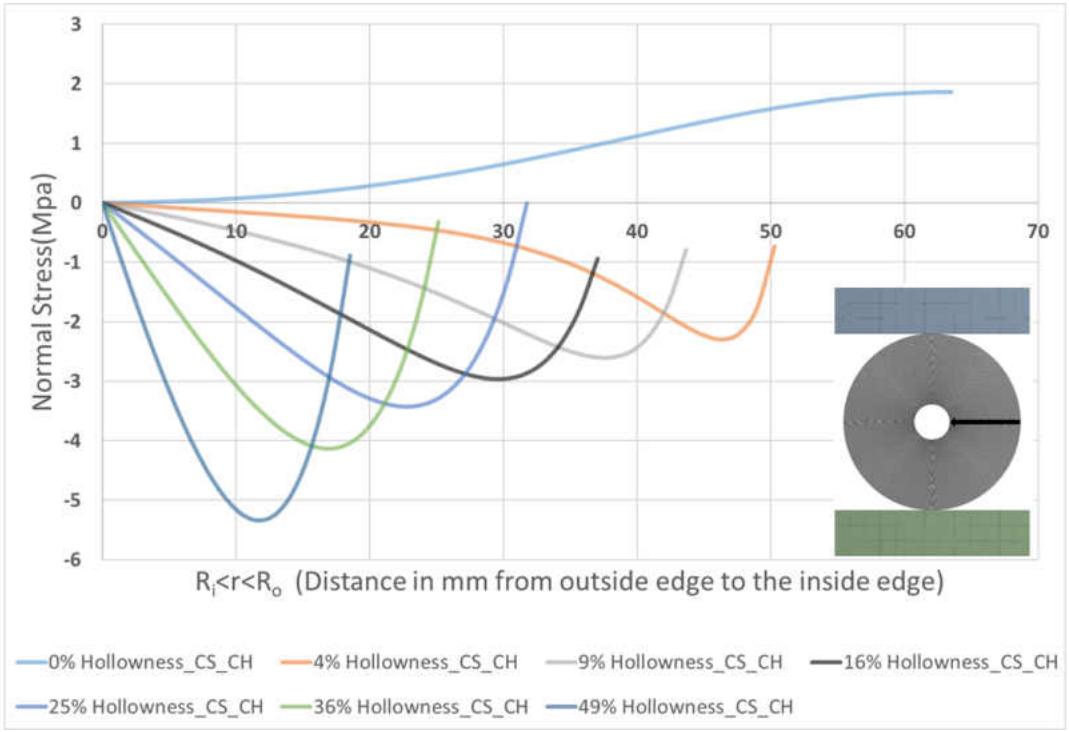

Figure 3.9 Normal Stress Variation along X-axis.

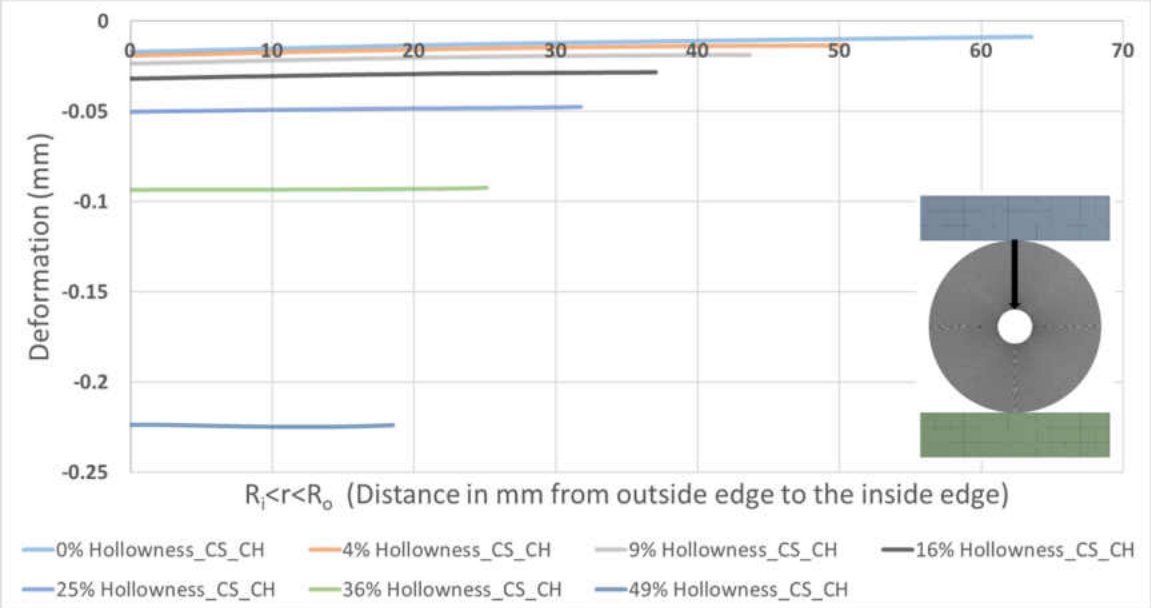

Figure 3.10 Directional Deformation Variation along Y-axis

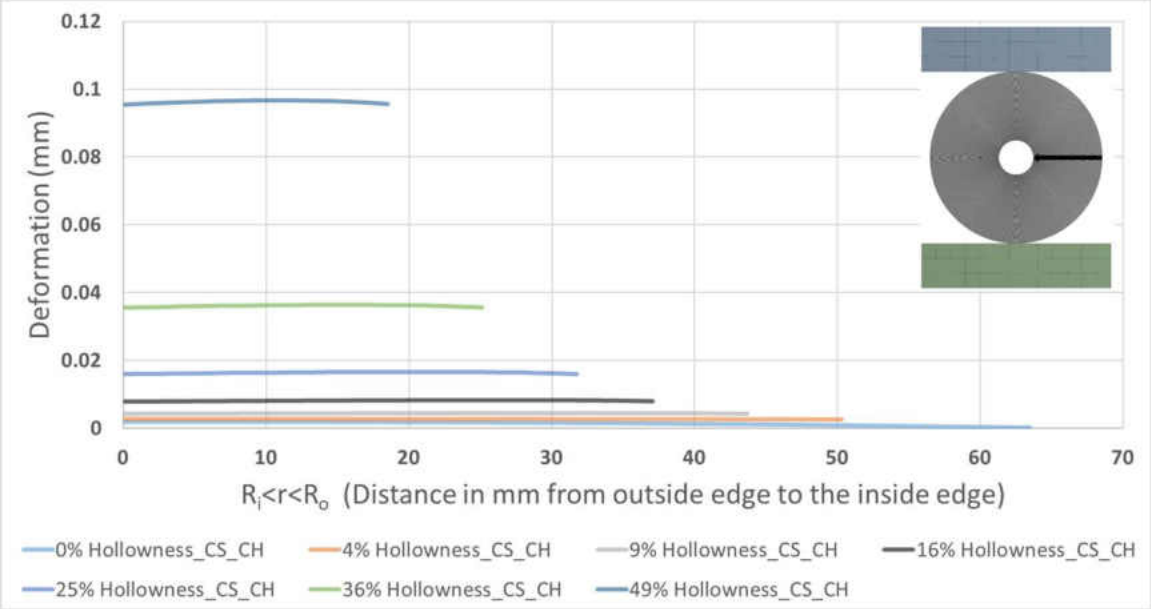

Figure 3.11 Directional Deformation Variation along X-axis.

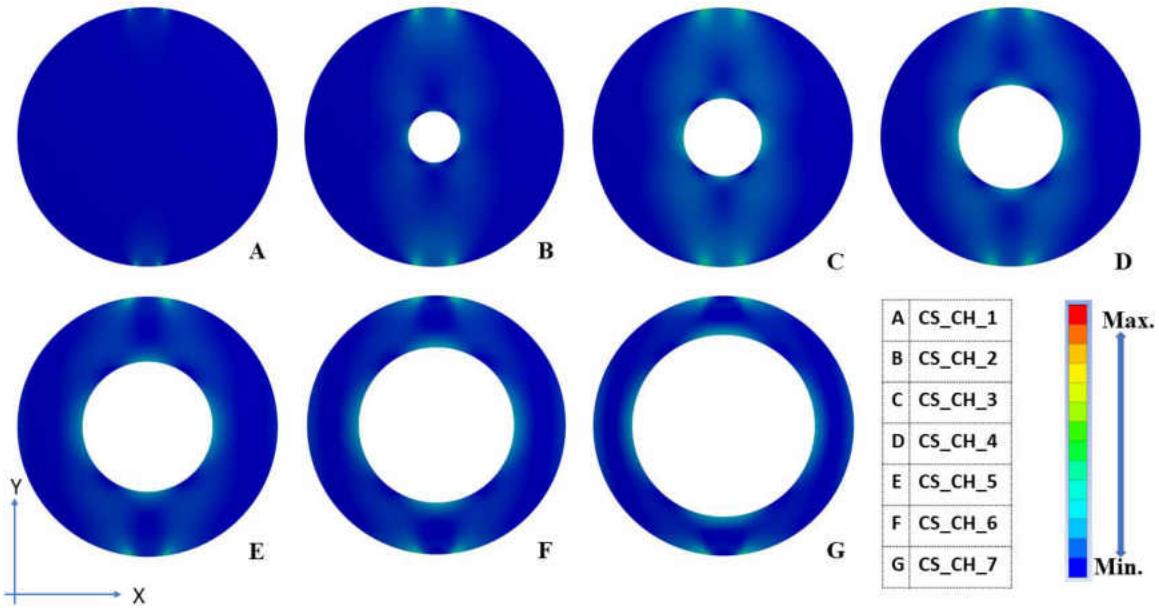

Figure 3.12 Equivalent Stress Variation on Circular Specimen with Circular Holes.

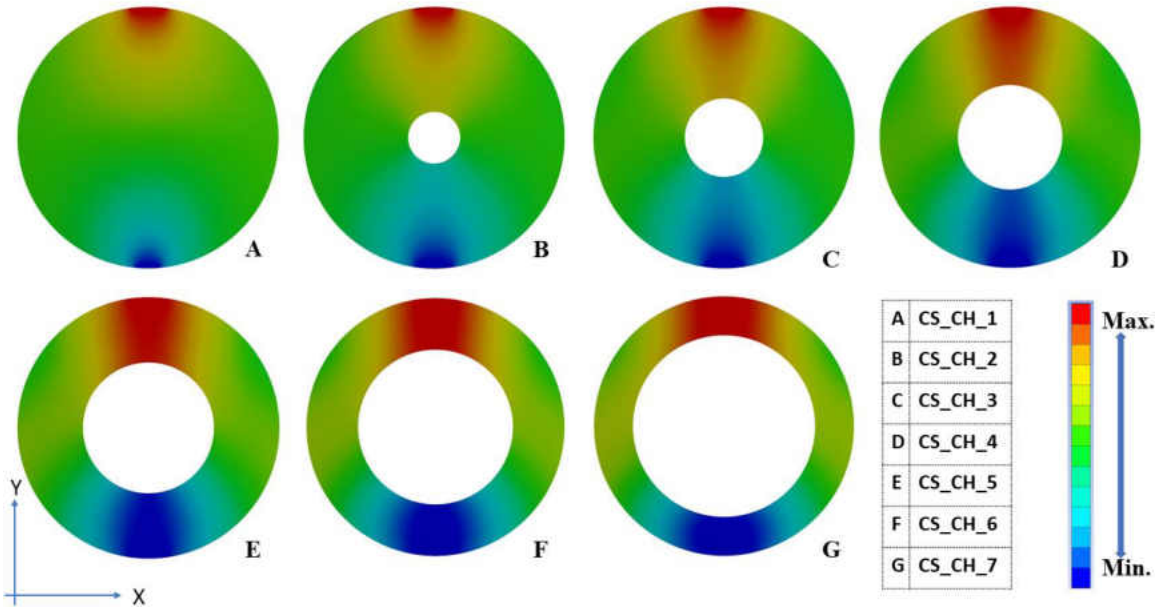

Figure 3.13 Deformation Variation on Circular Specimens with Circular Holes.

ii. ***Circular Specimen with Square Holes.*** Figure (3.14) to Figure (3.17) show normal stress and deformation variation for circular specimens with square holes along X and Y axes. The results can be summarized as,

- Maximum Normal stress is observed for solid specimen (0% hollowness). The stress is compressive for solid specimen along the Y-axis until the inside edge. For all other hollow specimens, the stress is initially compressive and then rises to zero at the inside edge. For the specimen with 38.48% hollowness, the stress is initially compressive at the outside edge, but goes tensile, rises to peak and drops down to zero at the inside edge.

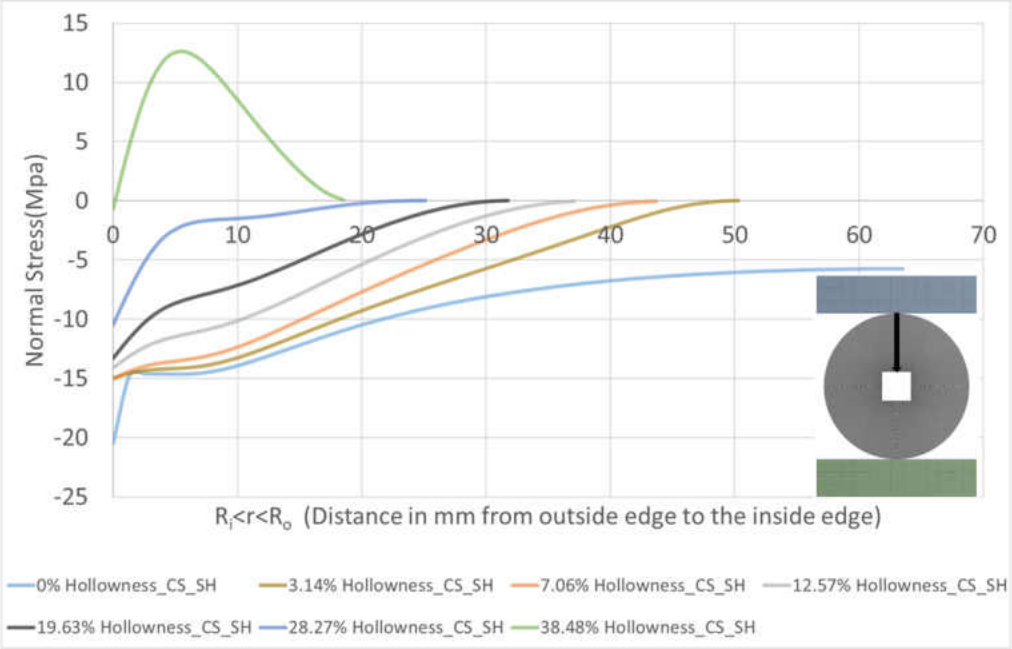

Figure 3.14 Normal Stress along Y-axis.

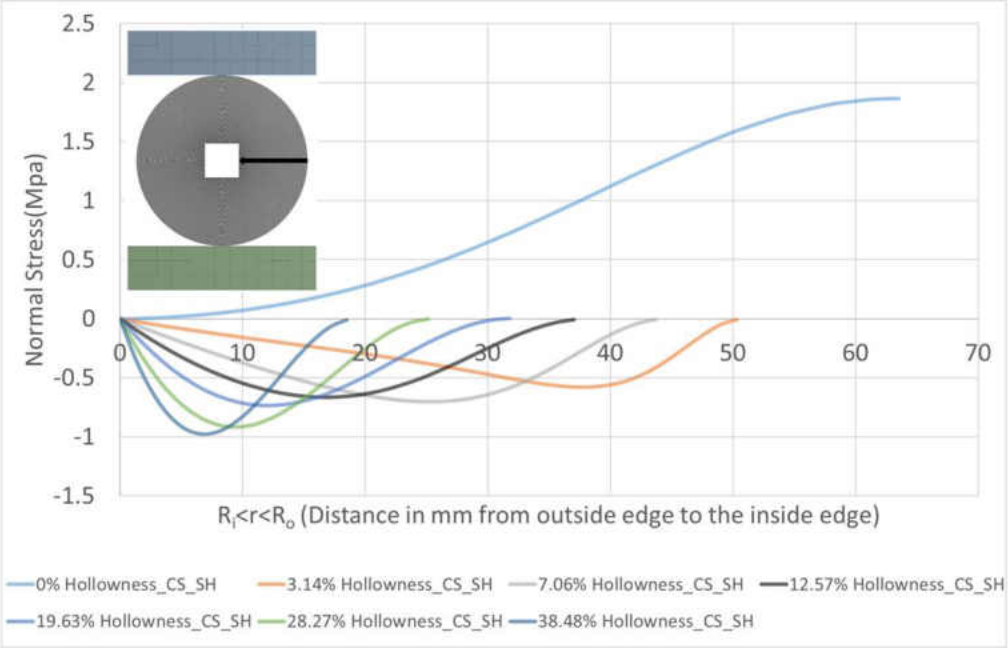

Figure 3.15 Normal Stress Variation along X-axis.

- Normal stress along X-axis is maximum for solid specimen. The stress is tensile for the solid specimen all along the X-axis. For rest of the specimens, the stress along X-axis is compressive, drops down to maximum and then rises to zero at the inside edge.

- Deformation along X and Y-axes are maximum for 38.49% hollow specimens. The deformation variation is almost constant along both of the axes until the inside edge.

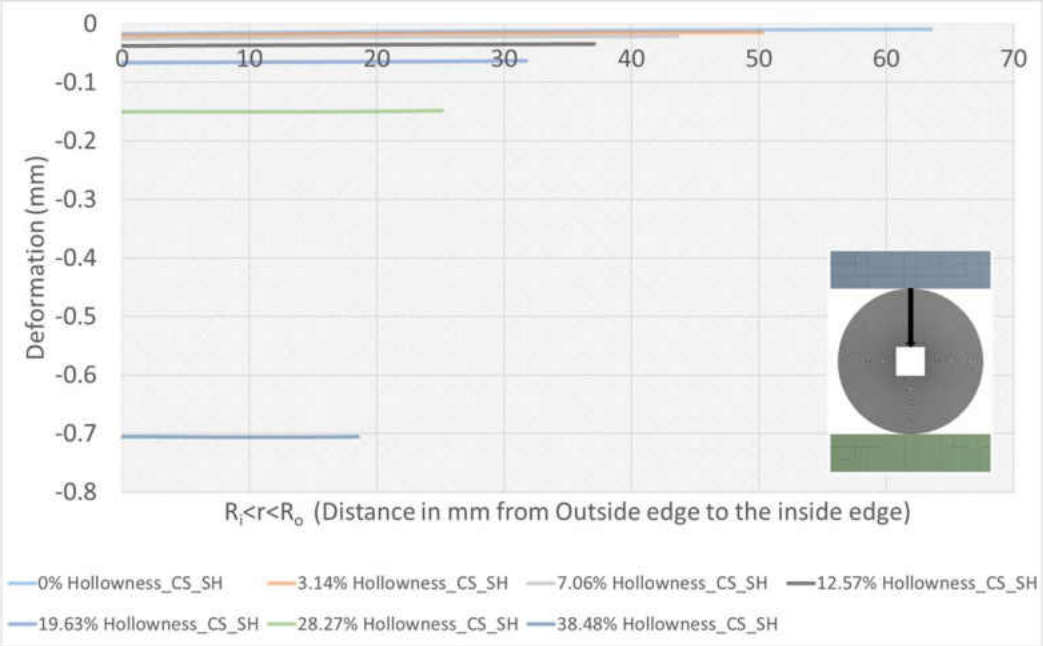

Figure 3.16 Directional Deformation Variation along Y-axis.

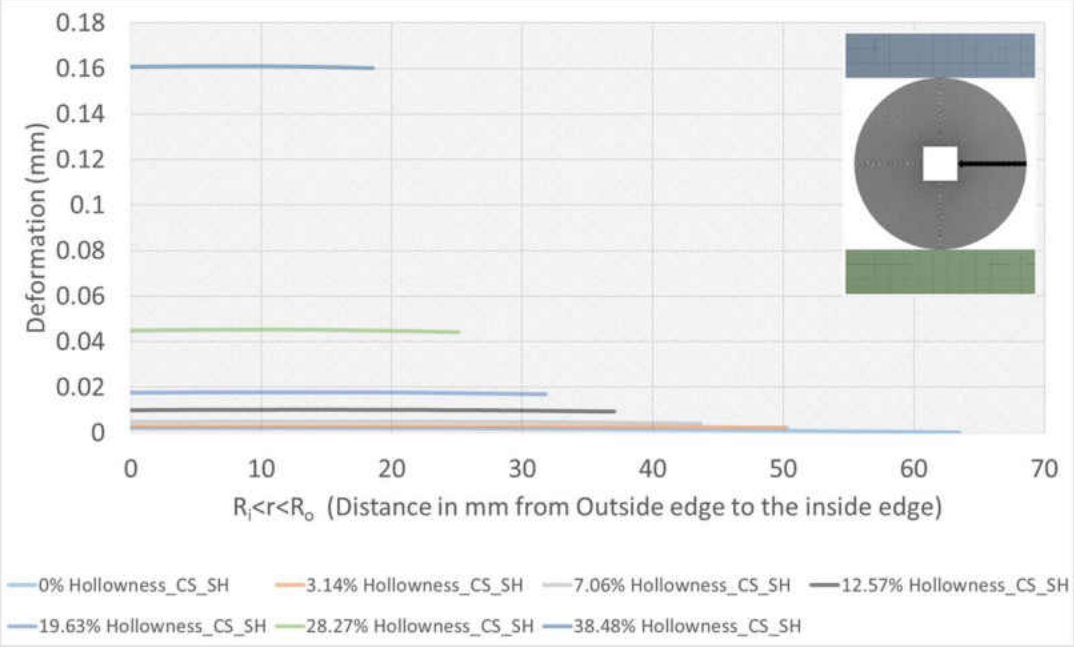

Figure 3.17 Directional Deformation Variation along X-axis.

Figure (3.18) shows the variation of Equivalent (von Mises) stress on the specimens due to change in hollowness during normal compressive loading. Stress concentration is observed at the inside corner edges of the square voids and at points of contact of the plates and specimens. Stress does not vary significantly along the X-axis with the change in hollowness. Displacement variation on circular specimens with square holes are shown in Figure (3.19). The upper half deforms considerably along the Y-axis on normal compressive loading, whereas deformation is minimum along the bottom half. Deformation along the X-axis is almost the same for a change in hollowness.

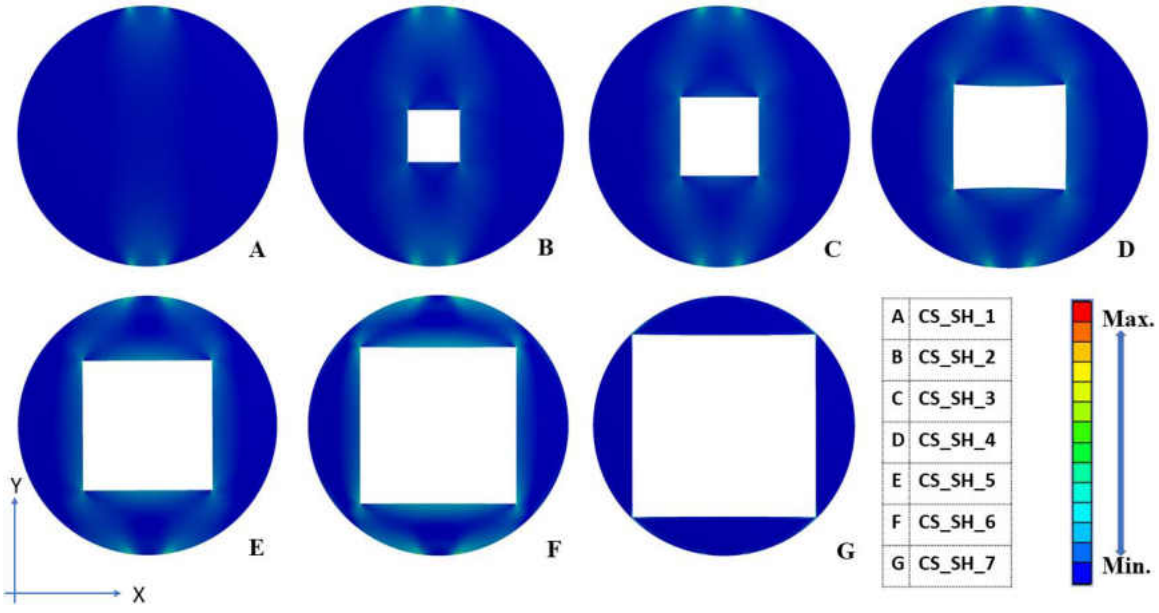

Figure 3.18 Equivalent Stress Variation on Circular Specimens with Square Holes.

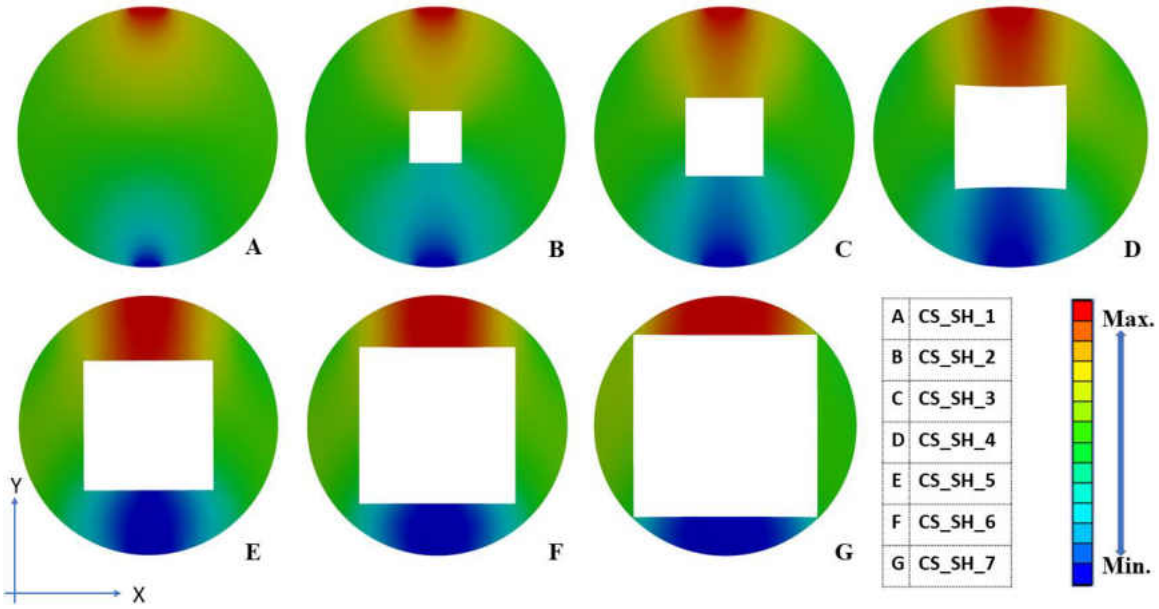

Figure 3.19 Deformation Variation on Circular Specimens with Square Holes.

iii. ***Square Specimen with Circular Holes.*** Figure (3.20) to Figure (3.23) show Normal stress and deformation variation along the Y and X axis for Square specimens with Circular Holes with the change in hollowness size in them. The results can be summarized as,

- Maximum normal stress along Y-axis is observed on the solid specimens (0% hollowness). For all other specimens, it is initially compressive and then decreases to zero at the inside edge.
- Normal stress along X-axis is minimum for the solid specimens. It is compressive along the X-axis. For all other specimens, the stress goes

compressive, reaches its peak at almost center distance between outside and inside edge, and then drops down to minimum at the inside edge.

Deformation along X and Y-axes are minimum for the solid specimens. Maximum deformation is observed for 38.48% hollow specimens along both X and Y-axes. The deformation is almost constant along both the axes.

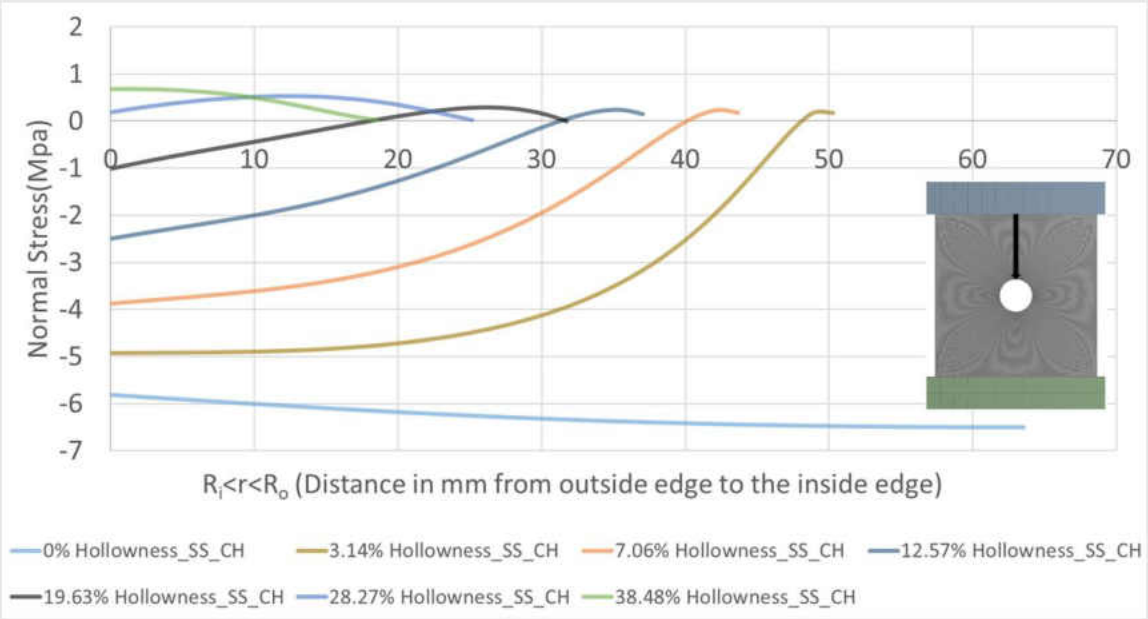

Figure 3.20 Normal Stress Variation along Y-axis.

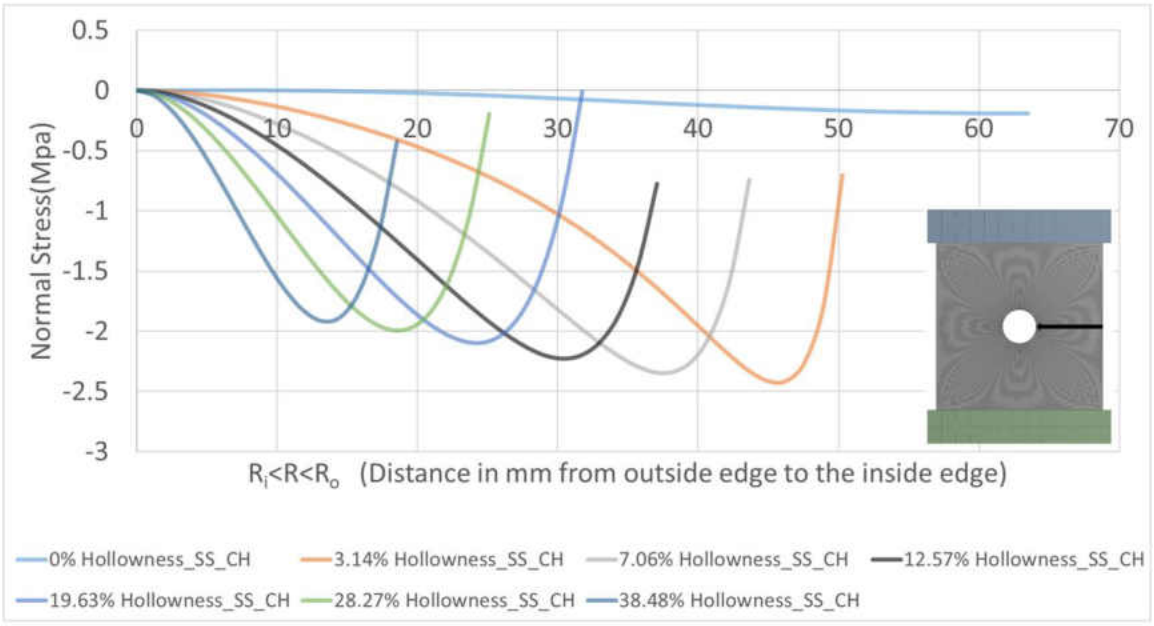

Figure 3.21 Normal Stress Variation along X-axis.

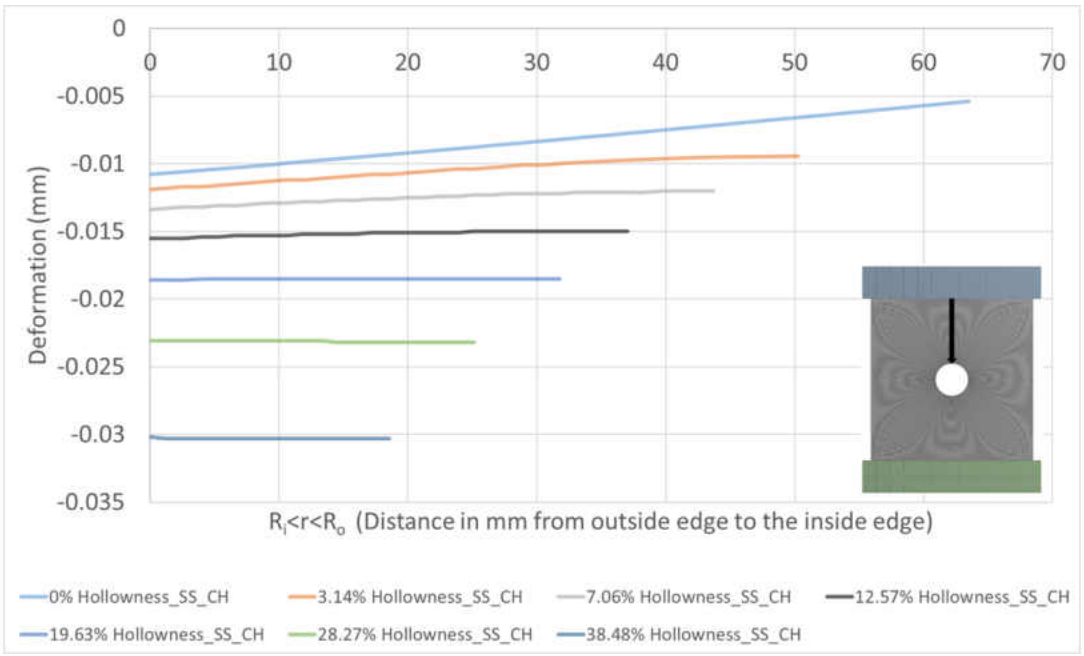

Figure 3.22 Directional Deformation Variation along Y-axis.

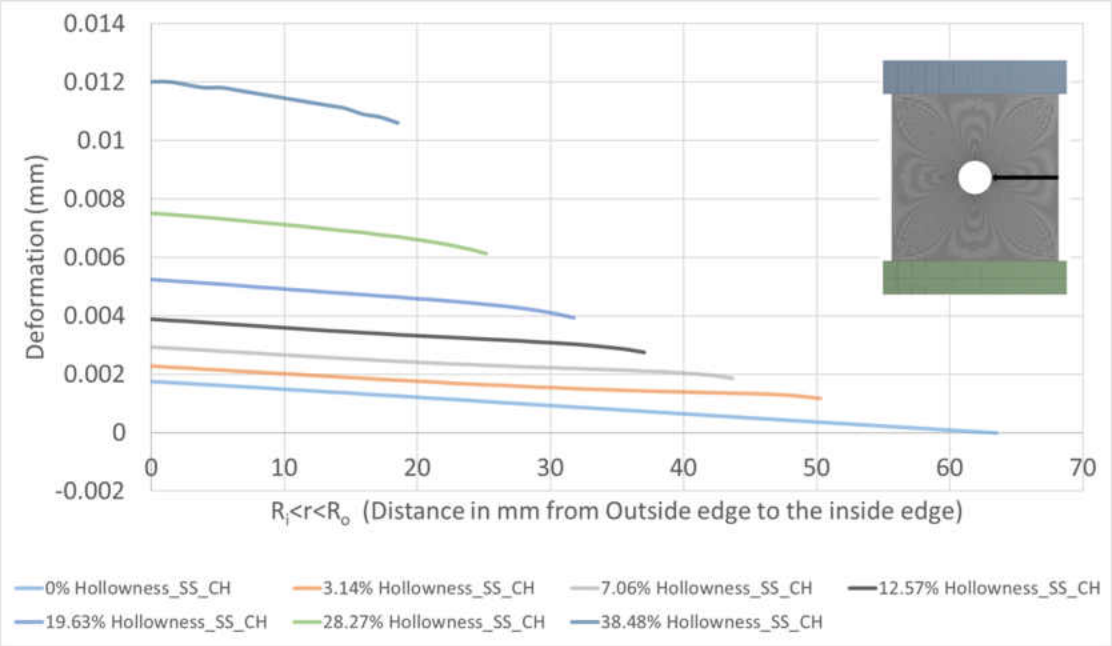

Figure 3.23 Directional Deformation Variation along X-axis.

Equivalent stress (von-Mises) variation in square specimens with circular holes are shown in Figure (3.24). Stress concentration is observed at the top and bottom corners for solid specimen. As hollowness increases, stress distributes within the specimen and low values of stresses are observed along the loading axis as compared to the X axis. For hollow samples, interestingly, stress is concentrated at the inside edges along both X and Y-axis. Higher prominence of stress is observed at the inside edge along X-axis, which could possibly be due to the introduction of bending stress in the specimens.

As shown in Figure (3.25), higher deformation is observed for all the specimens along the upper half due to higher compression. Deformation is minimum along the bottom half of the specimen. The distribution is

symmetric along the loading axis. Minimum stress variation is observed along the X-axis for a change in hollowness.

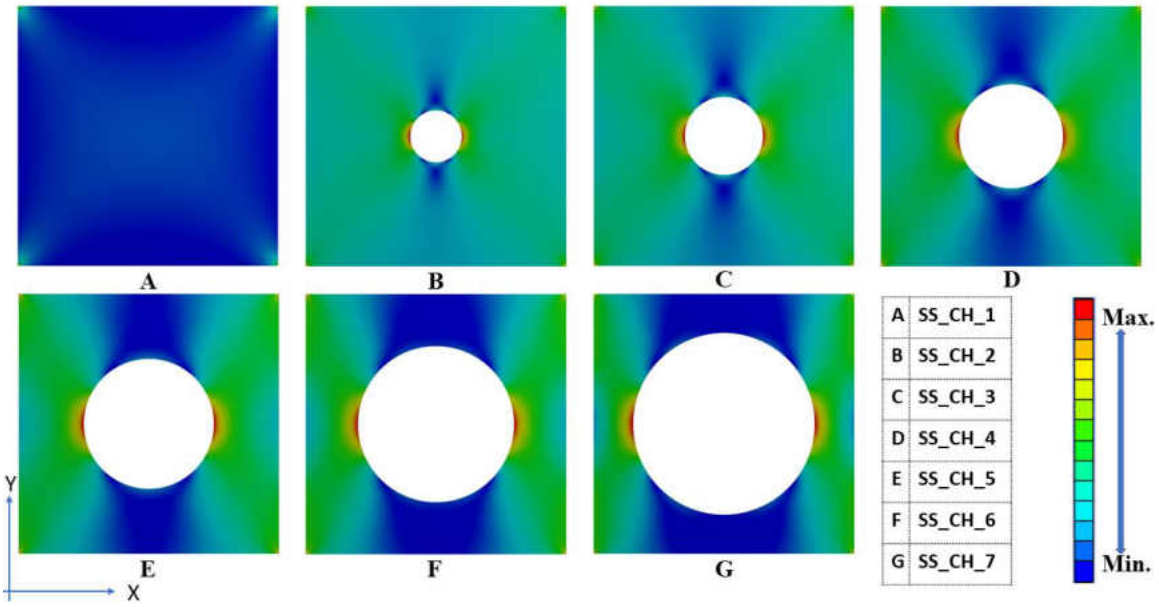

Figure 3.24 Equivalent Stress Variation on Square Specimens with Circular Holes.

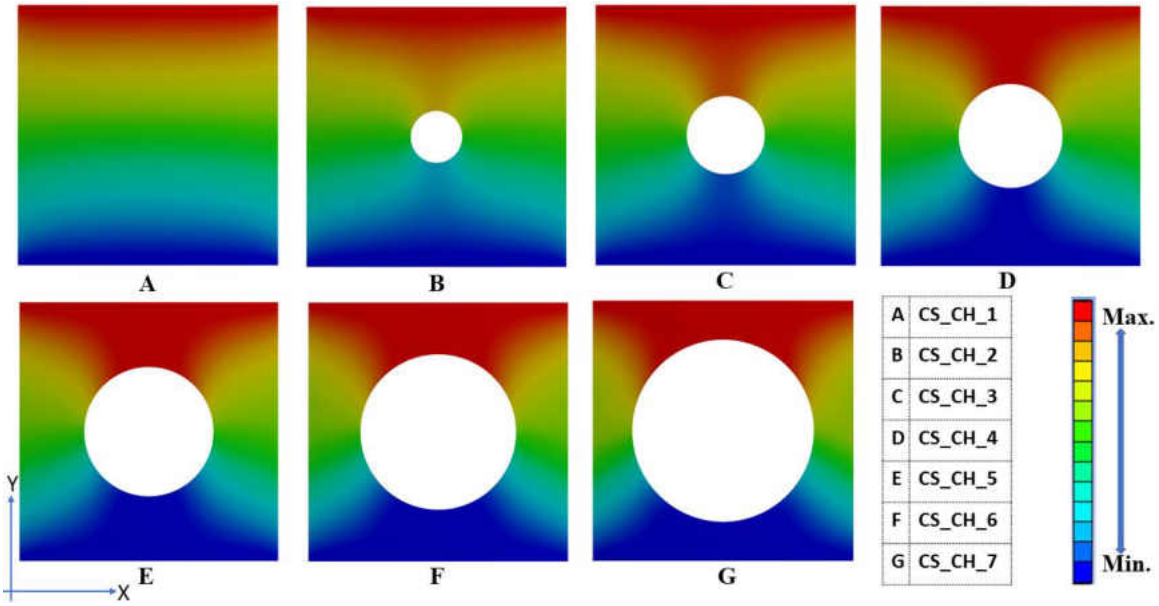

Figure 3.25 Deformation Variation on Square Specimens with Circular Holes.

iv. ***Square Specimens with Square Holes.*** Normal stress and deformation variation for square specimens with square holes are plotted along the outside edge to inside edge as shown in Figure (3.26) to Figure (3.29). The results can be summarized as

- Normal stress along Y-axis is maximum for 0% hollow specimens. The stress is initially compressive and then rises to zero at the inside edge for all other specimens.
- Normal stress along X-axis is minimum for solid specimens. The stress values are all compressive. For each specimen except the solid one, stress increases to a peak at almost center distance between outside and inside edge and then decreases to zero at the inside edge.
- Deformation along X and Y-axes are maximum for 38.49% hollow specimens. Deformation is almost constant along both the axes for each specimen.

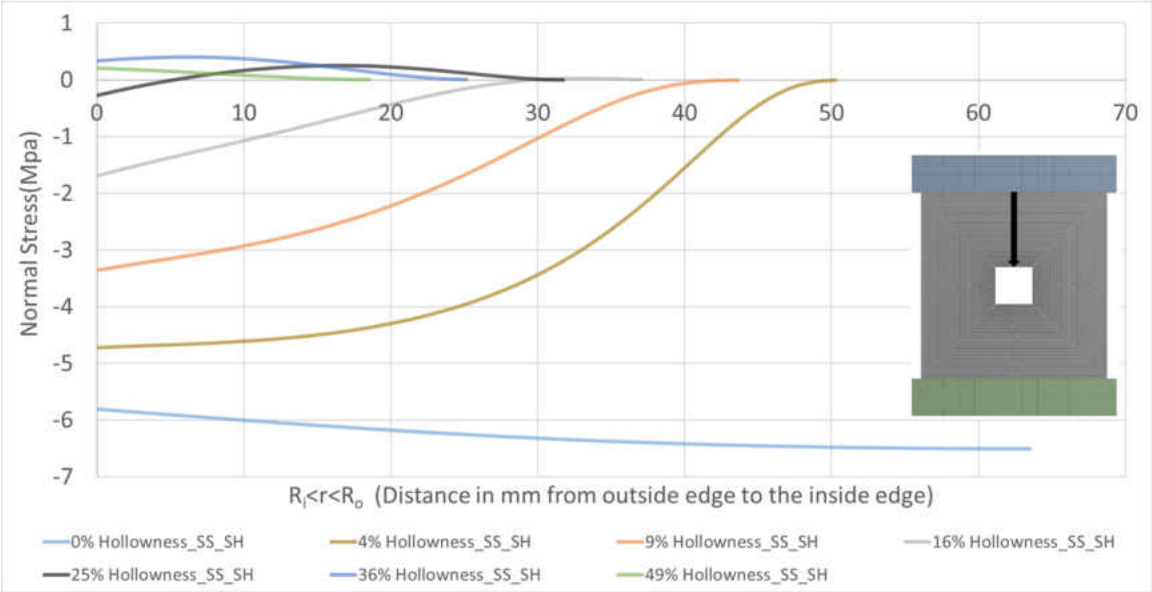

Figure 3.26 Normal Stress Variation along Y-axis.

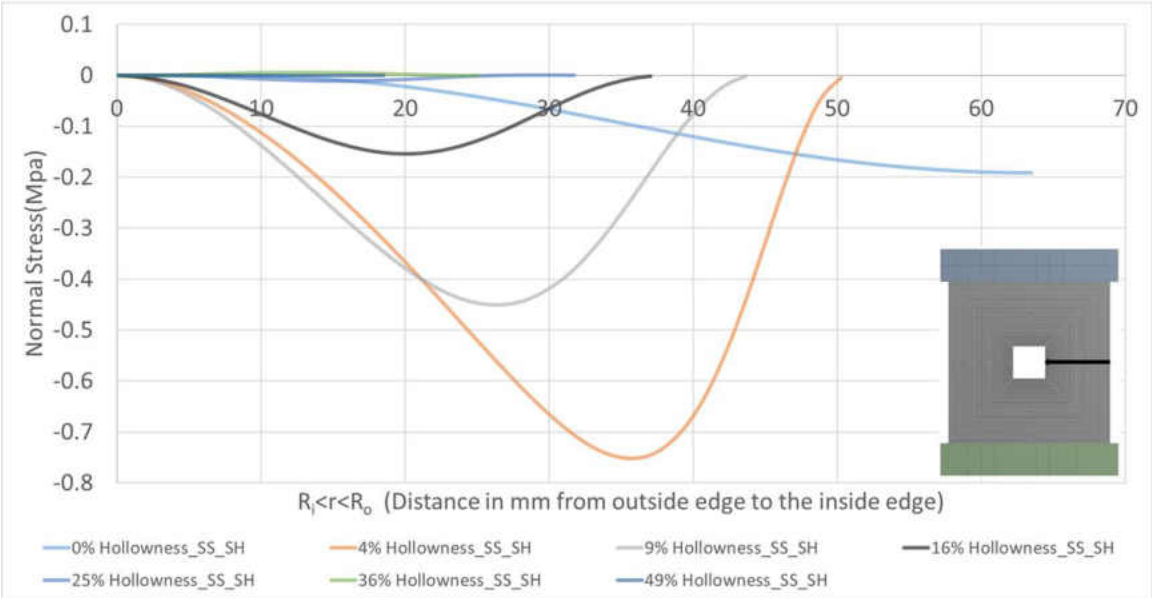

Figure 3.27 Normal Stress Variation along X-axis.

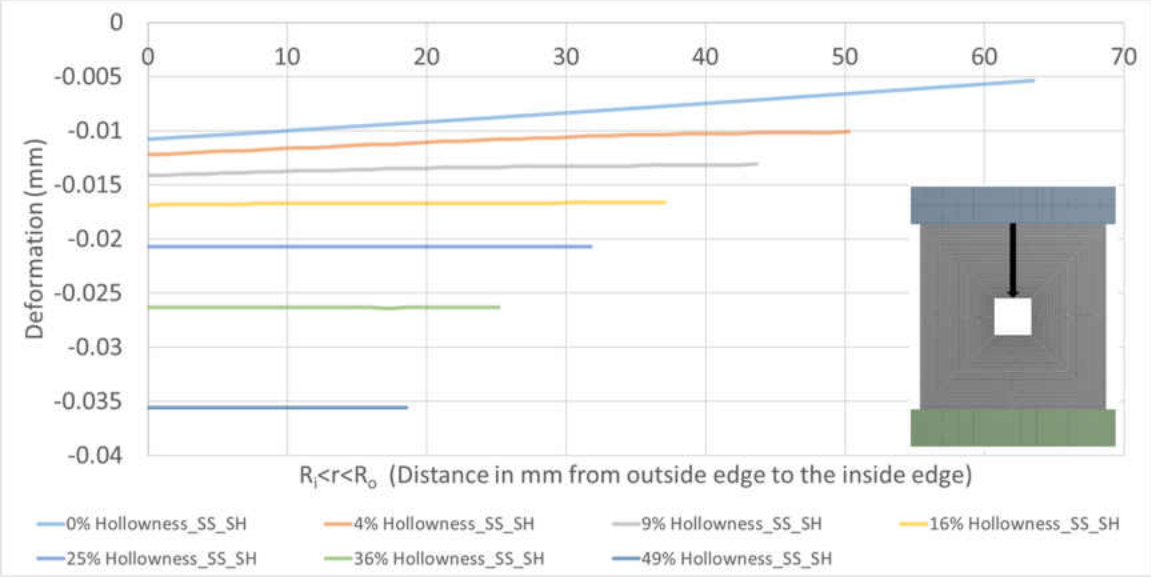

Figure 3.28 Directional Deformation Variation along Y-axis.

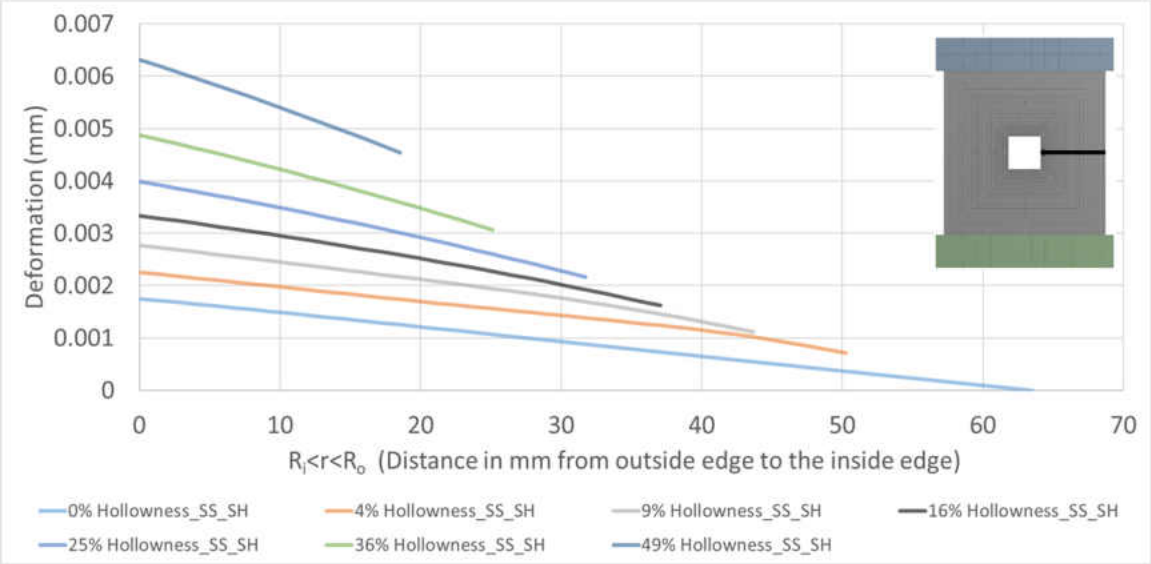

Figure 3.29 Directional Deformation along X-axis.

Equivalent (von-Mises) stress is concentrated at the corners for solid specimens under normal compression as shown in Figure (3.30). The stresses

then distribute throughout the body but still would be symmetrical along X and Y-axis. Higher stress concentration is observed at the inside corners of the voids. Deformation variation in Square specimens with square holes is shown in Figure (3.31). Deformation is minimum along the bottom half of the specimen and maximum along the upper half. The distribution is symmetric along Y-axis and the variation is minimum along X-axis for change in hollowness of the specimen.

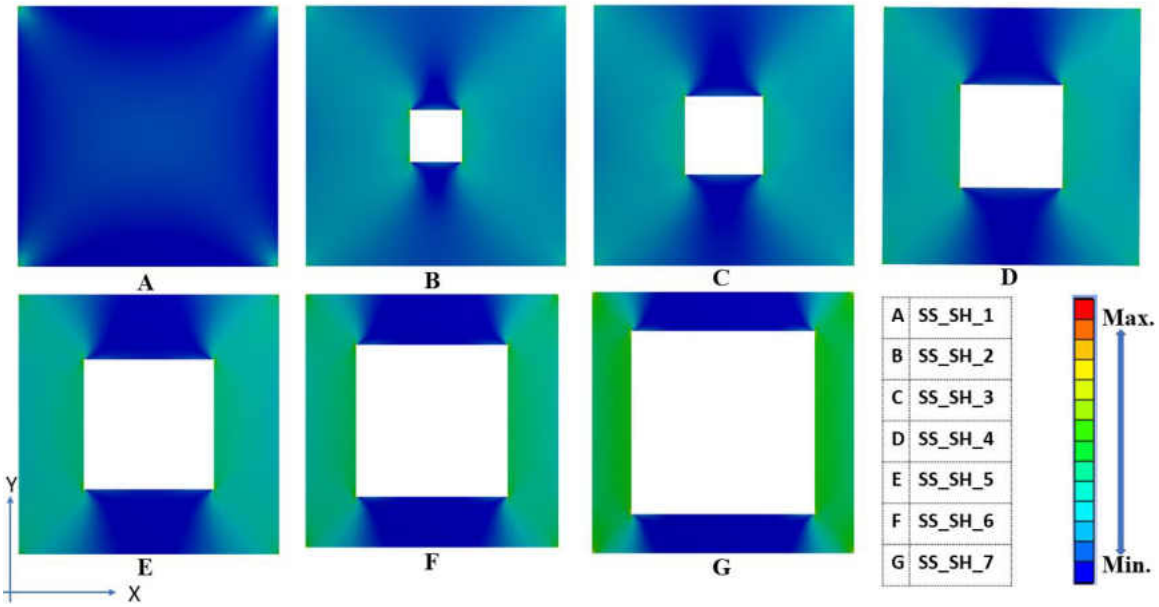

Figure 3.30 Equivalent Stress Variation on Square Specimens with Square Holes.

From the above results, it can be inferred that stress distribution is better for Concentric Regular specimens. For concentric irregular specimens, stress gets concentrated at the inside edges and corners of inside edges. Stress on specimens with concentrated loading is concentrated along the loading axis. Stress along X-axis does not vary with hollowness for concentrated loading. For specimens under distributed loadings, stress varies with

hollowness along both the axes. Maximum stress variation is observed along the X-axis with increase in hollowness.

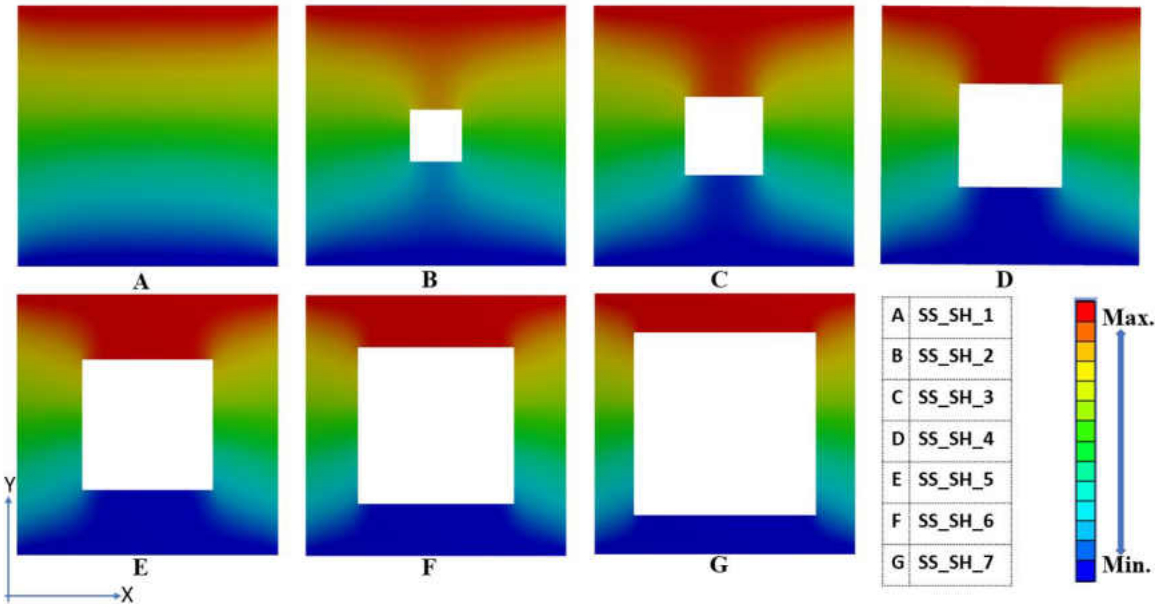

Figure 3.31 Deformation Variation on Square Specimens with Square Holes.

For all types of specimens, minimum deformation is observed for the bottom half of the specimens. Deformation is symmetric and concentrated along the loading axis for all the specimens with concentrated loadings for change in hollowness. For concentric irregular specimens, deformations are maximum along the inside edges. Maximum deformation is observed at the corner edges due to stress concentration.

3.3 Optimum Hollowness from FE results

The percentage hollowness at which the strain values are minimum is noted as the optimum hollowness for the loading case. Strain values obtained from the FEA are plotted against hollowness for different load values to obtain optimum hollowness. The strain values

measured at ΔX=13mm, ΔX=19mm, ΔY=13mm and ΔY=19mm are presented below. The distances are taken from the outer edge along two perpendicular axes, X and Y, where Y is the loading axis.

3.3.1 Strain Variation for Circular Specimen with Circular Holes

Figure (3.32) shows the location of measurement of normal strain along the loading axis (Y-axis) and the axis perpendicular to that (X-axis). Figure (3.33) to Figure (3.36) show the variation of strain for the change in load on Circular specimens with circular holes (CS_CH) measured at different point along X and Y-axes.

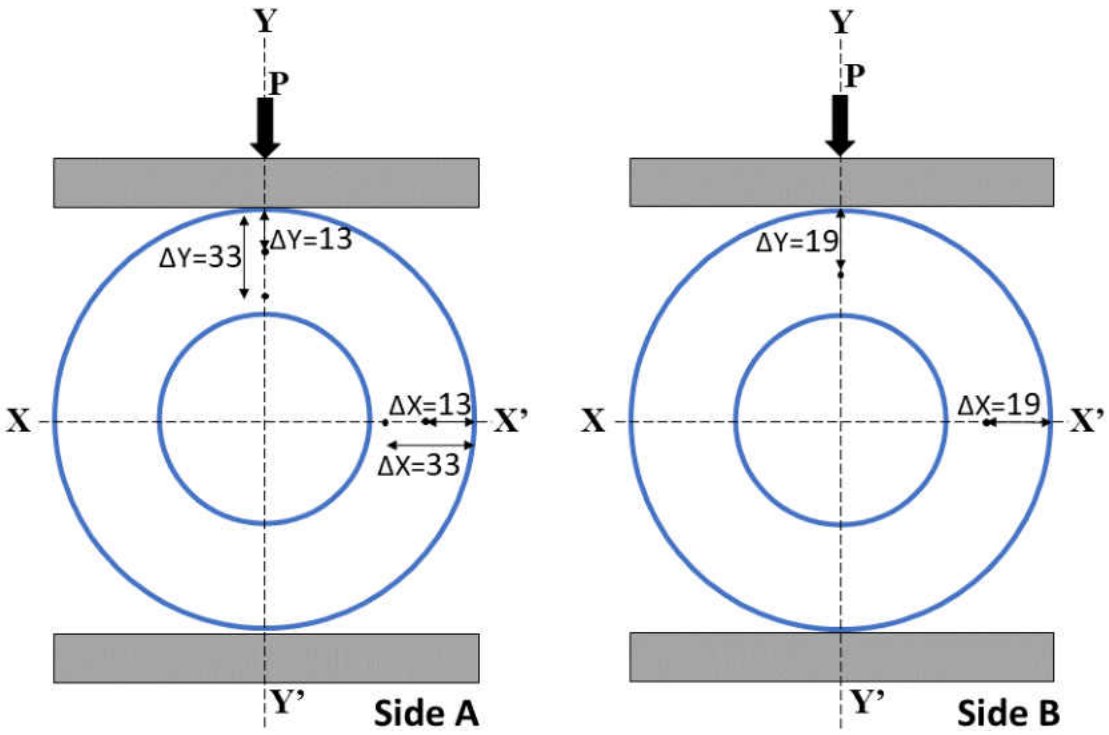

Figure 3.32 Strain Measurement Points on Circular Specimens with Circular Holes.

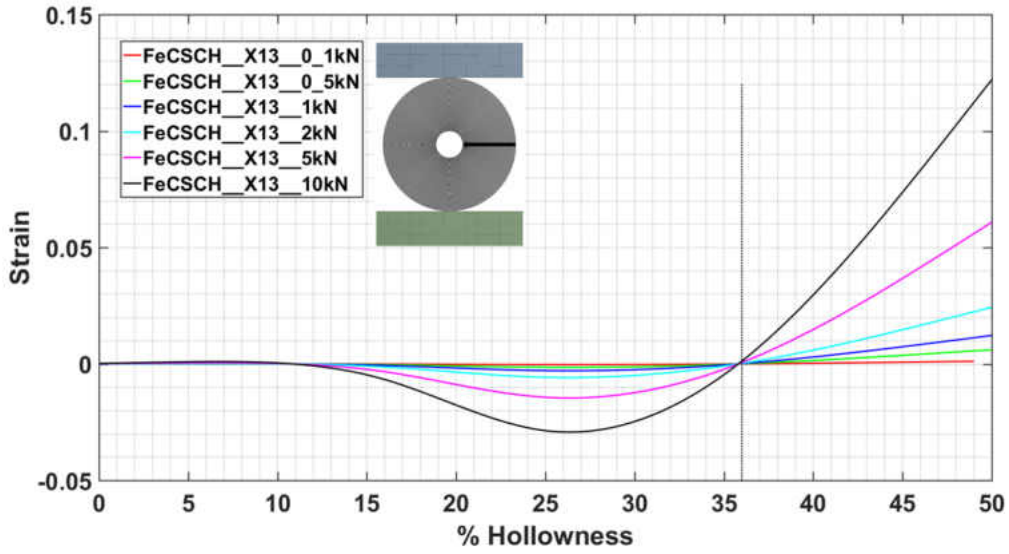

Figure 3.33 Strain Variation at ΔX=13mm on Circular Specimens with Circular Holes.

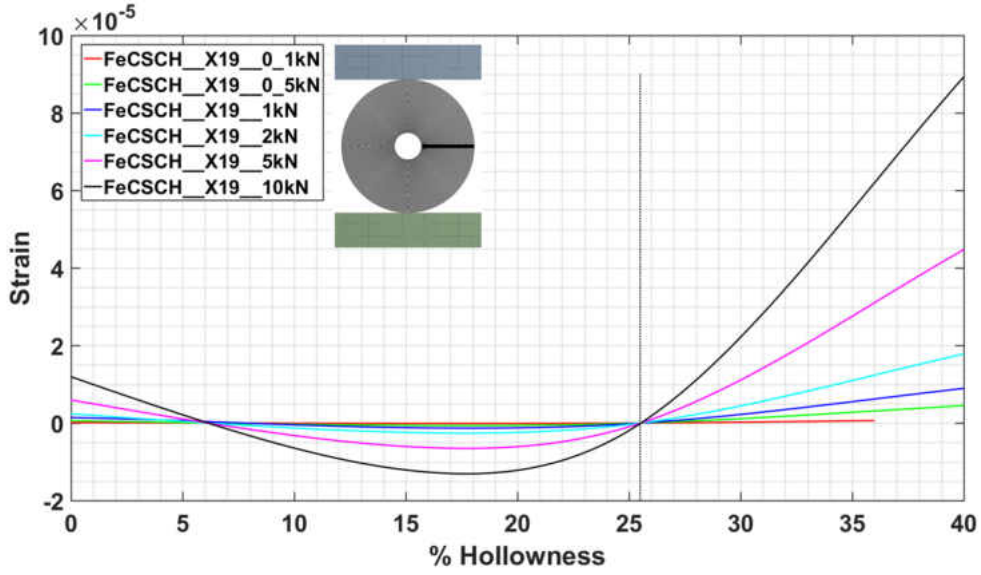

Figure 3.34 Strain Variation at ΔX=19mm on Circular Specimens with Circular Holes.

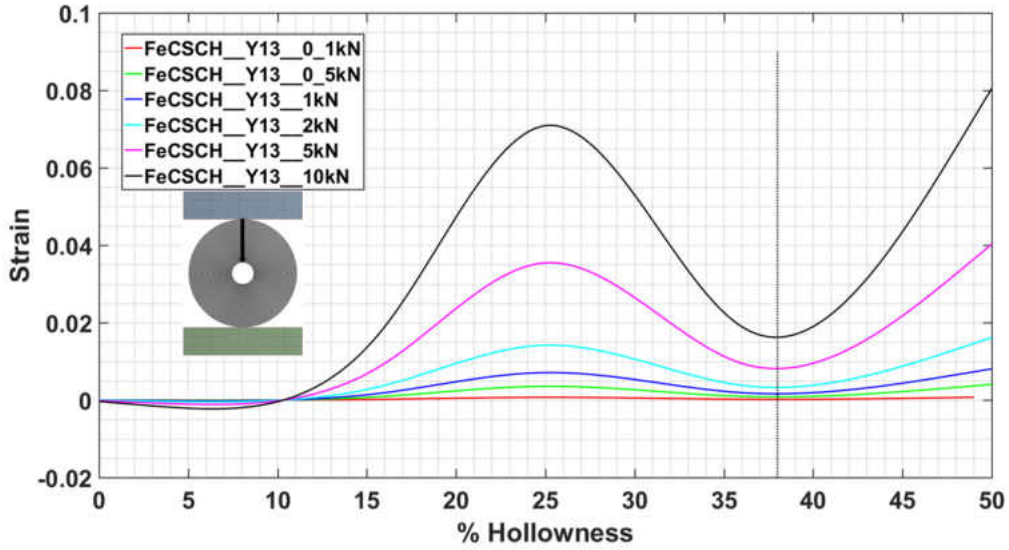

Figure 3.35 Strain Variation at ΔY=13mm on Circular Specimens with Circular Holes.

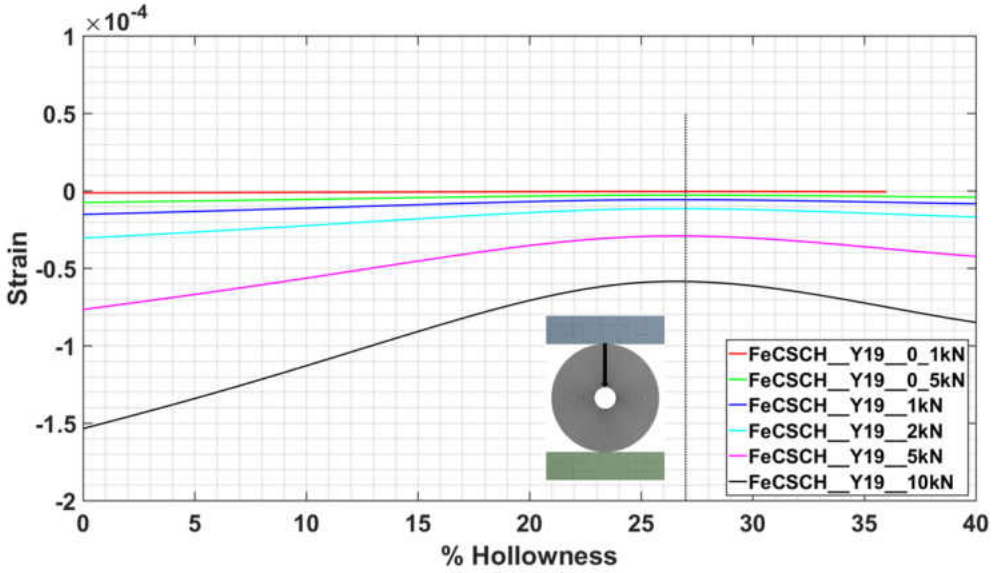

Figure 3.36 Strain Variation at ΔY=19mm on Circular Specimens with Circular Holes.

Figure (3.37) shows the variation of normal strain variation at different locations within the specimen for increase in hollowness percentage. Finite element results show that normal strain rises steeply after about 40% hollowness. Optimum hollowness for this loading and specimen case varies between 25% to 40%. Strain rises significantly beyond the optimum hollowness values, indicating higher chances of failure in the specimens.

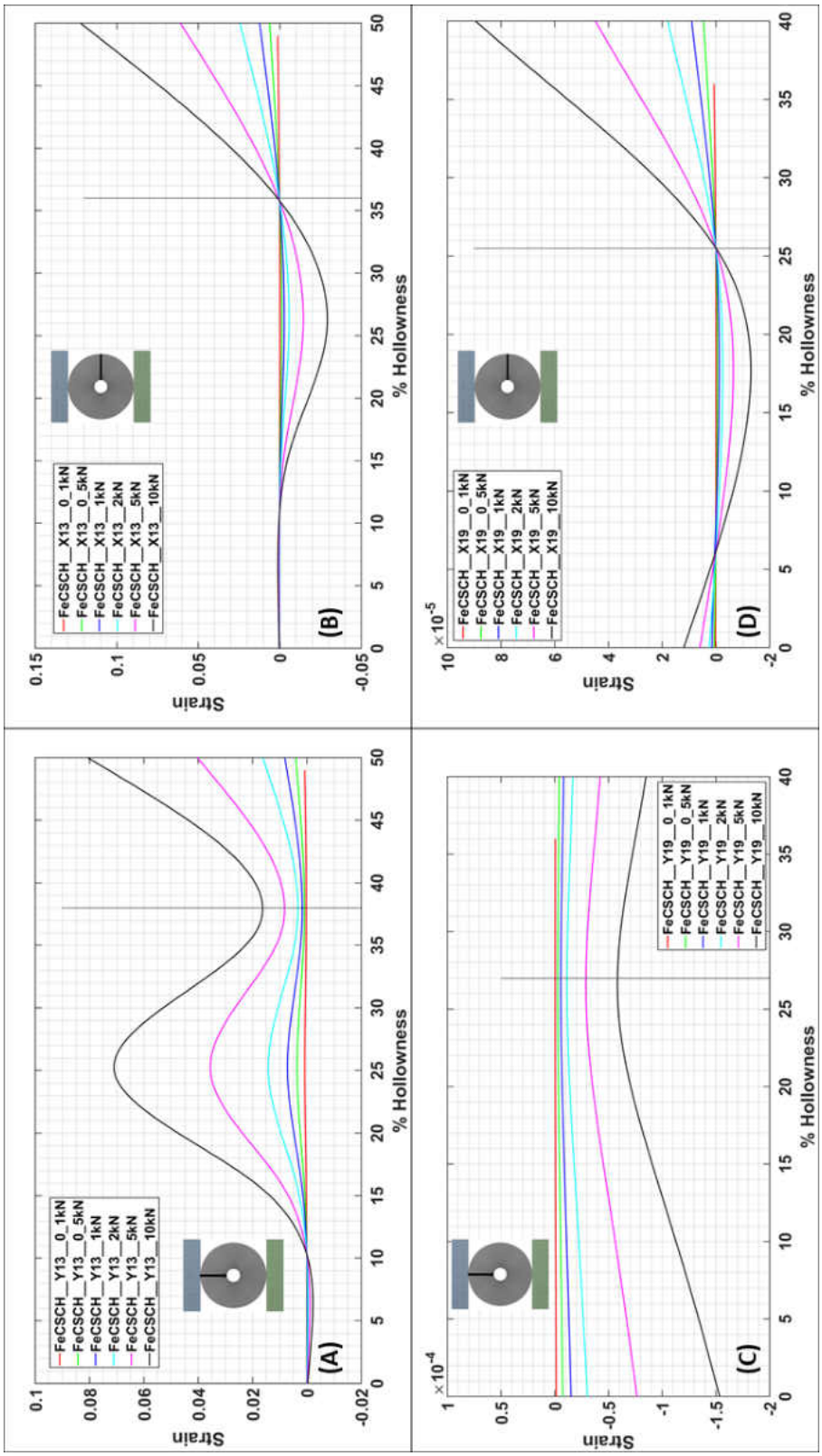

Figure 3.37 Strain Variation on Circular Specimen with Circular Holes. (A) ΔY=13mm (B) ΔX=13mm (C) ΔY=19mm (D) ΔX=19mm

3.3.2 Strain Variation on Square Specimen with Circular Holes

Figure (3.38) show Square specimen with circular holes and the location of measurement of normal strain in them. Figure (3.39) to Figure. (3.42) show the variation of strain for the change in load on Square specimens with Circular Holes (SS_CH) measured at these points.

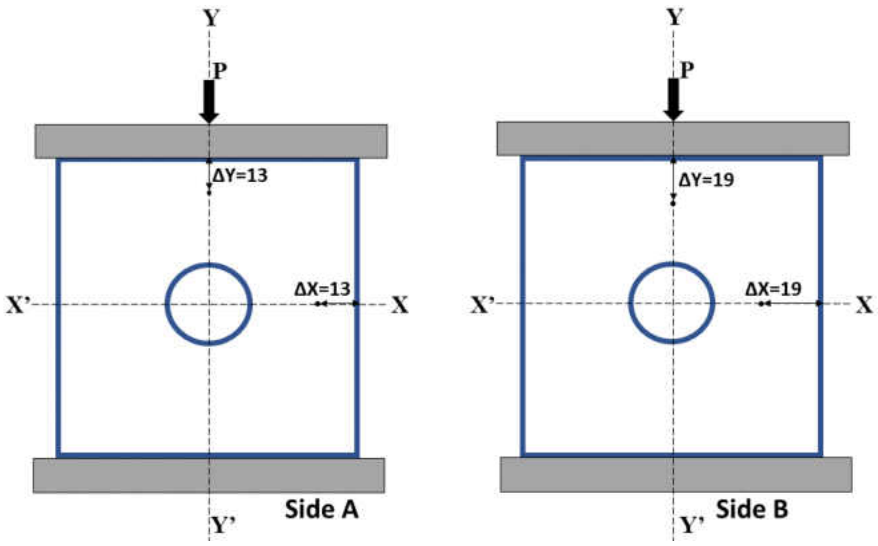

Figure 3.38 Strain Measurement Points on Square Specimens with Circular Holes.

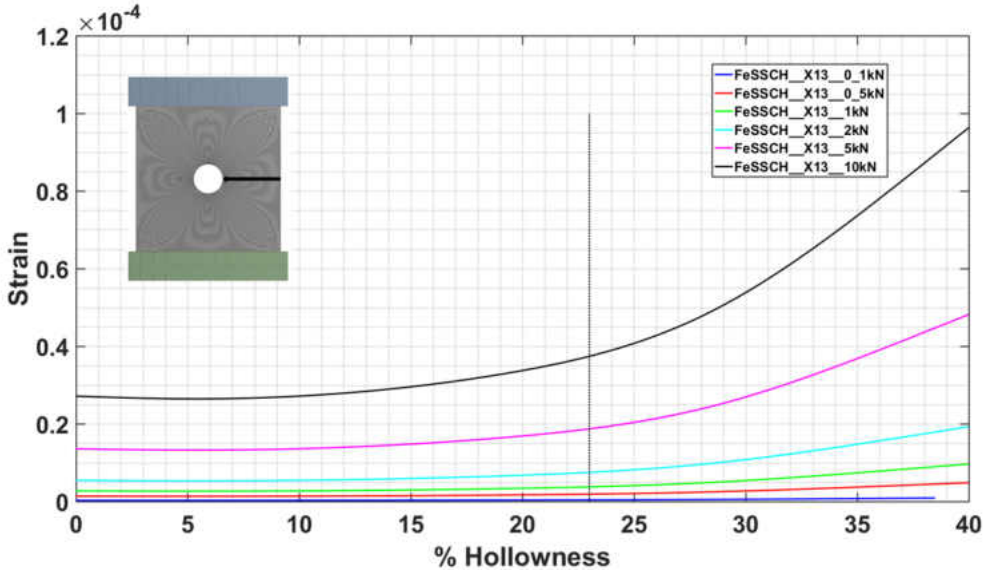

Figure 3.39 Strain Variation at ΔX=13mm on Square Specimens with Circular Holes.

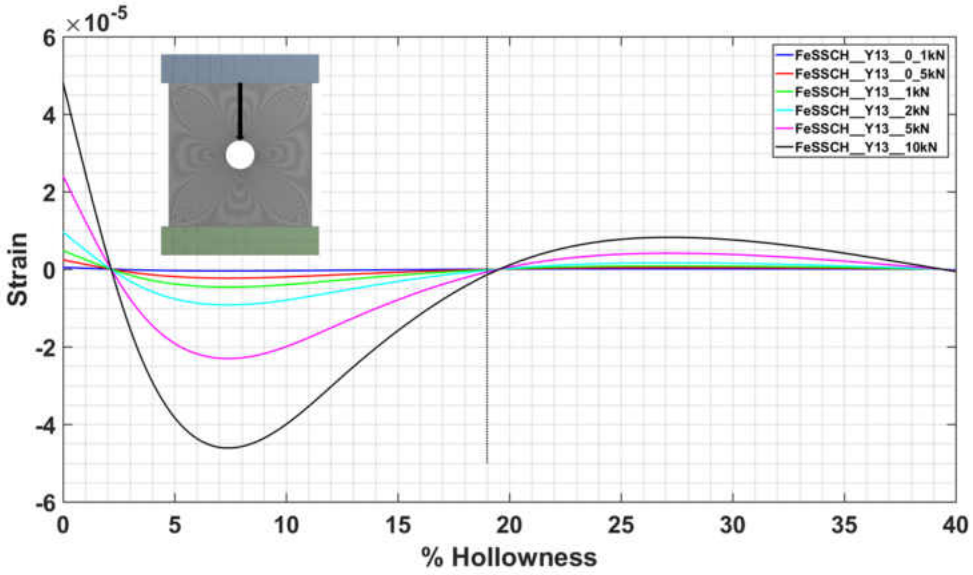

Figure 3.40 Strain Variation at ΔY=13mm on Square Specimens with Circular Holes.

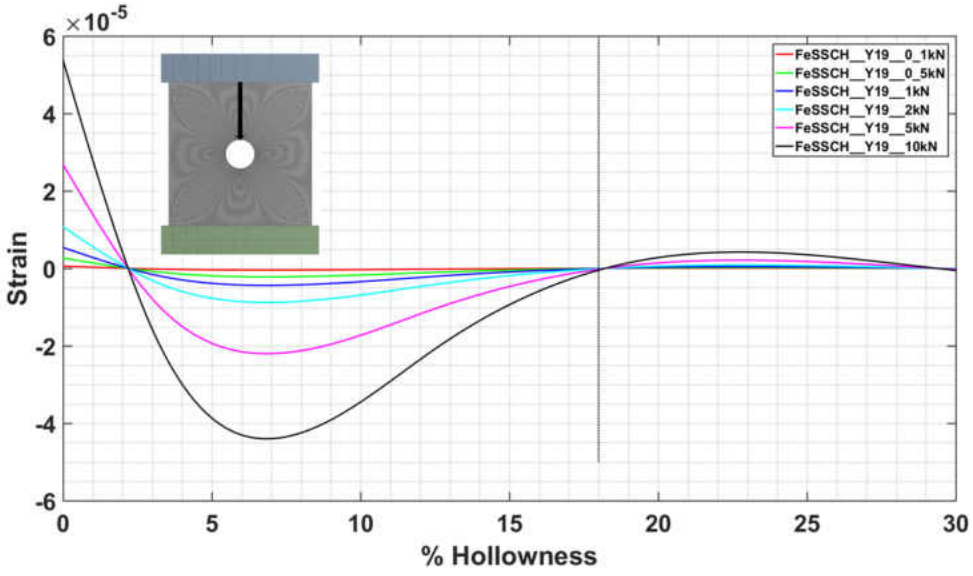

Figure 3.41 Strain Variation at ΔY=19mm on Square Specimens with Circular Holes.

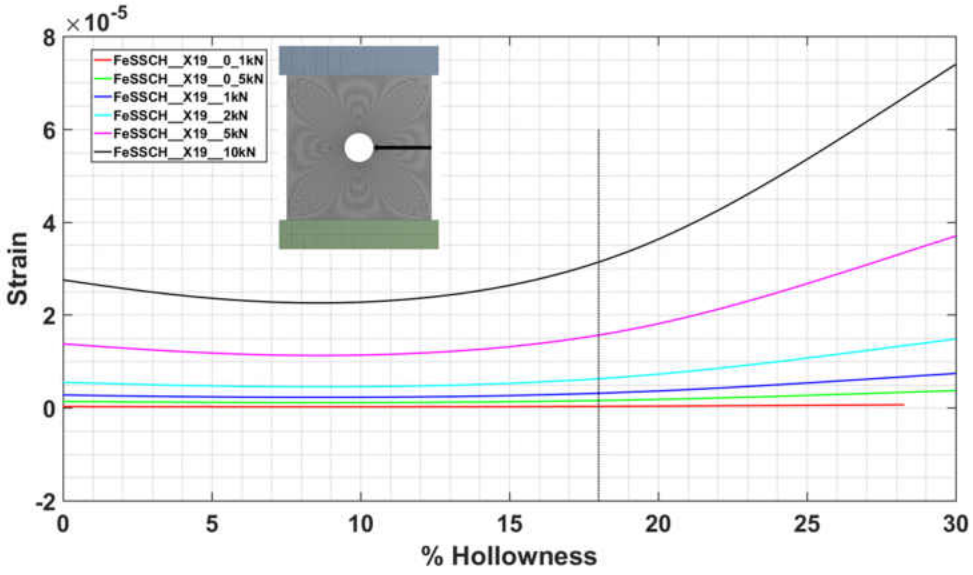

Figure 3.42 Strain Variation at ΔX=19mm on Square Specimens with Circular Holes.

Figure (3.43) shows the variation of normal strain variation at different locations within the specimen for increase in hollowness percentage. Finite element results show that optimum hollowness for this loading case is around 20% as strain rises significantly beyond 20% hollowness along Y and X-axis.

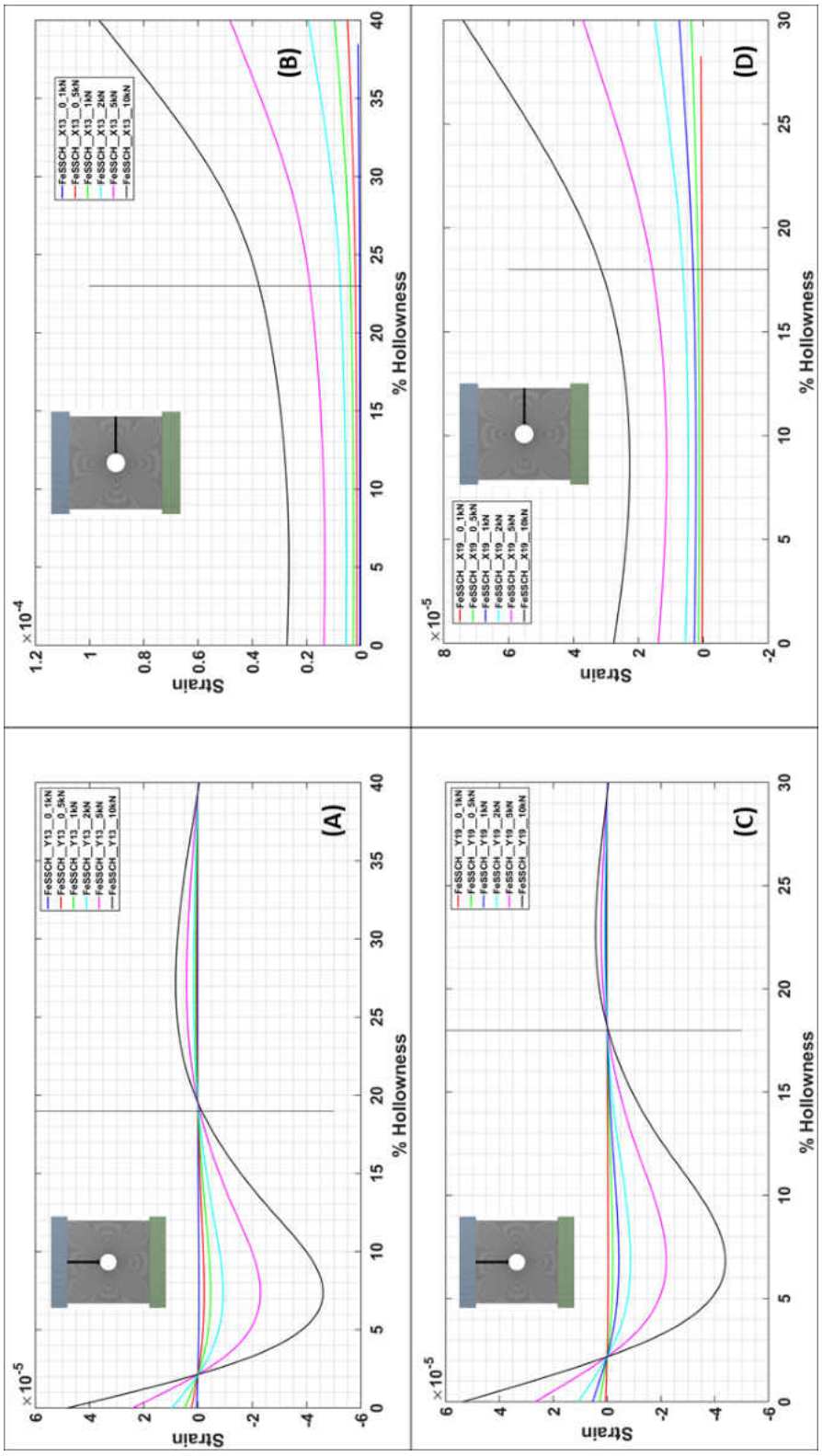

Figure 3.43 Strain Variation on Square Specimens with Circular Holes. (A) ΔY=13mm (B) ΔX=13mm (C) ΔY=19mm (D) ΔX=19mm

3.3.3 Strain Variation along Y-axis for Different Types of Specimens

Figure (3.44) shows location along Y-axis for measurement of strain on different FE models. Figure (3.45) shows variation of strains along Y-axis for different type of specimens. The plots on left are for strain variation along Y-axis for circular specimens with concentric circular holes under normal compressive loading. The strain is optimum for around 25% to 40% hollowness. The plots on right are for strain variation along Y-axis for square specimens with concentric circular holes under normal compressive loading. The strain values are rise steeply beyond 20% hollowness, indicating an increased possibility of failure beyond 20% hollowness of specimens.

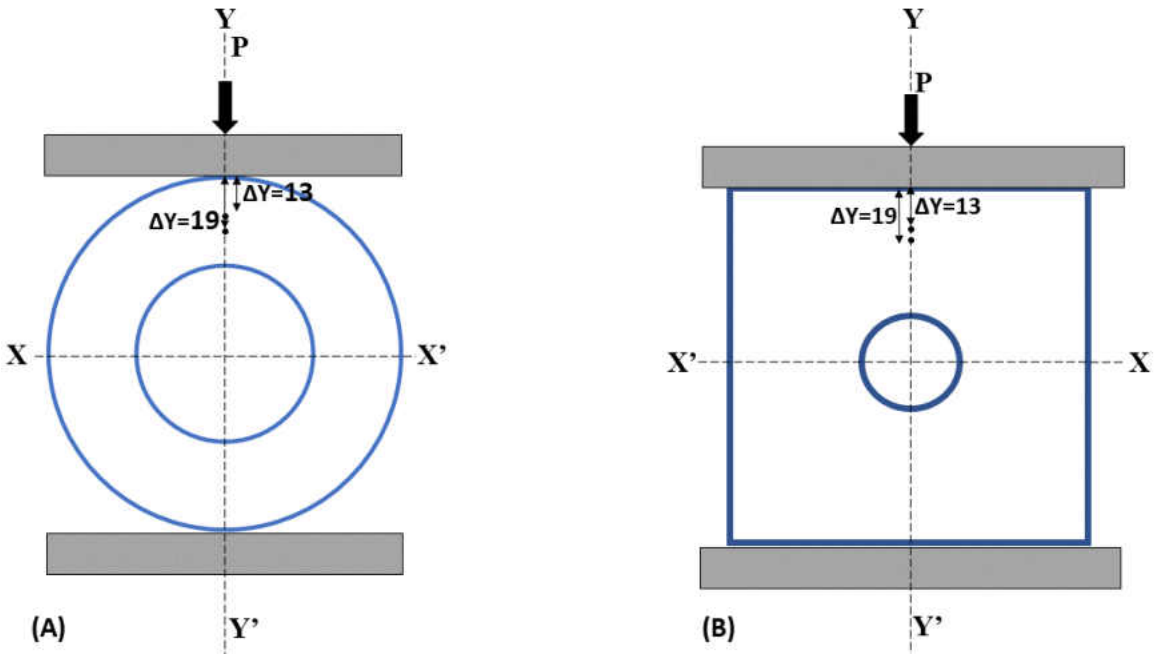

Figure 3.44 Strain Measurement Points on Different Specimens along Y-axis.

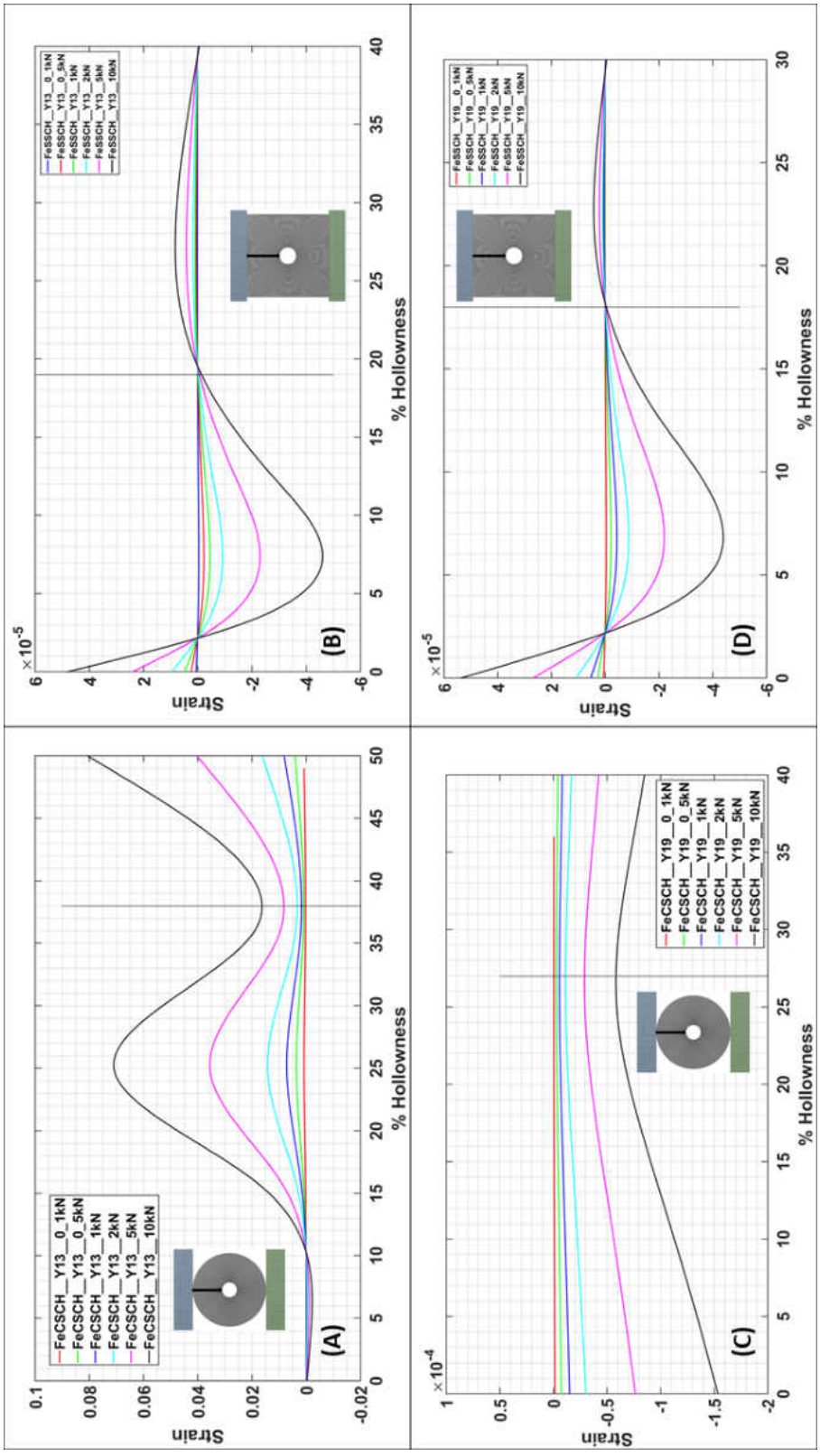

Figure 3.45 Variation along Y-axis. (A) CS_CH_Δ=Y13 (B) SS_CH_ΔY=13 (C) CS_CH_ΔY=19 (D) SS_CH_ΔY=19

3.3.4 Strain Variation along X-axis for Different Types of Specimens

Figure (3.46) shows the location of strain measurement on FE models for different types of specimens along X-axis. Figure (3.47) shows the comparative variation of strain with hollowness for two different types of specimens along X-axis. The plots on left are for strain variation along X-axis for circular specimens with concentric circular holes under normal compressive loading. Optimum strain is observed for around 25% to 35% hollowness. The plots on right are for strain variation along X-axis for square specimens with concentric circular holes under normal compressive loading. The optimum strain values are observed between 15% to 25% hollowness.

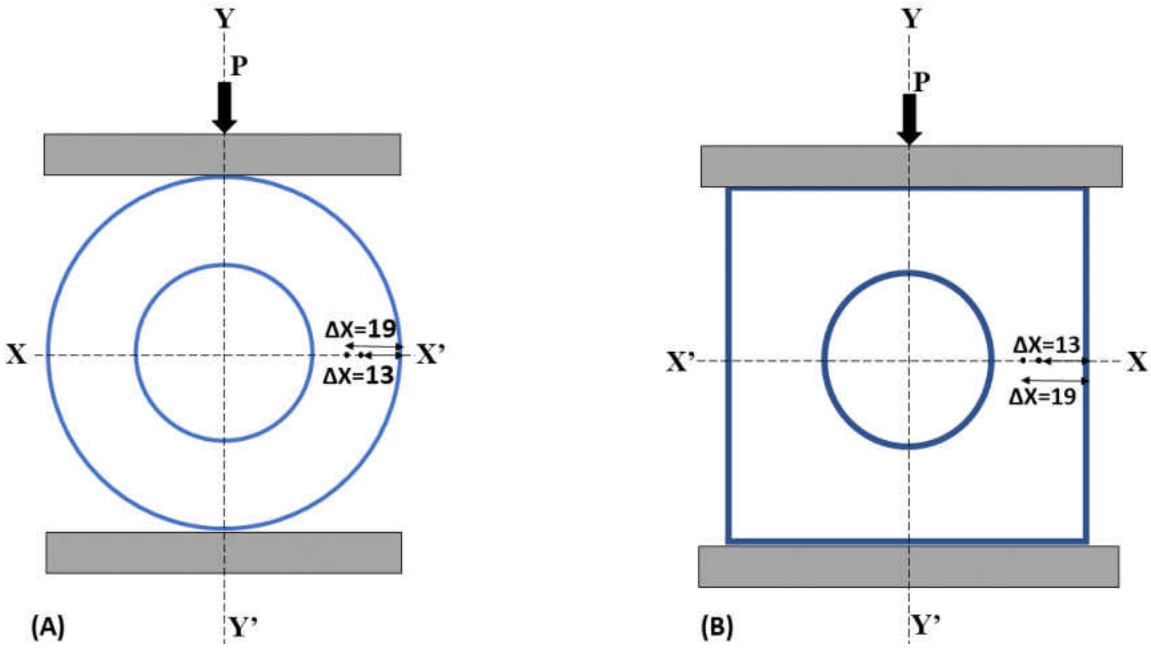

Figure 3.46 Location of Strain Measurement on Different Specimens along X-axis.

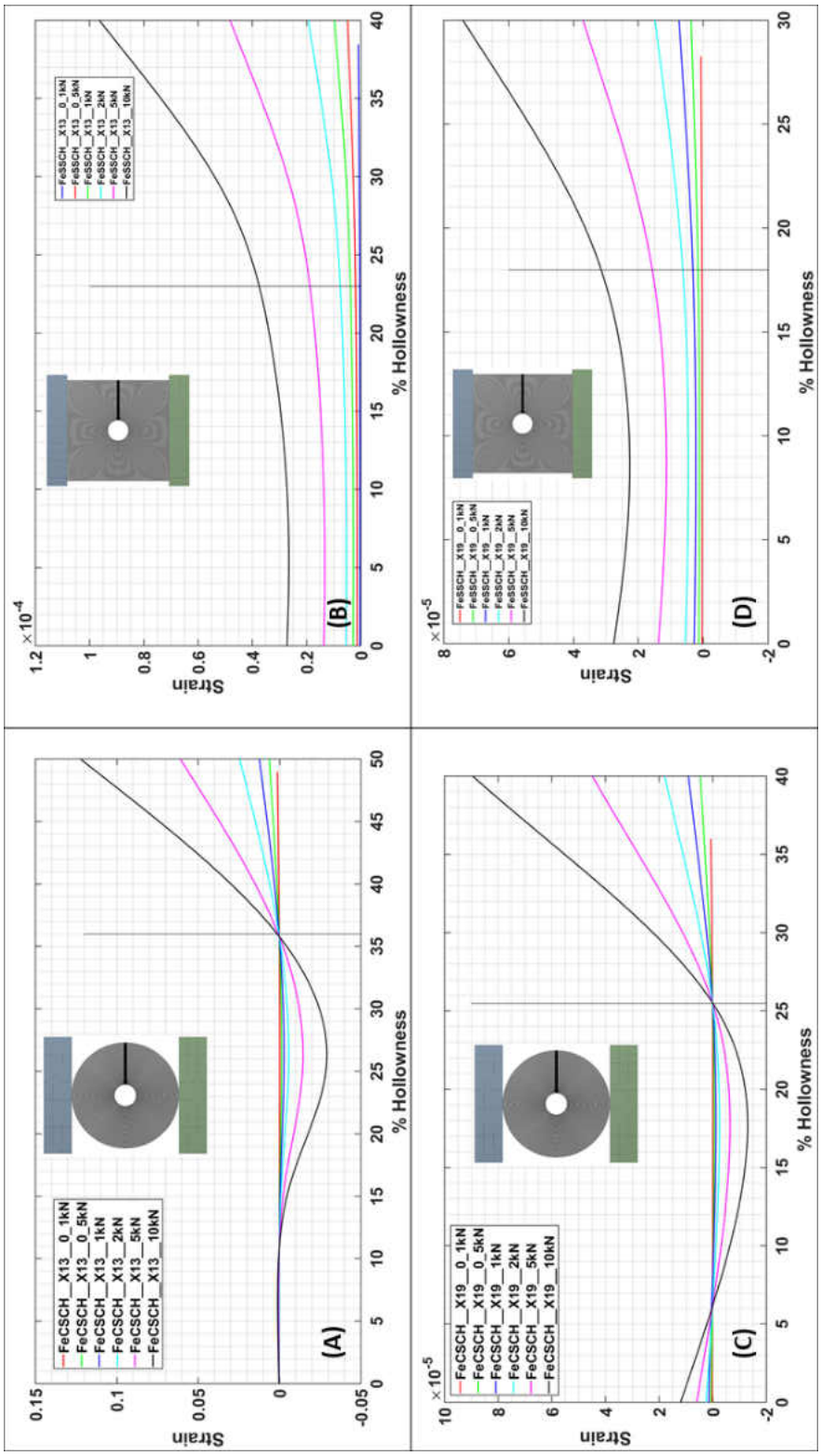

Figure 3.47 Strain Variation along X-Axis. (A) CS_CH_ΔX=13 (B) SS_CH_ΔX=13 (C) CS_CH_ΔX=19 (D) SS_CH_ΔX=19

3.4. Contact Stress Variation

Finite Element Models were created for contact stress analysis, as contact stress is the most critical factor that determines rolling contact fatigue life of components in rolling contact.

3.4.1 Preprocessing

It describes the modeling and meshing techniques.

A. **Models.** 2D half symmetric surface models were created in ANSYS Workbench® for contact stress investigation. The roller model had diameter of 5.5 inches whereas, the specimen models had a diameter of 1.5 inches. Both roller and specimen models had a thickness of 0.5 inches. The hole size for the specimens were increased for different hollowness percentages. A total of 10 FE models were created for percentage hollowness ranging from 0 to 81 as shown in Figure (3.48). The material assignment for both of the rollers and specimens is Structural steel. Frictionless contact was created between the specimen and rollers to imitate the experimental conditions that will be discussed in Chapter 4. Since the lubrication between rollers and specimens in the experiment will be under Elasto-hydrodynamic regime, the friction is considered to be negligible.

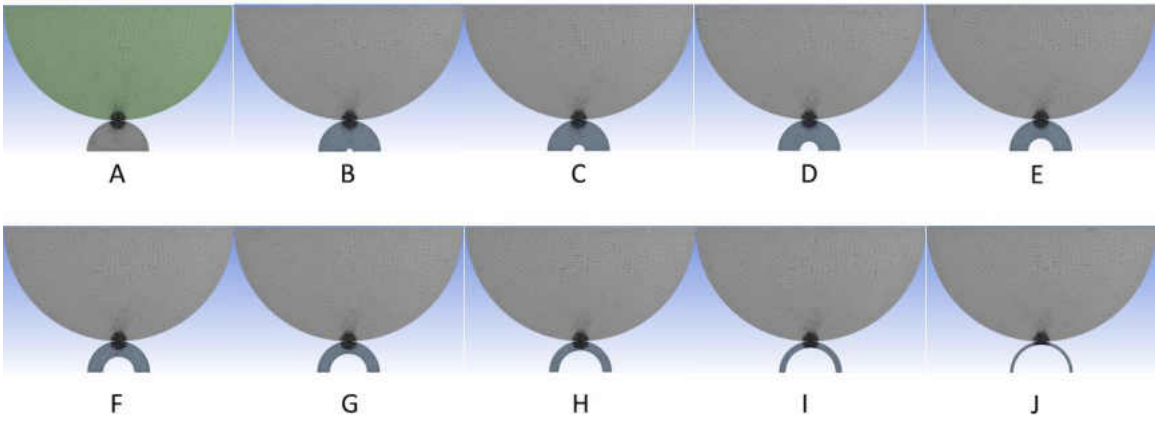

A: Solid Specimen (0% Hollowness)	B: Specimen (1% Hollowness)	C: Specimen (4% Hollowness)	D: Specimen (9% Hollowness)	E: Specimen (16% Hollowness)
F: Specimen (25% Hollowness)	G: Specimen (36% Hollowness)	H: Specimen (49% Hollowness)	I: Specimen (64% Hollowness)	J: Specimen (81% Hollowness)

Figure 3.48 2-D Finite Element Models with Different Hollowness.

B. Mesh. The models were fine meshed using face meshing tools. A sphere of influence was created at the contact point of radius 5mm and the element size of 0.025mm. This generated a very fine mesh in the zone of contact. The maximum value of shear and von Mises stresses are observed around 0.7b below the contact surface where b is the half contact width for cylinders in contact, as shown in Figure (2.8) [54.]. A very fine mesh is created with the sphere of influence at the contact. Figure (3.49) shows details of the fine mesh created with sphere of influence of diameter 5 mm at the contact surface. For the FEA of the created models, mesh metrics were obtained with small element sizes for the rollers and specimens. These values presented in Table (3.3), are within the recommended range for each of the mesh metrics. Finite element convergence plots for contact stress on solid and hollow specimens with 10% hollowness have also been added in Appendix C.

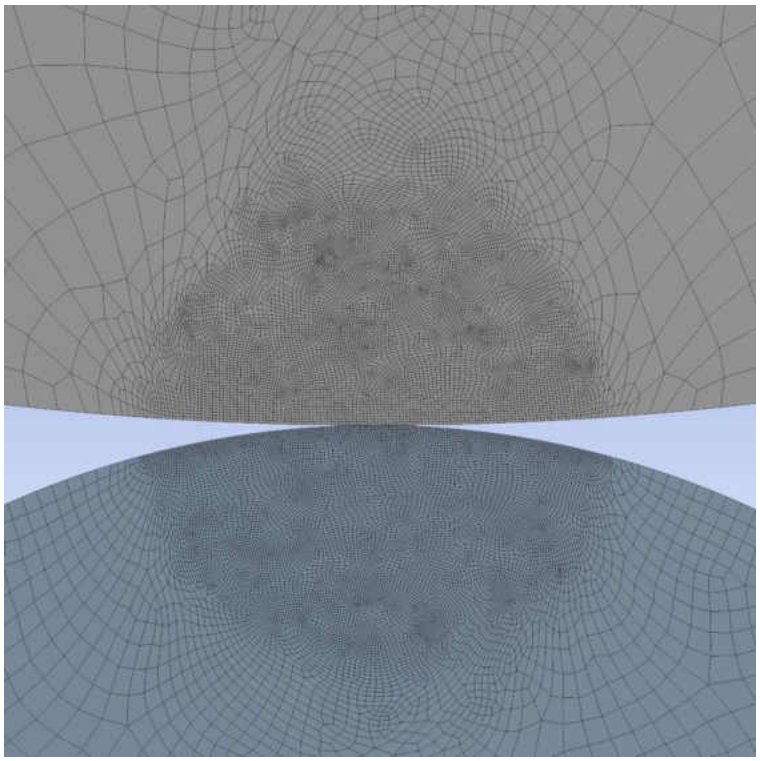

Figure 3.49 Fine Meshing at Contact Surface with Sphere of Influence

Contact stress analysis is non-linear and involves careful selection of contact elements. The contact surfaces between the roller and specimens are made up of contact elements. For flexible-flexible contact between the roller and specimen, the roller surface is made up of TARGE169 elements whereas, the specimen surface is made up of CONTA172 elements. CONTA172 are 2-D 3-Node Surface to Surface contact elements overlaid on the surfaces that deform under contact. They have two degrees of translational freedom along X and Y at each of the nodes. These elements are paired with TARGE196 elements to represent general contact. Any translational or rotational displacement can be imposed on the TARGE169 elements. 2-D segments on the TARGE169 are defined by the target shape codes which indicate the geometry of the elements. For the cylinder on cylinder contact

surface, these TARGE169 element are arc shaped having 3 nodes with 2-translational degrees of freedom on each of them.

Table 3.3 Mesh Metrics for Finite Element Models.

% Hollowness	0	1	4	9	16	25	36	49	64	81
No. of Elements	23562	23701	23819	23229	23444	23834	23282	22639	21439	18028
Element Quality	0.91	0.92	0.92	0.9	0.92	0.9	0.92	0.9	0.92	0.9
Aspect Ratio	1.38	1.38	1.36	1.4	1.37	1.4	1.35	1.4	1.35	1.3
Jacobian Ratio	1.3	1.3	1.3	1.3	1.3	1.3	1.29	1.3	1.29	1.3
Parallel Deviation	9.57	9.91	9.82	9.9	9.83	9.4	9.6	9.7	9.64	9.3
Maximum Corner Angle	105.4	104	104.3	104	104.4	104	103.81	104	103.68	103
Skewness	0.19	0.17	0.17	0.2	0.17	0.2	0.17	0.2	0.17	0.2
Orthogonal Quality	0.95	0.96	0.96	1	0.96	1	0.96	1	0.96	1

C. Loading and boundary conditions. For the 2D symmetric FE models created, the top edge of the roller was loaded in negative Y-direction with 1500N. The bottom edge of the specimen was supported with frictionless support. The outer circular edge of the roller was constrained to only displace along Y-axis. The loading and boundary conditions are shown in Figure (3.50).

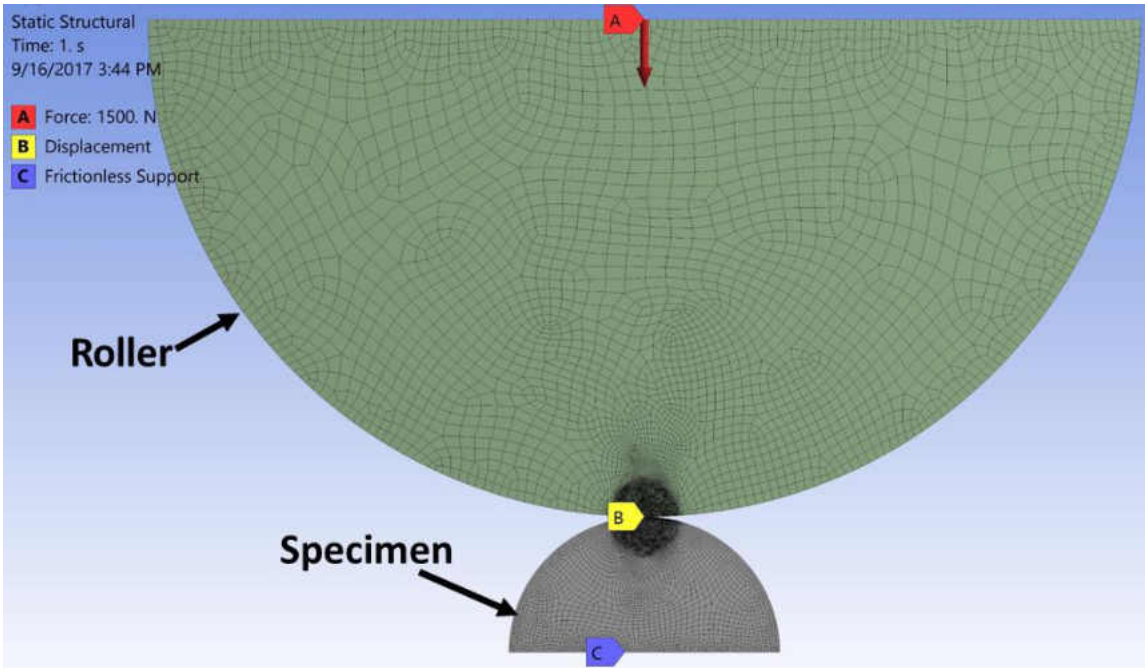

Figure 3.50 Loading and Boundary conditions FEA on Roller and Specimen.

3.4.2 Postprocessing

The solid model created on ANSYS Workbench® and the results from the FEA were validated with theoretical calculations. The following variables are defined as per the actual specimens and rollers manufactured for the experiment for RCF.

Load $(P) = 1500N$

Contact Width $(l) = 0.5\ inches$

Modulus of Elasticity for Roller $(E_1) = 210\ Gpa$

Modulus of Elasticity for Specimen $(E_2) = 210\ Gpa$

Diameter of Roller $(D_1) = 5.5\ inches$

Diameter of Specimen $(D_2) = 1.5\ inches$

Poisson's Ratio for Roller $(v_1) = 0.3$

Poisson's Ratio for Specimen $(v_2) = 0.3$

Using Eqn. (2.8), (2.9) and (2.10), we get

$P_{max} = 538.3$ Mpa

From FEA results for the solid specimen model, the contact pressure is,

$P_{maxFE} = 490.87$ Mpa

Difference in results

$$\Delta_{pmax} = \frac{P_{max} - P_{maxFE}}{P_{max}} \times 100$$

$$\Delta_{pmax} = 8.811\%$$

In finite element analysis, a result variation of within 10% is acceptable. Thus, from the above results, our FE model is validated for contact analysis.

After solving the FE models, results for Contact Stress, Equivalent Stress and total deformation were extracted for each of the cases and analyzed.

3.4.3 Results

From the finite element contact stress analysis, contact stress, equivalent stress and total deformation values for the specimen with different hollowness were obtained. They were

then plotted against percentage hollowness. Figure (3.51) shows the variation of contact stress with the change in hollowness in specimens. Contact stress value decreases with the increase in hollowness, validating the initial assumption that hollow specimens are better than the solid ones on contact loading. Contact stress value decrease significantly beyond 60% hollowness, possibly because the specimen is crushed under the compressive loading.

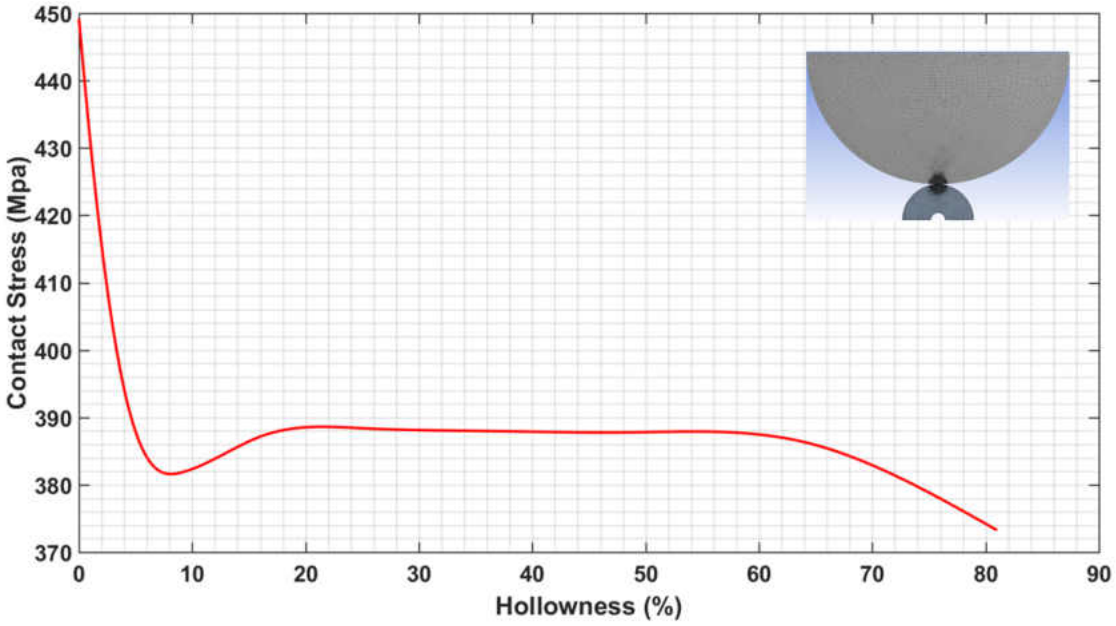

Figure 3.51 Contact Stress Variation with Hollowness.

The contact patch variation on increasing hollowness is shown in Figure (3.52). The actual region for sticking during the contact loading is increased once the hollowness of specimen increases. Figure (3.53) and Figure (3.54) present the variation of Equivalent von-Mises stress and total deformation on the specimens during the normal compressive loading through rollers respectively. Equivalent stress, though decreases minimally at the initial values of hollowness, it rises sharply beyond 40% hollowness. Similar is the case with total deformation on the specimen. This indicates that the chances of failure are very high

beyond 40% hollowness in those specimens. Significant rise in deformation beyond 40% hollowness is an indication of the material being possibly crushed under the normal compressive loading.

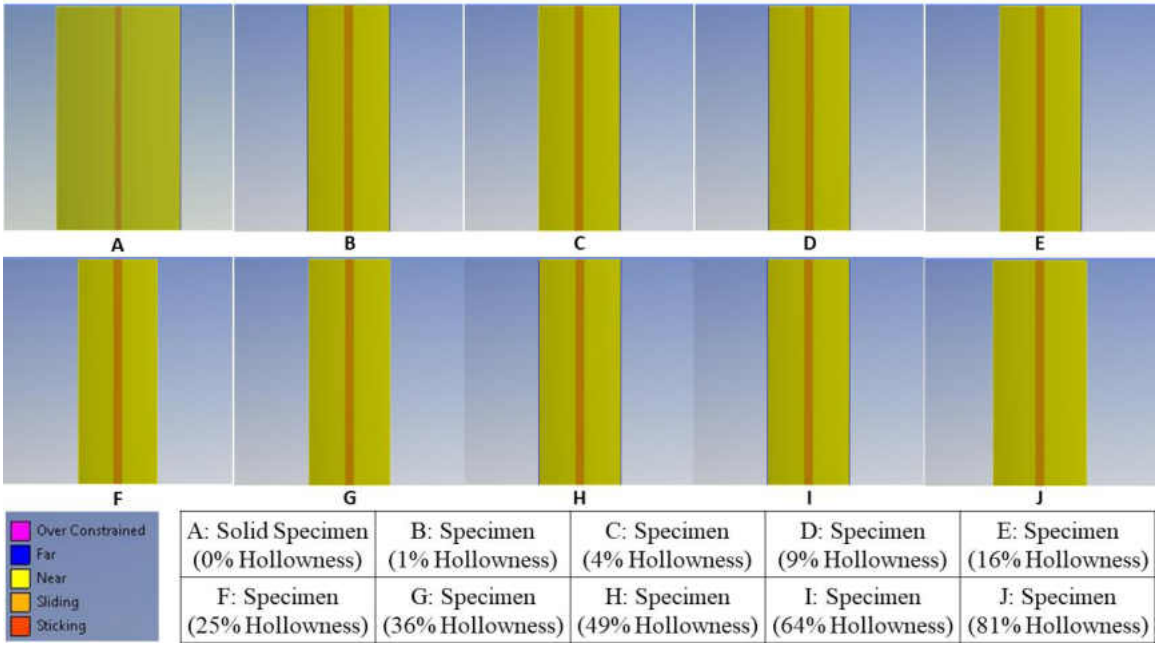

A: Solid Specimen (0% Hollowness)	B: Specimen (1% Hollowness)	C: Specimen (4% Hollowness)	D: Specimen (9% Hollowness)	E: Specimen (16% Hollowness)
F: Specimen (25% Hollowness)	G: Specimen (36% Hollowness)	H: Specimen (49% Hollowness)	I: Specimen (64% Hollowness)	J: Specimen (81% Hollowness)

Figure 3.52 Contact Patches between Roller and Specimen from FEA.

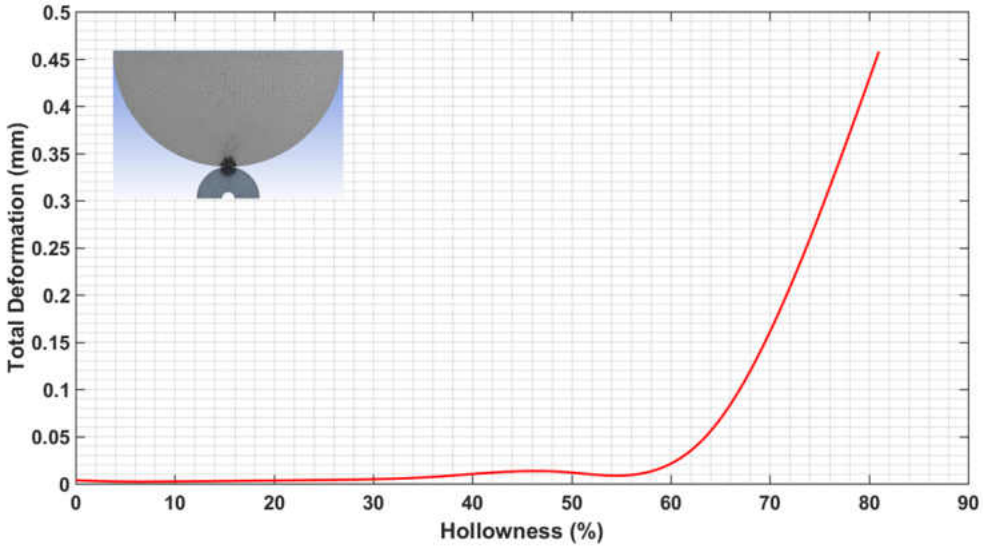

Figure 3.53 Equivalent Stress Variation with Change in Hollowness.

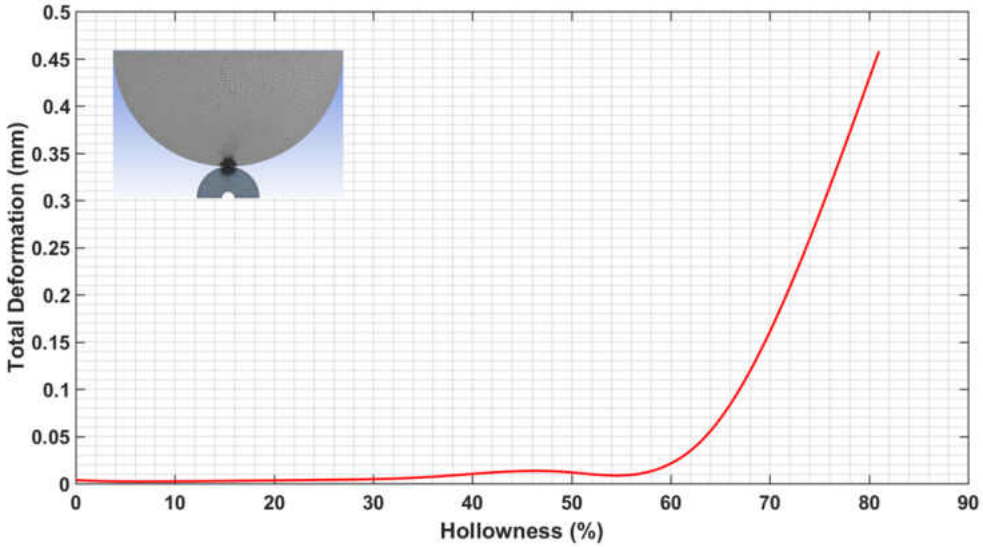

Figure 3.54 Total Deformation Variation with Change in Hollowness.

CHAPTER 4

EXPERIMENTAL INVESTIGATION

4.1 Overview

This chapter first presents the experimental part of the strain investigation on different specimens and then discusses the experiment for rolling contact fatigue life test. It provides a detailed description of the experimental setup, reasons behind the design and selection of test specimens and then explains the experimental procedure for strain investigation on circular and square discs and hollow load bearing specimens for RCF testing. Even though the experiment for RCF failed, the setup and testing procedure are discussed. This chapter provides details of different components of the test setup ranging from loading, data acquisition to data processing. Finally, it presents the results obtained from the experiments conducted.

4.1 Hollowness Under Normal Loading

Machine components fail due to various reasons. Failure is the state where a component cannot satisfactorily perform its function and thus loose its usefulness. This particular work is focused on failure due to higher stress on a component leading to its deformation. Higher

stress induced on any component, changes its material property or shape, thus making it unfit. Precise measurement of stress involves measurement of deformation of the work piece under any particular loading. The measured deformation is used in analytical calculations to get local stress. The biggest challenge in finding local stress with this approach is measuring deformation that might be very small in magnitude. Strain is the ratio of change in length to the original length. Most commonly used method to find local stress value is to measure strain over a finite length of work piece and then use the stress-strain relation for the particular material to convert strain value to local stress. With a small length of measurement, the value of strain measured becomes very close to the theoretical strain. Strain measured by this technique is mean deformation per unit length of specimen considered. Smaller the length considered, smaller will be the strain and measurement of such smaller value will again be a challenge. Thus, experimental design for measuring strain involves a careful selection of measuring instrument that is able to detect and measure the deformation, and the material that can undergo measurable deformation under the applied load. Electrical-resistance strain gages are the most commonly used devices for strain measurement.

Experimental setup was designed to investigate the stress distribution and effect of hollowness on the stress field in machine component. As per Hooke's Law, stress induced is directly proportional to the strain until the elastic limit; therefore, strain measurement was the basis for the experiment. Aluminum specimens were chosen as they are easier to machine and would induce significant strain on application of smaller load than steel. Electrical-resistance foil strain gages were used for strain measurement as they are small, light, and adhere easily on the aluminum surfaces. In addition, these strain gages do not

influence the property of metals. The aluminum specimens were cut to square and circular cross sections out of a 0.5-inch-thick plate. The outer diameter of circular specimen and the outer edge length for the square specimen were both 5 inches. Different sized center holes were cut into these specimens. Fourteen specimens were made as detailed in the Table (4.1) and Figure (4.1).

Table 4.1 Aluminum Specimen Details.

S. N	Cross Section of Specimen	Notation	Outside Dimension (inches)	Hole Dimension (Diameter/Edge Length) (inches)	Hollowness (%)
1	Square	SS_CH_1	5	0	0
2	Square	SS_CH_2	5	1	3.14
3	Square	SS_CH_3	5	1.5	7.07
4	Square	SS_CH_4	5	2	12.57
5	Square	SS_CH_5	5	2.5	19.64
6	Square	SS_CH_6	5	3	28.27
7	Square	SS_CH_7	5	3.5	38.49
8	Circular	CS_CH_1	5	0	0
9	Circular	CS_CH_2	5	1	4
10	Circular	CS_CH_3	5	1.5	9
11	Circular	CS_CH_4	5	2	16
12	Circular	CS_CH_5	5	2.5	25
13	Circular	CS_CH_6	5	3	36
14	Circular	CS_CH_7	5	3.5	49

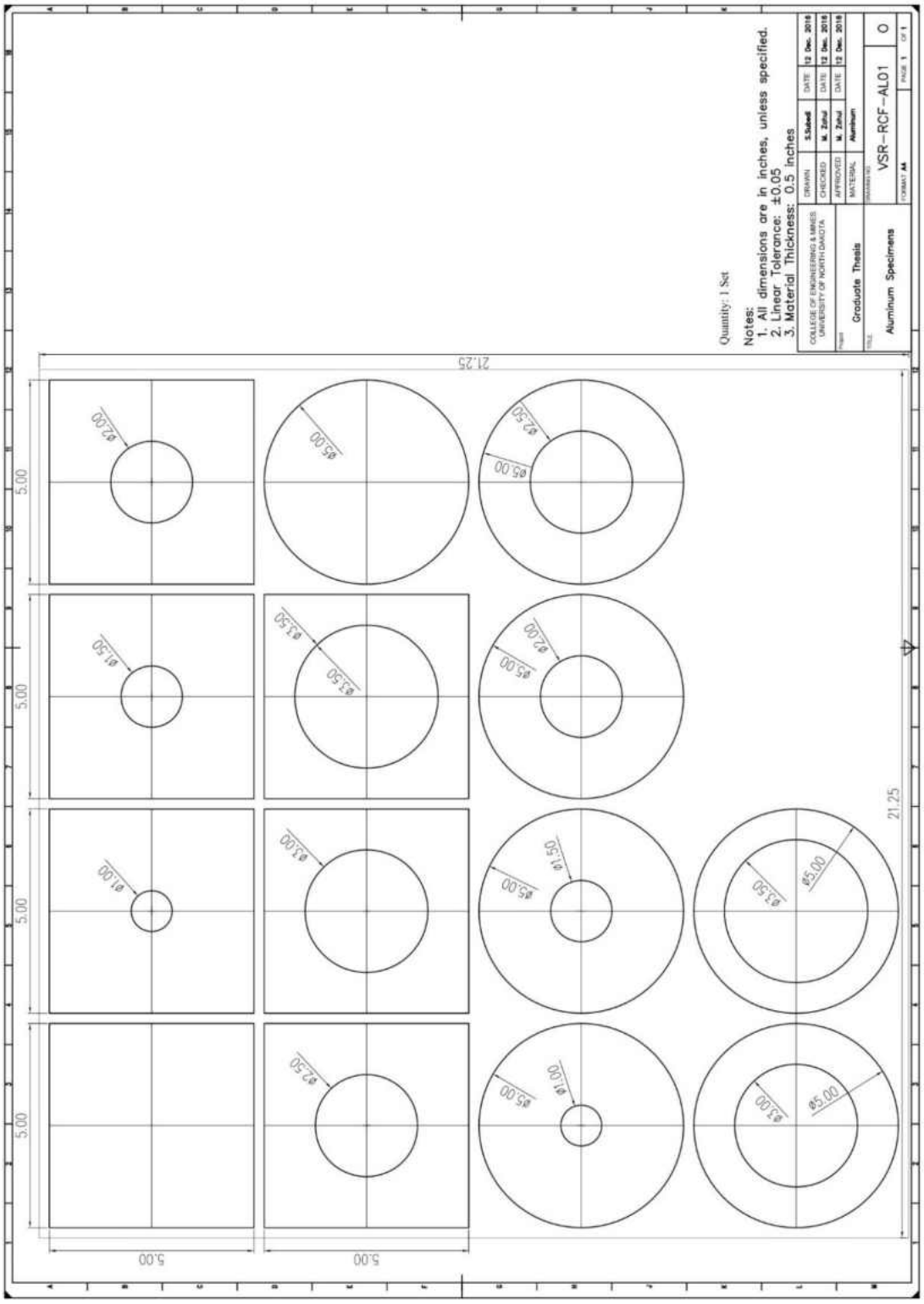

Figure 4.1 Aluminum Specimens for Hollowness Tests.

The manufactured specimens are shown in Figure (4.2). These 0.5-inch-thick specimens were cut with waterjet cut to a precision of 0.01inches.

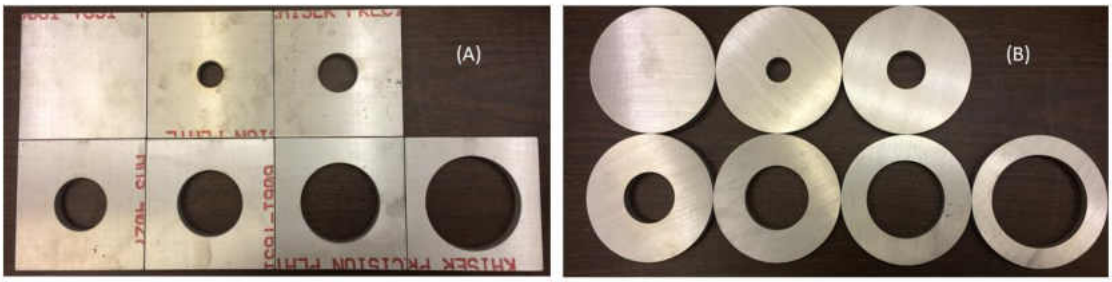

Figure 4.2 Specimens for Experiment. (A) Square specimens with circular holes (B) Circular Specimens with Circular Holes

4.1.1 Test Setup

A test setup was designed for loading and obtaining strain data during the test. The test setup comprises of the following two systems,

A. **Loading System**. Shimadzu 50kN Universal Testing Machine was used to load the specimens. A 50kN load cell was used for the compression tests. Special fixtures were manufactured to attach the load cell. Adjustments were made on the loading heads of UTM to ensure that the loading axis of the UTM is normal to the loading cross section. This is essential to ensure normal axial loading and prevent bending or torsion loading in the specimen. A load based compression test module was created in the Trapezium Z Material Testing software from Shimadzu to apply load at a rate of 10N/s. The experimental setup used is shown in Figure (4.3).

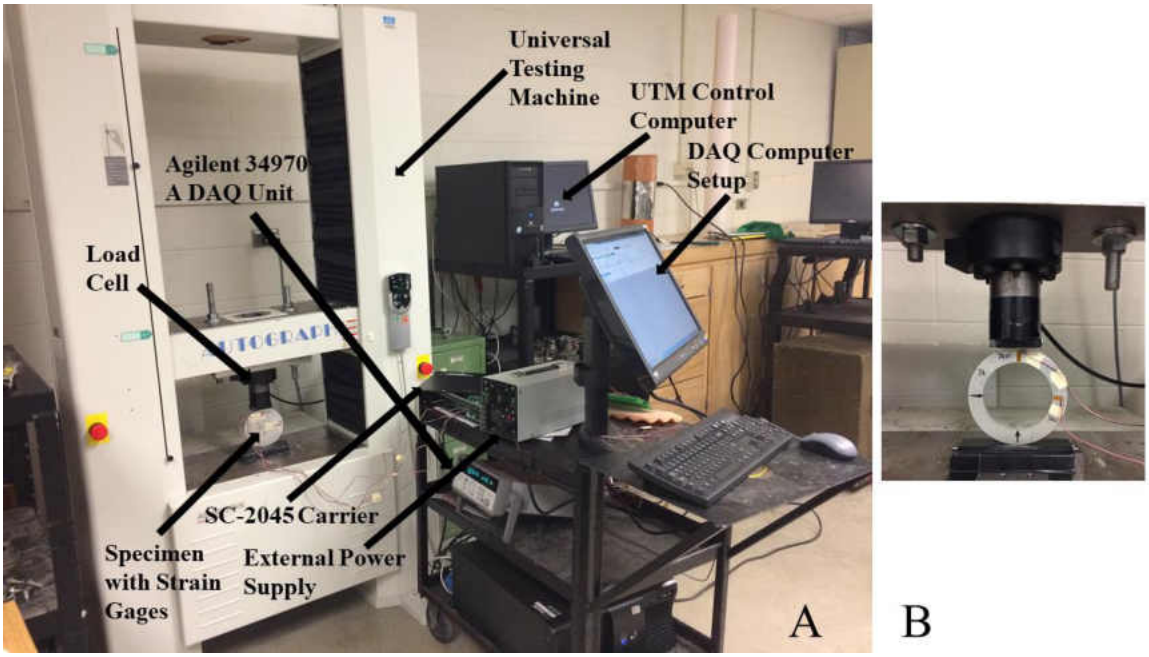

Figure 4.3 Experimental Setup for Strain Investigation. (A) Experimental setup for strain investigation (B) Close up View of the Specimen with Strain Gages.

B. Data Acquisition System. This system primarily consists of all the system components used in the experiments for measuring, acquiring and saving the strain data. Figure (4.4) shows various components of the data acquisition system. It consists of the following components,

i. ***Strain gages.*** Strain gages are strain-sensitive alloy wires arranged in foil grid pattern, with a known resistance value. Resistance of a wire is dependent on its length, cross section area and the resistivity of the material of composition. For a change in length of wire, its resistance changes accordingly. Resistance is thus, linearly proportional to the strain on the foil grid wire of strain gage. Not just the strain gage material, but also the specimen material on which the gauge is mounted, are both sensitive to temperature, causing a change in

length/area of the gauge. Thus, there is a need for temperature compensation to counter for the thermal sensitivity of the strain gage and the specimen.

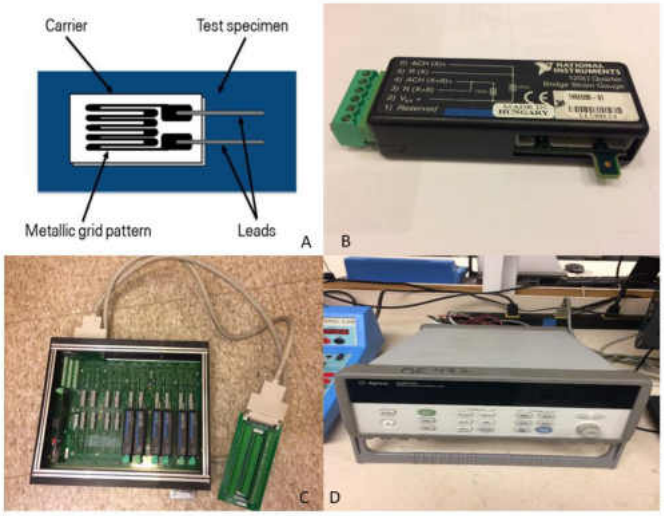

A	Micro-Measurement Strain Gage
B	Strain Gage Module SCC_SG-01
C	SC-2045 Carrier with CB-68LPR terminal connector block and SH68-68 NI Shielded cable.
D	Agilent 39740 A DAQ Unit

Figure 4.4 Components of a Data acquisition system.

To measure such small strain values and to compensate for temperature sensitivity, strain gages are always used in bridge configuration with a voltage or current excitation source [55]. Gage factor(G_f) is the ratio between fractional change in resistance to strain, provided by Eqn. (4.1)

$$G_f = \frac{\frac{\Delta R}{R}}{\frac{\Delta \epsilon}{\epsilon}} \tag{4.1}$$

A typical Quarter bridge configuration type Wheatstone bridge is shown in Figure (4.5). It consists of two parallel voltage divider circuits with two resistors each. The voltage across the mid nodes is calculated using the following Eqn. (4.2).

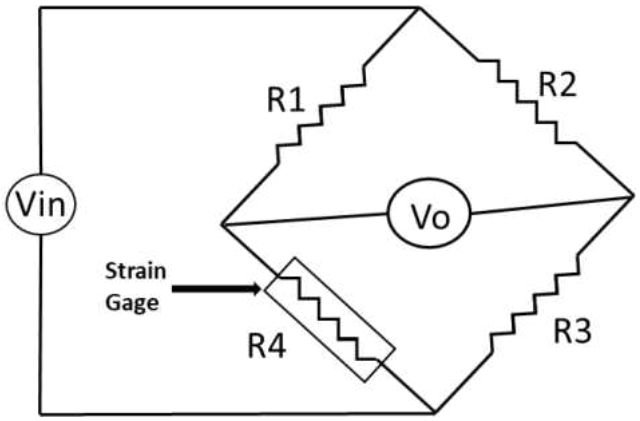

Figure 4.5 Quarter Bridge configuration of Wheatstone bridge.

$$V_o = \left[\frac{R_3}{R_2+R_3} - \frac{R_4}{R_1+R_4}\right] \times V_{in} \quad (4.2)$$

WheatStone bridge circuits are used for extremely accurate measurements. When all the resistors are equal, the voltage across the mid nodes (V_o) is zero. For the quarter bridge configuration, one leg of the WheatStone bridge is replaced with the strain gage as shown in Figure (4.5). When there's a specimen deforms, voltage changes in the circuit. This change in voltage (ΔV) is measured using a voltmeter and converted to strain $(\in)$ using Eqn. (4.3).

$$\in = \frac{4\Delta V}{G_f \times V_{in}} \quad (4.3)$$

Micro Measurement CEA Series Strain Gages manufactured by MicroMeasurements were used for the experiment due to their ease of installation and lead wire attachment, for axial strain measurement [56]. These are highly precise gages with a gage factor of 2.1±0.5% and resistance of 120±0.3%.

ii. ***Strain gage modules.*** Quarter Bridge Type-I SCC-SG01 module from National Instruments with 3-wire configuration is used to measure axial strain on the specimens [57]. A 3-wire connection can eliminate the effects of variable lead-wire resistance because lead resistance affects adjacent legs of the bridge [58]. With each resistor of 120Ω, a CEA series strain gage makes one leg of the compact Strain Gage module. For the experiment, six modules were mounted in the carrier for analog voltage input.

iii. ***Carrier.*** SC-2045 carrier from NI was used to mount the strain gage modules. These carriers can mount 20 SCC-SG modules, and provide multiple channel operation for multiple strain data. They have multiple configurable connectors to connect them to the DAQ devices. For the experiment, six SCC-SG01 strain gage modules were mounted for analog input. It was then, connected to 68-pin screw terminal connector block CB-68LPR using a SH68-68 NI Shielded cable.

iv. ***Data Acquisition Unit (DAQ).*** Voltage data for individual strain gages were extracted from the Terminal connector block, and fed to the input channels of Agilent 34970A Data Acquisition Unit. It has 20 channels that connect to the internal Digital Multimeter (DMM). The minimum level that the internal DMM can detect for a given measurement is known as sensitivity. It corresponds to the ability of the internal DMM to respond to minor change in the input level. The DMM consists of signal conditioning, amplification and a high resolution (up to 22 bits) analog to digital convertor [59].

v. ***Data Logger Software***. The voltage data acquired from the DMM in Agilent 34970 A DAQ are then scanned, collected and recorded using the Benchlink Data Logger Pro Software. The software is capable of multiple scans for real time data from multiple channels. These data are recorded and exported into excel [60].

Figure (4.6) shows the sample experimental specimens with strain gages mounted on them.

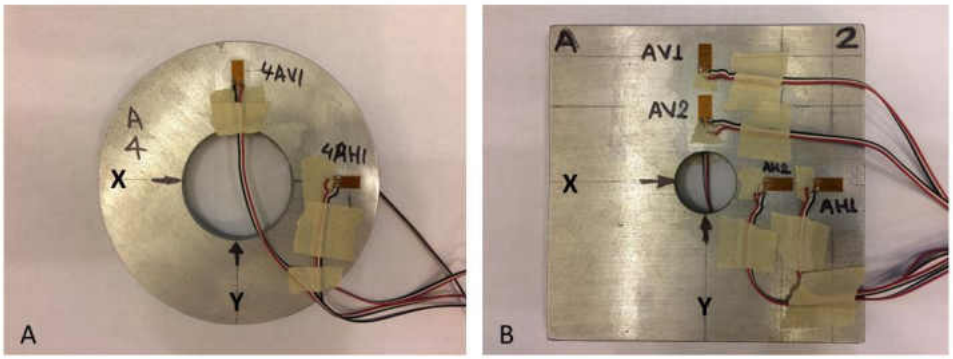

Figure 4.6 Two types of specimens with strain gages mounted on them.

4.1.2 Test Procedure

Strain gages were attached to the specimen surfaces as shown in Figure (4.6), as per the prescribed method. The number and location of strain gages on specimens were based on the size of the holes. Precision strain gauges were mounted on the specimens along two perpendicular axes to obtain strain information due to the applied load. Strain gauges were connected to the NI Strain Gauge modules (SCC-SG-01). 5V DC external power was supplied to the SC-2345 board. An ANSYS® simulation was carried out to determine the minimum load to apply to the specimen, based on the resolution of data acquisition system calculated using Eqn. (4.3) and Eqn. (4.4). A strain of 6.9E-06 was obtained at 19mm

distance from the edge along X-axis on the Circular Specimens with 0% hollowness for a 100N load from ANSYS® simulation.

$$Q = \frac{E_{FS}}{2^M} \quad (4.4)$$

E_{FS} is the full scale voltage of the device

M is the number of bits

A 20 Channel, 22-Bit Agilent (34970A) system with 24Volts full scale voltage was the best fit. It is capable of measuring up to 2.1798e-06 Volts. It was connected to a PC to acquire the voltage data from the strain gauges. Benchlink Data Logger Pro software was used to record the real-time data and export multichannel voltages into excel. Voltage data were recorded for each load and each sample. In-spite of all the efforts, there still were errors in the system, such as different length of wires, amount of solder, temperature variation during experiments, minor voltage fluctuations etc., so the Wheatstone circuits on the unloaded samples were not perfectly balanced. They were the major sources of error in the experiments.

Strain gages were mounted at three locations; 13mm (ΔX=ΔY=13) and 33mm (ΔX =ΔY=33), distance from the outside edges along both axes on the front side (A) of the specimen while the back side (B), had strain gages at locations 19mm (ΔX =ΔY=19), from the outside edge along both the axes as shown in Figure (4.7). Strain gages were connected to the Modules and the voltage data from them were fed to the Data Logger Pro using Agilent System. Maximum of six channels were scanned. Specimens were categorized based on the number of strain gages mounted.

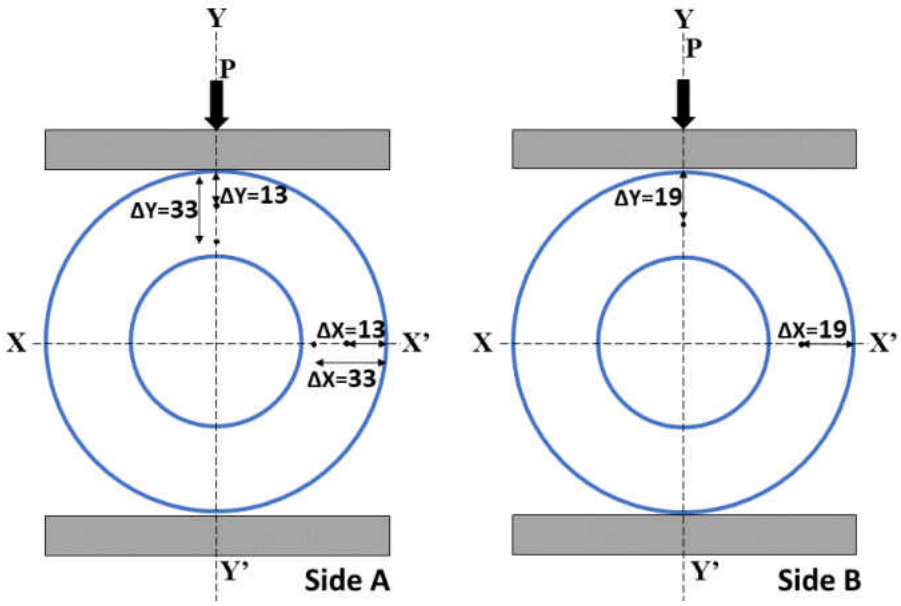

Figure 4.7 Strain Gage Mounting locations on Two Sides of Circular Specimens.

Table (4.2) shows the category of specimen, channels and location of strain gage on different specimens. Firstly, the experiments were carried out on the Square specimens.

For circular specimens, strain data was measured at only two points along each axis, 13mm and 19mm distance from the outer edges. Y is the loading axis and X is the axis perpendicular to Y on the front, and back faces. Voltage readings were scanned for load values of 0N, 100N, 500N, 1000N, 2000N, 5000N, 10,000N. Though, 6 strain gages were mounted on the square specimens at 13mm,19mm, and 33mm distances from outer edges along X and Y-axis only 4 out of 7 specimens could accommodate the 3rd strain gage at 33mm because of the size of holes. This led to shortage of data points to analyze strain at those particular locations for different hollowness. Thus, they were not included in the results.

Table 4.2 Specimens and Input Channels for AGILENT DAQ.

Category	Specimens	Side	Axis	Strain Gage location	Input Channel for Agilent System	Code
1	SS_CH_1 SS_CH_2 SS_CH_3 SS_CH_4	A	Y	ΔY=13mm	102	AV1
				ΔY=33mm	103	AV2
			X	ΔX=13mm	104	AH1
				ΔX=33mm	105	AH2
		B	Y	ΔY 19mm	106	BV1
			X	ΔX=19mm	107	BH1
2	CS_CH_1 CS_CH_2 CS_CH_3 CS_CH_4 SS_CH_5 SS_CH_6 CS_CH_5 CS_CH_6	A	Y	ΔY 13mm	102	AV1
			X	ΔX=13mm	103	AH1
		B	Y	ΔY 19mm	104	BV1
			X	ΔX=19mm	105	BH1
3	SS_CH_7 CS_CH_7	A	Y	ΔY=13mm	102	AV1
			X	ΔX=13mm	103	AH1

4.1.3 Data Processing

Voltage readings for different load case for the strain gages were saved into excel. The initial readings from the strain gages were zeroed out to cancel the noise in the measurement and data acquisition system. The voltage values were then converted to strain using Eqn. (4.3). Strain values were then plotted against hollowness percentages using MATLAB®. The date was curve fitted with splines.

4.1.4 Results

Each specimen was loaded with different load values and the resulting strain data were recorded for each case. Normal strain obtained from experiment were plotted against hollowness to determine the optimum hollowness for the specific case of loading and location of measurement. Optimum hollowness is determined based on the pattern of variation of strain for different hollowness observed under increased loads. The value of percentage hollowness, where the graph for strain rises significantly, is taken as optimum value of hollowness. Dotted vertical lines on the plots represent corresponding optimum hollowness for the individual case of location of measurement and type of measurement.

A. **Strain Variation along X and Y-axis on Circular Specimen with Circular Holes.** Circular Specimens with Circular Holes (CS_CH) come under concentrated loading and concentric regular category. Figure (4.8) shows the specimen and location of strain measurement. Figure (4.9) to Figure (4.12) present strain variation at different location for circular specimens with circular holes for different loads applied. The measurement technique was consistent for all the experiments.

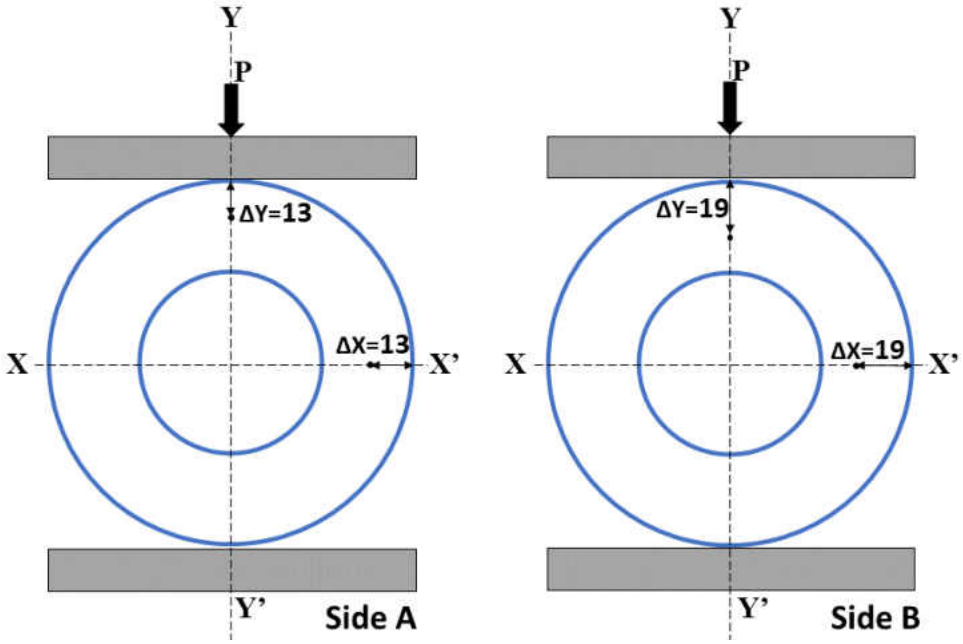

Figure 4.8 Strain Measurement Points on Circular Specimens with Circular Holes.

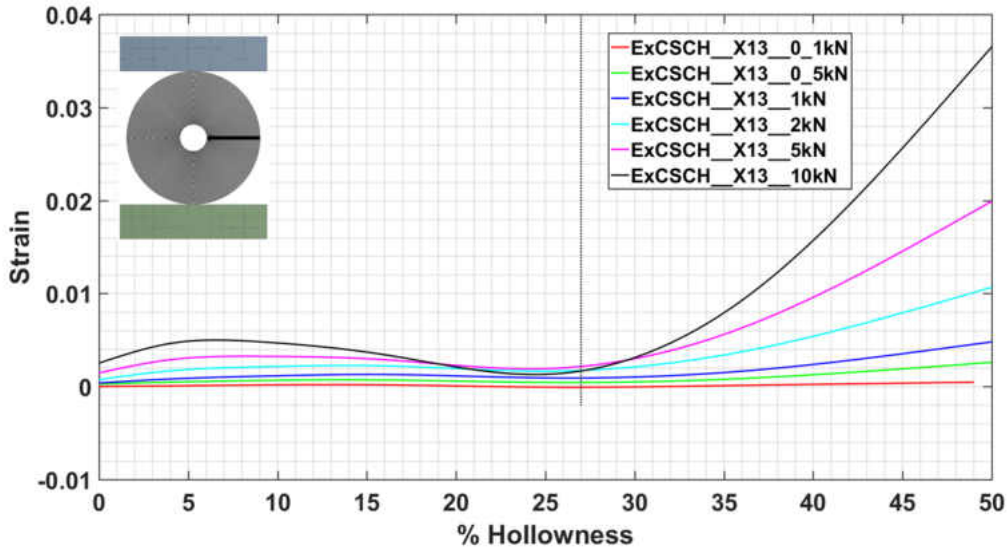

Figure 4.9 Strain Variation at ΔX=13mm on Circular Specimens with Circular Holes.

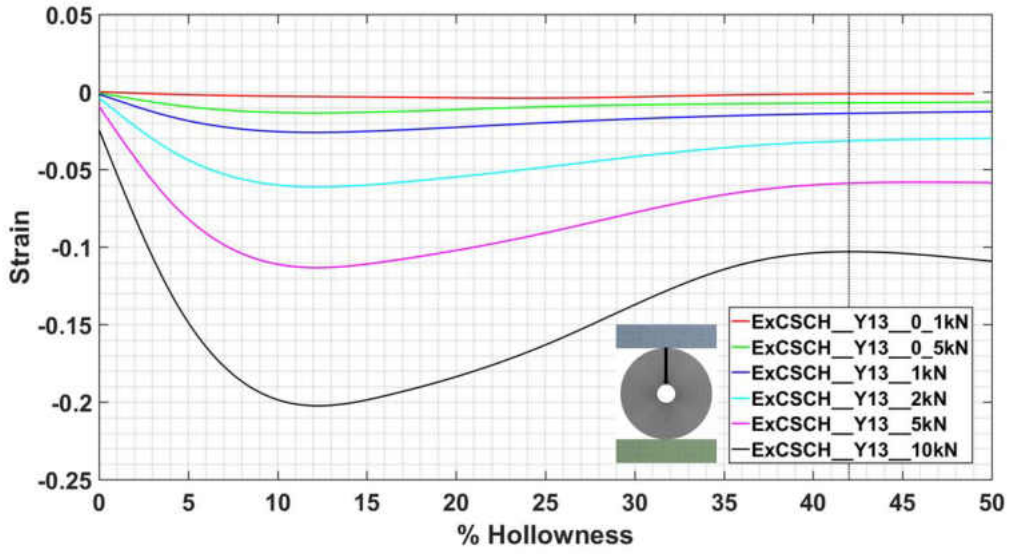

Figure 4.10 Strain Variation at ΔY=13mm on Circular Specimen with Circular Hole.

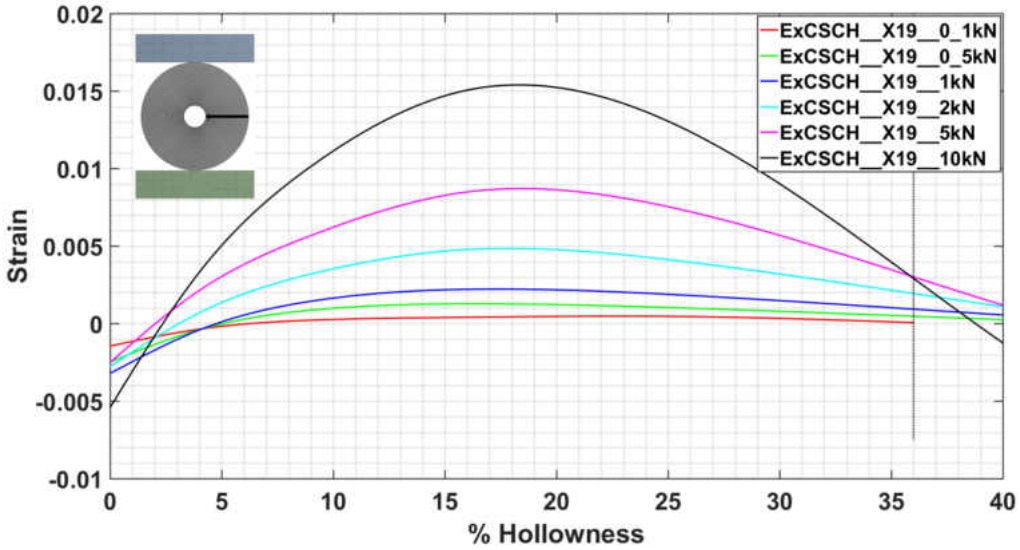

Figure 4.11 Strain Variation at ΔX=19mm on Circular Specimen with Circular Hole.

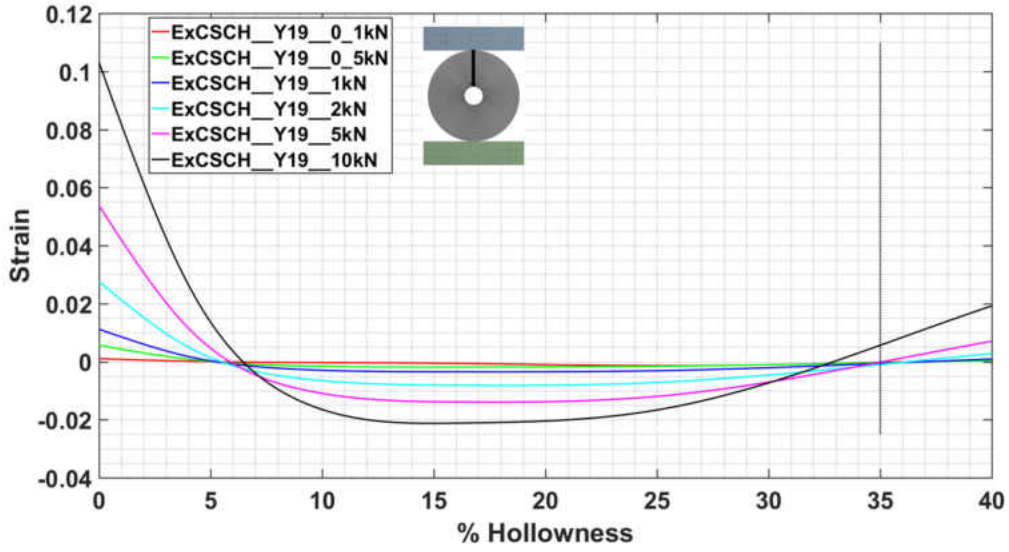

Figure 4.12 Strain Variation at ΔY=19mm on Circular Specimen with Circular Hole.

Figure (4.13) shows a comparison between experimental strain variation for circular specimens with circular holes along two different axes at two different locations. Strain variation at ΔY=13mm location and ΔY=19mm indicate an optimum hollowness around 40% whereas for ΔX=13mm and ΔX=19mm locations, optimum hollowness is between 25% to 40%. This shows that Circular specimens with concentric regular voids can be manufactured with a maximum hollowness of 40% without a significant increase in strain value.

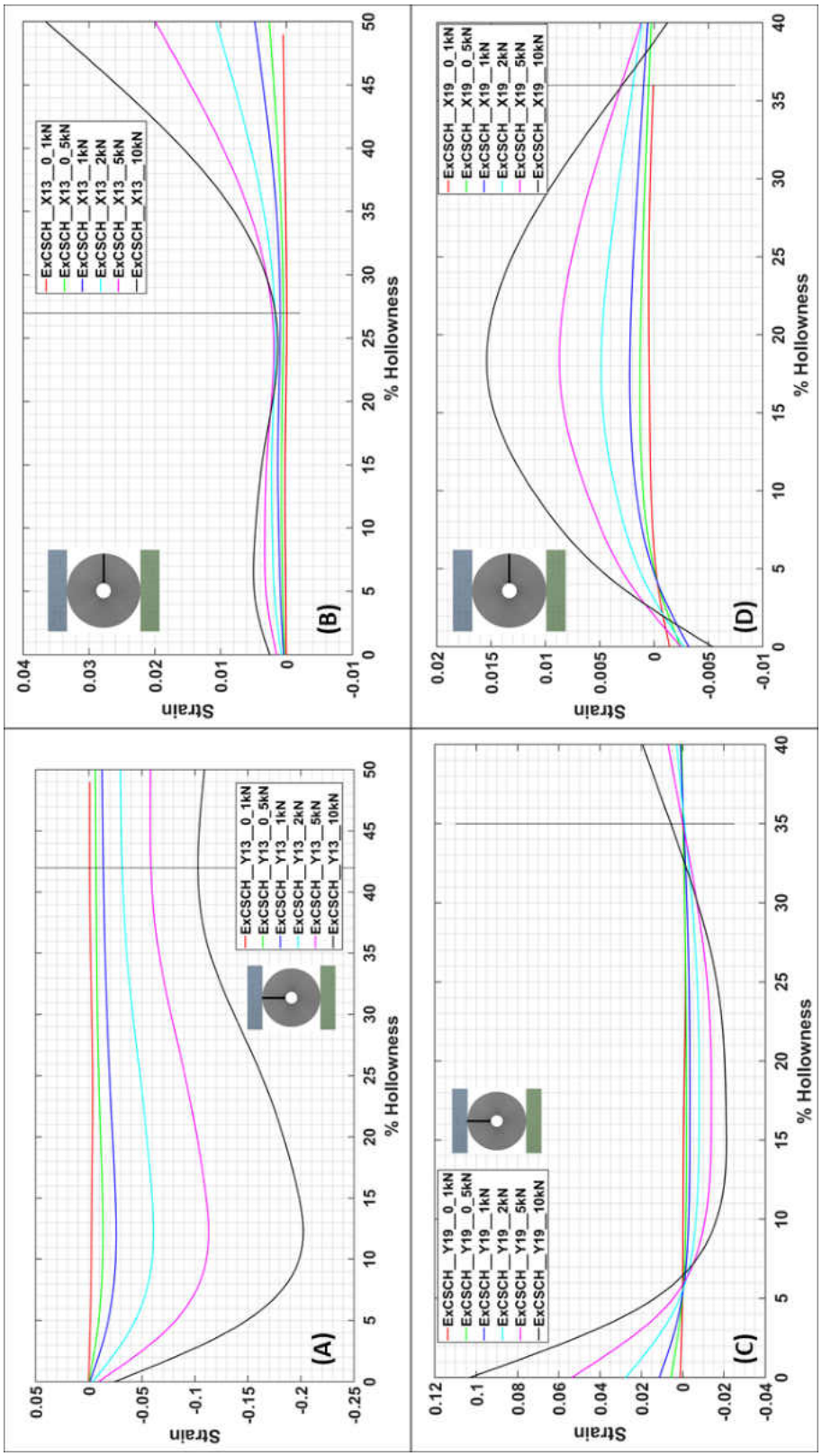

Figure 4.13 Strain Variation at Different Locations. (A) Δ=Y13mm (B) ΔX=13mm (C) ΔY=19mm (D) ΔX=19mm

B. Strain Variation along X and Y-axis on Square Specimen with Circular Holes.

Square Specimens with Circular Holes (SS_CH) come under distributed loading and concentric irregular category. Figure (4.14) show the loading and location of strain measurement on the specimens. Figure (4.15) to Figure (4.18) show the variation of strain for different loads against different hollowness percentages.

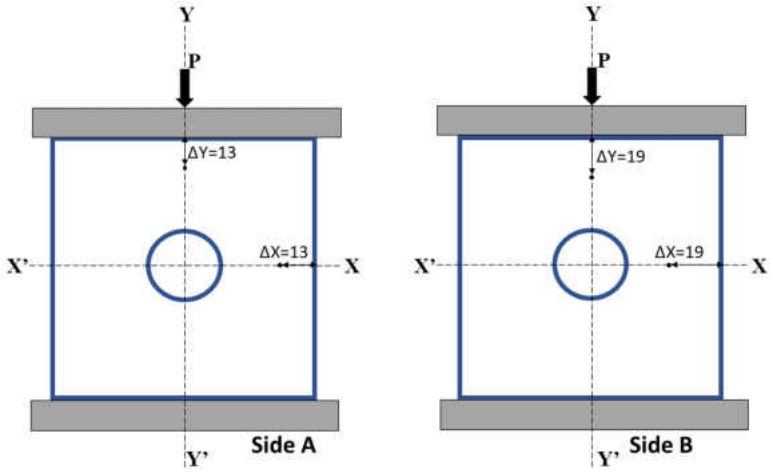

Figure 4.14 Strain Measurement Points on Square Specimens with Circular Holes.

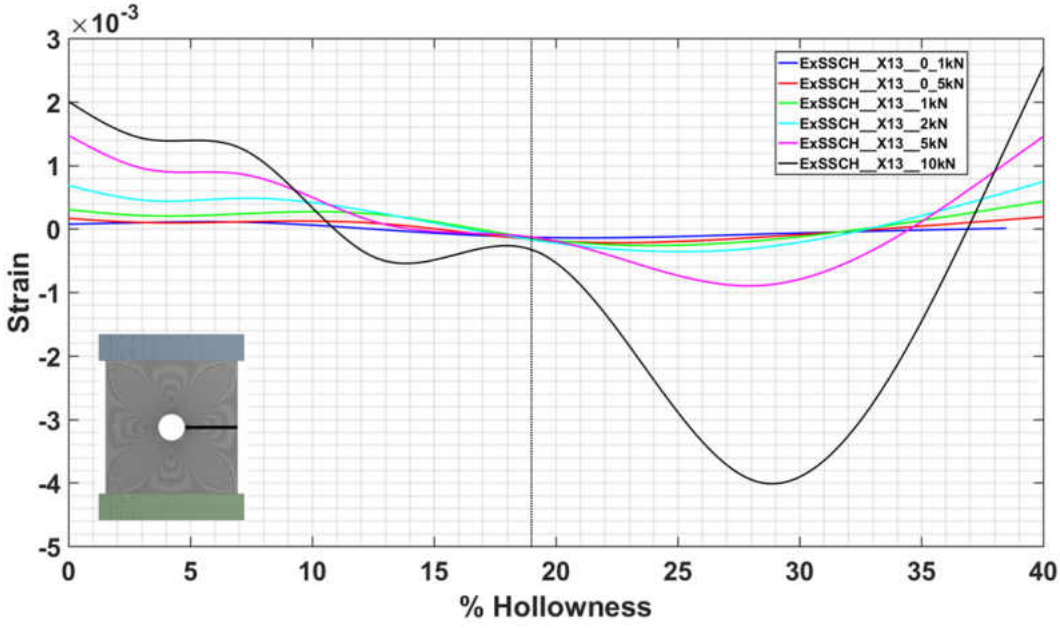

Figure 4.15 Strain Variation at ΔX=13mm on Square Specimens with Circular Holes.

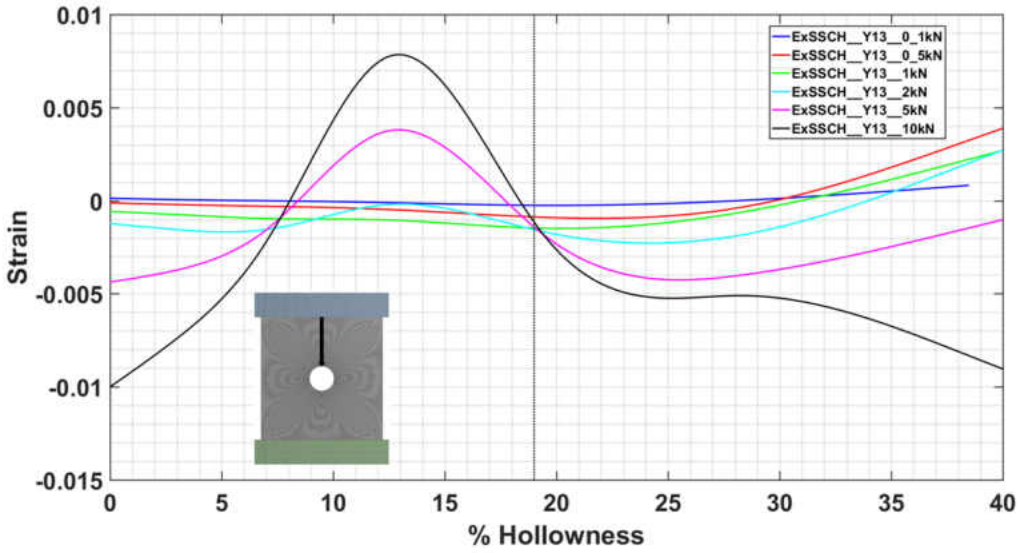

Figure 4.16 Strain Variation at ΔY=13mm on Square Specimens with Circular Holes.

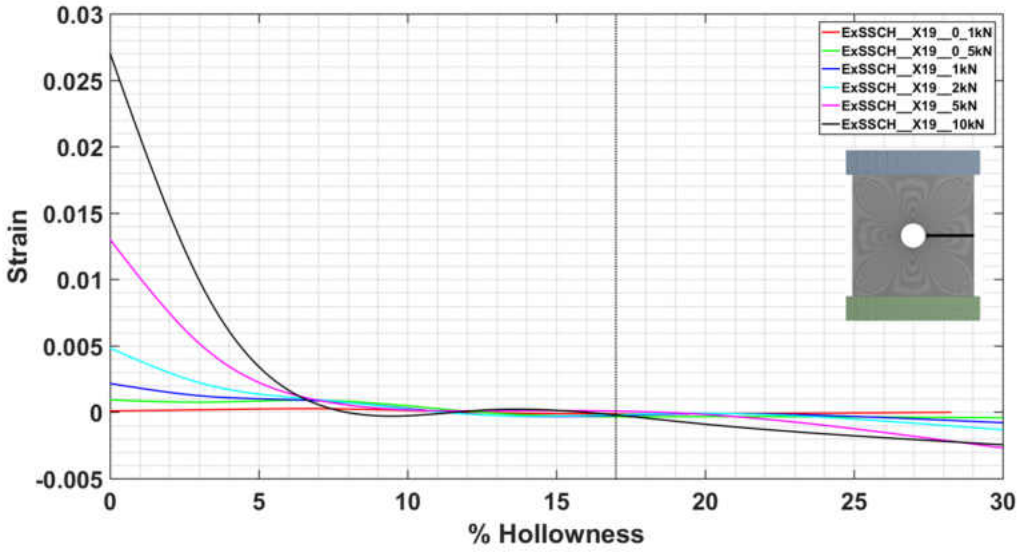

Figure 4.17 Strain Variation at ΔX=19mm on Square Specimens with Circular Holes.

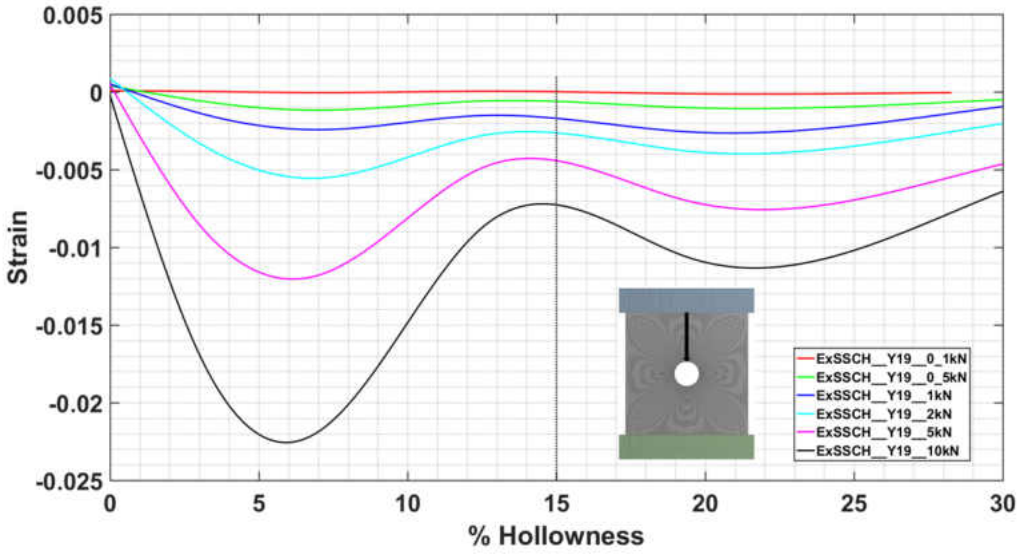

Figure 4.18 Strain Variation at ΔY=19mm on Square Specimens with Circular Holes.

Figure (4.19) shows a comparison between experimental strain variation for square specimens with circular holes along two different axes at two different locations. Optimum hollowness based on strain variation along Y-axis for around 20%. For ΔX=13mm and ΔX=19mm locations, optimum strain is observed at around 20% hollowness. This shows that square specimens with concentric irregular voids can be manufactured with a maximum hollowness of 20%, without significant increase in strain.

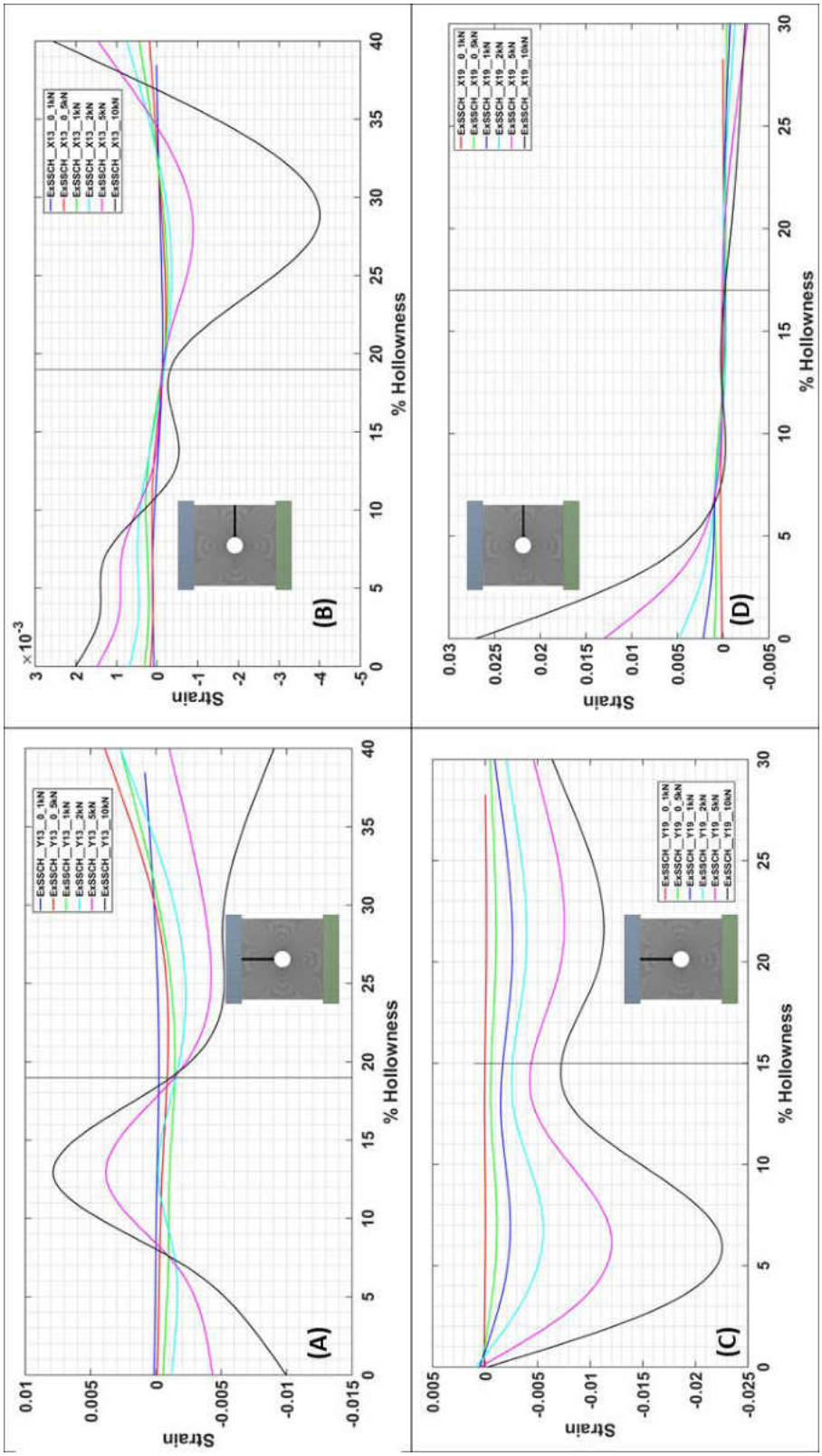

Figure 4.19 Strain Variation for Different Hollowness. (A) SS_CH_ΔY=13 (B) SS_CH_ΔX=13 (C) SS_CH_ΔY=19 (D) SS_CH_ΔX=19

C. Strain Variation for Specimens with Different Type of Voids under Different Types of Loads.

Results obtained after plotting the strain versus hollowness are now discussed based on the classification of specimens as discussed in Chapter 3.

i. Strain variation along Y-axis. Figure (4.20) shows the location of strain measurement on different type of specimens. The strain variation against different hollowness at 13mm (ΔY=13) and 19mm (ΔY=19) distance from outer edge along the loading axis are plotted in Figure (4.21). The plots on left are for strain variation along Y-axis for circular specimens with concentric circular holes under normal compressive loading. The strains rise steeply between 35% to 40% hollowness for these specimens. The plots on right are for strain variation along Y-axis for square specimens with concentric circular holes under normal compressive loading. The strains rise steeply between 15% to 20% hollowness for these specimens.

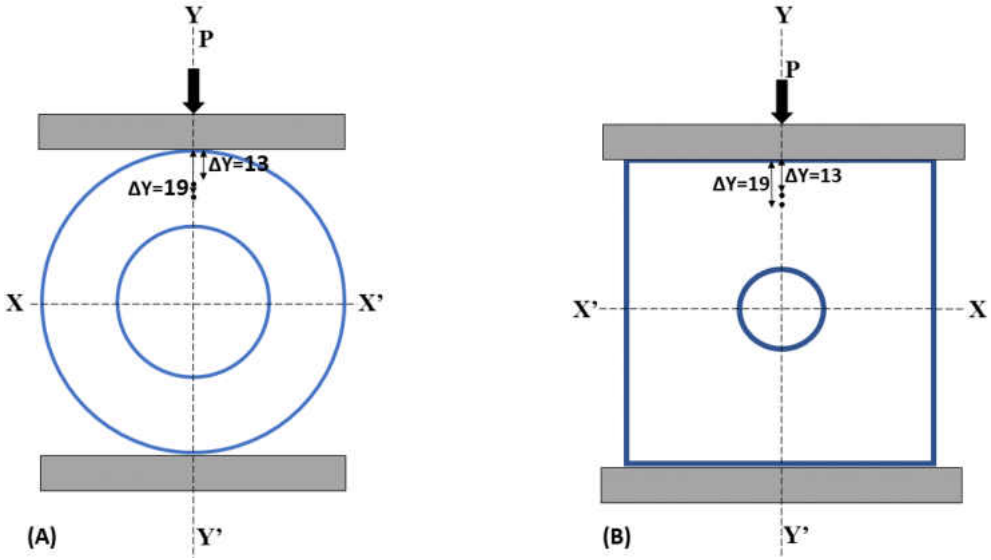

Figure 4.20 Strain Measurement Points on Different Specimens along Y-axis.

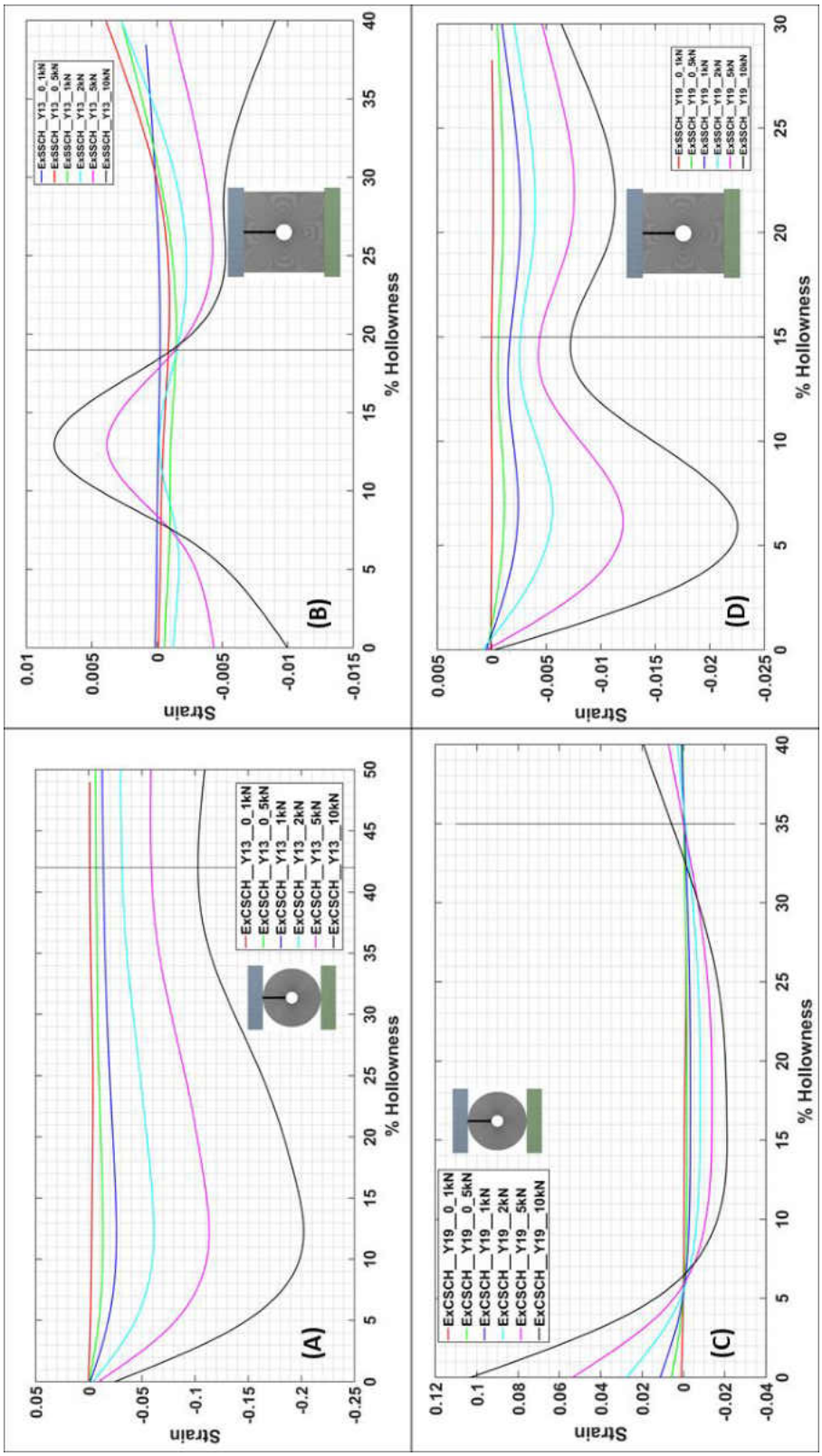

Figure 4.21 Strain Variation along Y-axis. (A) EX_CS_CH_ΔY=13 (B) EX_SS_CH_ΔY=13 (C) EX_CS_CH_ΔY=19 (D) EX_SS_CH_ΔX=19.

ii. ***Strain variation along X-axis.*** Figure (4.22) shows strain measurement locations 13mm (ΔX=13) and 19mm (ΔX=19), distance from outer edge along the axis perpendicular to loading axis. Figure (4.23) shows the variation of strain along X-axis with hollowness for different types of specimens. The plots on left are for strain variation along X-axis for circular specimens with concentric circular holes under normal compressive loading. The strains rise sharply between 25% to 40% hollowness for this case of loading and type of holes. The plots on right are for strain variation along X-axis for square specimens with concentric circular holes under normal compressive loading. The strain values rise sharply between 15 to 20% hollowness for this case of loading and type of specimen. Beyond these hollowness percentages, the specimens experience signification strain, possibly indicating a higher chances of failure.

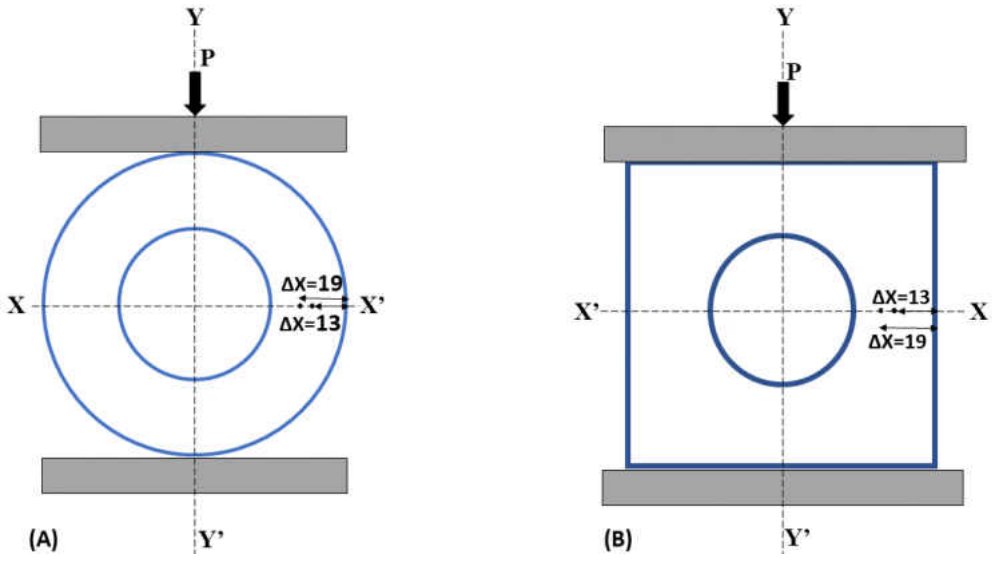

Figure 4.22 Strain Measurement Points on Different Specimens along X-axis.

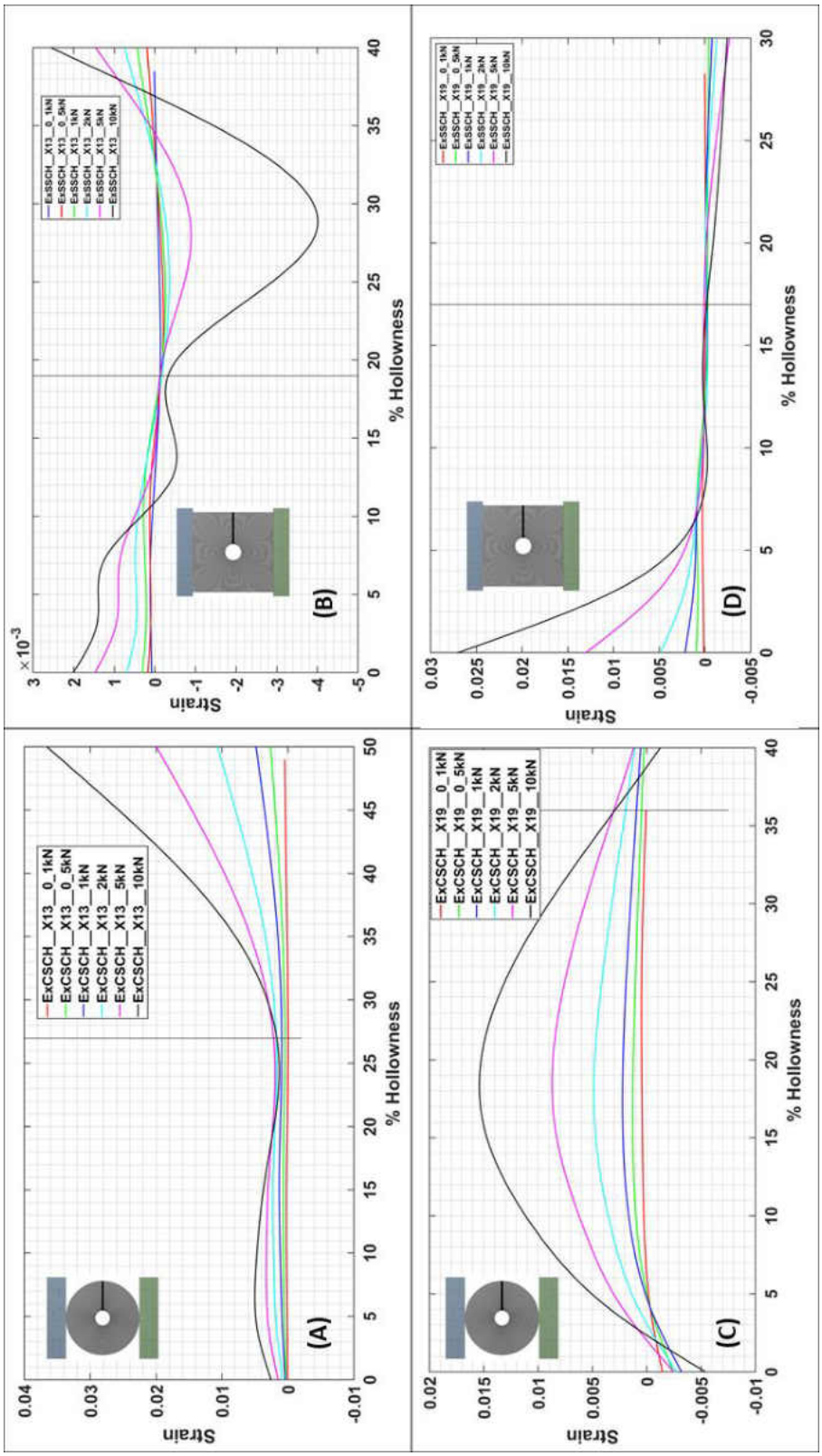

Figure 4.23 Strain Variation along X-axis. (A) CS_CH_ΔX=13 (B) SS_CH_ΔX=13 (C) CS_CH_ΔX=19 (D) SS_CH_ΔX=19.

4.2 Rolling Contact Fatigue Life

Based on the results from the experimental investigation of strain under normal compressive loading on the aluminum specimens, the hollowness approach is extended to fatigue life investigation of hollow specimens. FEA results show that hollow specimens have considerably lower contact stress than the solid ones. To check for the RCF life, the following experiment was attempted. However, due to multiple failure in the tester, the tests could not performed.

4.2.1 Specimen

Solid and hollow specimens were manufactured out of AISI 1045 carbon steel. The reason for choosing low carbon steel is the ease in manufacturability, lower endurance limit and the availability of comparable fatigue life data (S-N diagram). Fatigue behavior of AISI1045 carbon steel has been presented in Figure (4.24) [63].

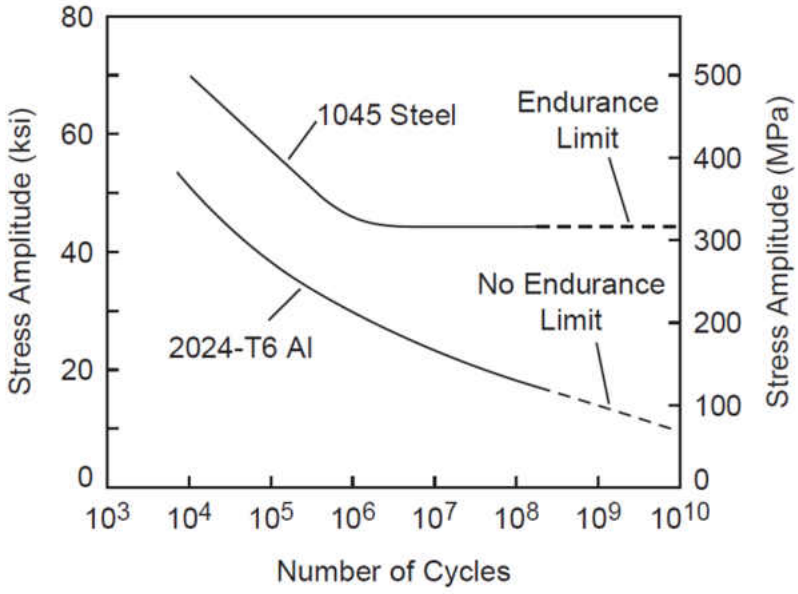

Figure 4.24 Fatigue Behavior of AISI 1045 Steel and 2024-T6 Al.

The specimens were manufactured in-house from 1.5inch round purchased. The specimens as listed in Table (4.3) have different hollowness and were designed and manufactured to be tested in the 2nd Generation Variable Slip Ratio Rolling Contact Fatigue Tester at UND. Additional slots were milled on the ends using a milling head for better grip of the specimen during tests. The specimens were then case hardened and finished, as shown in Figure (4.25), for the following specifications.

Effective Case Hardness: 50HRC

ECD off from outside Diameter: 0.038”

Surface Carbon: 0.8% to 0.9%

Hardness: 58.4 to 59.9 HRC

Surface roughness (R_a): 0.4 to 0.5µm.

Manufacturing drawings for all the test specimens have been added in Appendix D.

Table 4.3 Specimen Details for RCF test.

S.N	Specimens	Outside Diameter (inches)	Inside Diameter (inches)	Percentage Hollowness
1	Part No.1	1.5	0	0
2	Part No.2	1.5	0.6	16
3	Part No.3	1.5	0.75	25
4	Part No.4	1.5	0.9	36
5	Part No.5	1.5	1.05	49

Figure 4.25 Finished Specimens with Rollers.

4.2.2 Test Setup

The experiment was carried out on 2nd Generation Variable Slip Ratio Rolling Contact Fatigue Tester (VSR-RCF) [62]. The tester has been proven to provide accurate measurement of fatigue failure life on rolling contact elements. A 3-D view of RCF tester is shown in Figure (4.26). It comprises of three major components,

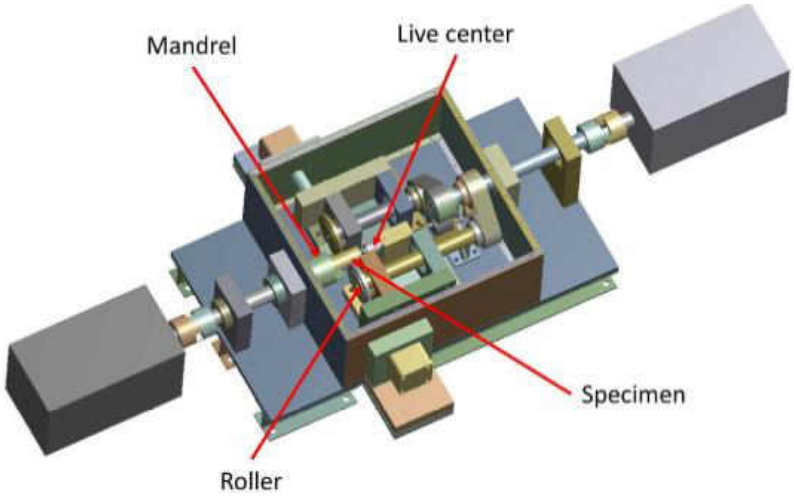

Figure 4.26 3D Cad Model of the RCF tester.

A. Mechanical System. It consists of the loading mechanism on the tester. Rollers are pushed onto the specimen by hydraulic cylinders to create a rolling contact. Figure (4.27) shows the arrangement of roller and specimens in the tester. Two rollers provide halve the testing time as for one rotation of roller, there occurs two loading cycles.

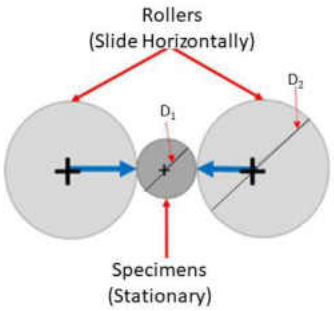

Figure 4.27 Roller and specimen configuration for the RCF tester.

Rollers and specimens are driven by high power motors driven at different speeds. Both rollers are connected to 10HP motor using a gear drive whereas specimen is

held on a chuck rotated by a different 10HP motor. Because of the difference in sizes of the rollers and specimens, the motor rpms are adjusted to obtain same surface velocity at the points of contact. Two hydraulic cylinders, and a hydraulic pump are used to load the rollers. The mechanism can apply a maximum load of 104kN with 21MPa line pressure. The pressure in these cylinders can be regulated using a pressure regulator mounted on the system. The rolling surfaces are continuously lubricated using the lubrication system to ensure proper regime of lubrication during the rolling.

B. Control System. When the specimens and rollers roll against each other, there can be slip between them. As relative sliding motion at the contact surfaces is a crucial factor in RCF life measurement, the control of motor speeds is critical to ensure proper operation of the tester. The rpm of motors is set so that the surface speeds of specimens and rollers match. To ensure no slip condition, feedback controls are used. The setup is designed to have a continuously variable slip ratio between roller and specimen using an Electronic Gear Ratio (EGR) technique [63]. The setup is equipped with Encoder feedback and Speed observer feedforward EGRs for the Powerflex motor controllers. For this experiment, no slip is desired and for the ease of operation, both the feedback encoders were disconnected. Instead, stroboscope was used to check the rotational speeds of specimen motor and roller motor. Both the motor drives output a voltage proportional to the speed of motor [64]. The voltage input for roller motor was used to obtain the input voltage for specimen motor to match the surface velocity of specimen and roller and ensure zero slip condition between them. The maximum speed of motors is 4165 rpm and the

maximum voltage input for the controller is 10 volts so the conversion factor for motor rpm to voltage is 416.5, meaning, for a signal of 1 volt to the controller, the motors run at an rpm of 416.5. Figure (4.28) shows all three system of the tester.

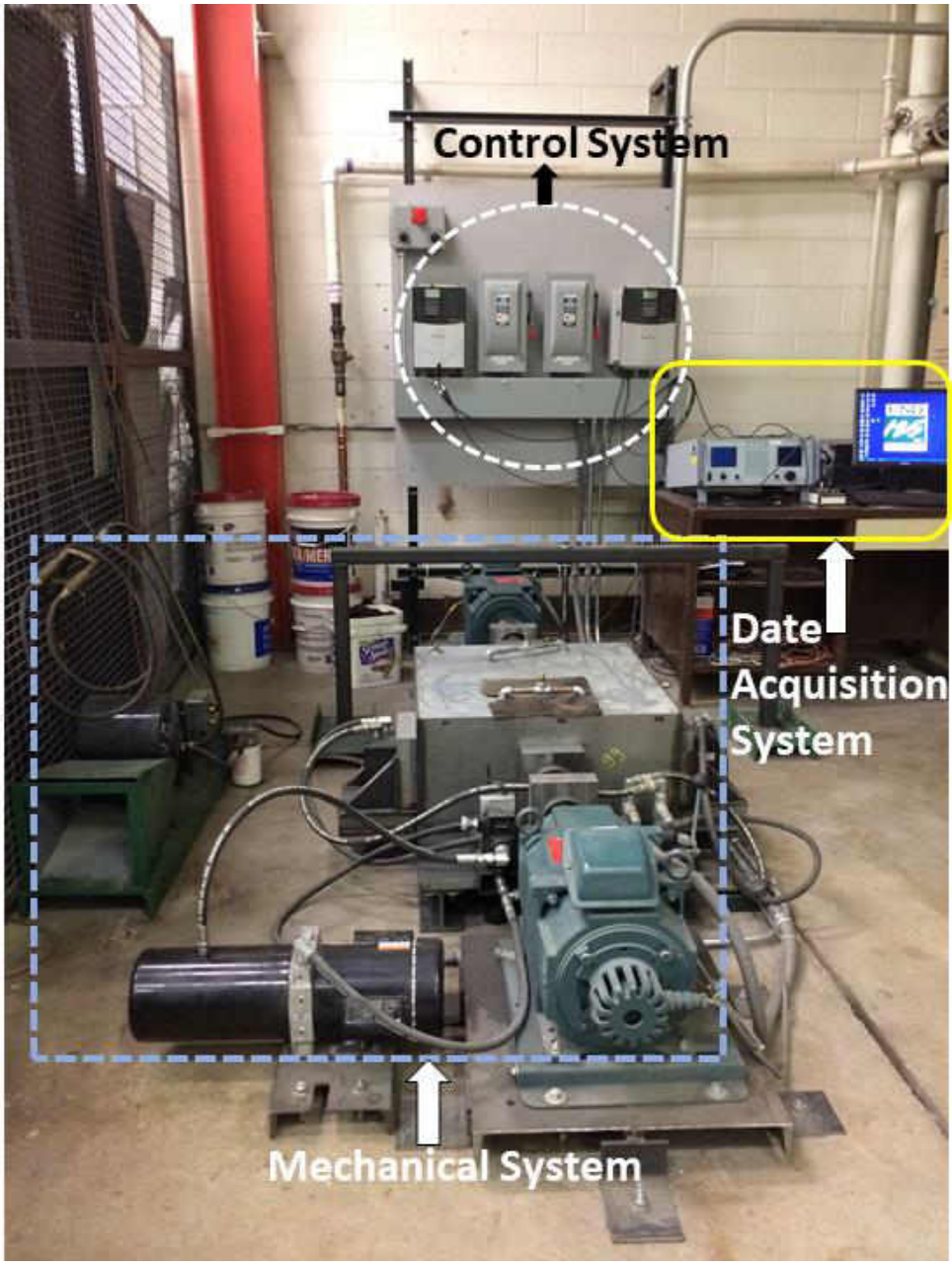

Figure 4.28 2nd Generation VSR-RCF Tester at UND.

C. Data acquisition and fault detection system. The setup is equipped with an Eddy current probe that is used to detect a crack on the specimen indicating a failure. Eddy current probes can detect very small cracks at a surface speed of 120m/s. The system is automated with data acquisition and signaling devices so that the motors stop once a crack is detected in the specimen. The eddy current probe is connected to Defectomat EZ 2.828® that reads multiple channels of voltages. Failure is indicated by when the measured probe output voltage exceeds a healthy specimen probe output voltage. On propagation of crack to the surface, the probe senses a change in the voltage. This change is voltage is compared to the threshold voltage set in the system. Once the change in voltage exceeds the threshold, crack on the specimen is detected. Real time data analysis is carried using MATLAB® program that then sends voltage signals to the motors to stop. Number of cycles and total run time for each experiment is recorded by the MATLAB® program thus giving the exact number of cycles of failure for each specimen. Figure (4.29) shows the failure detection process.

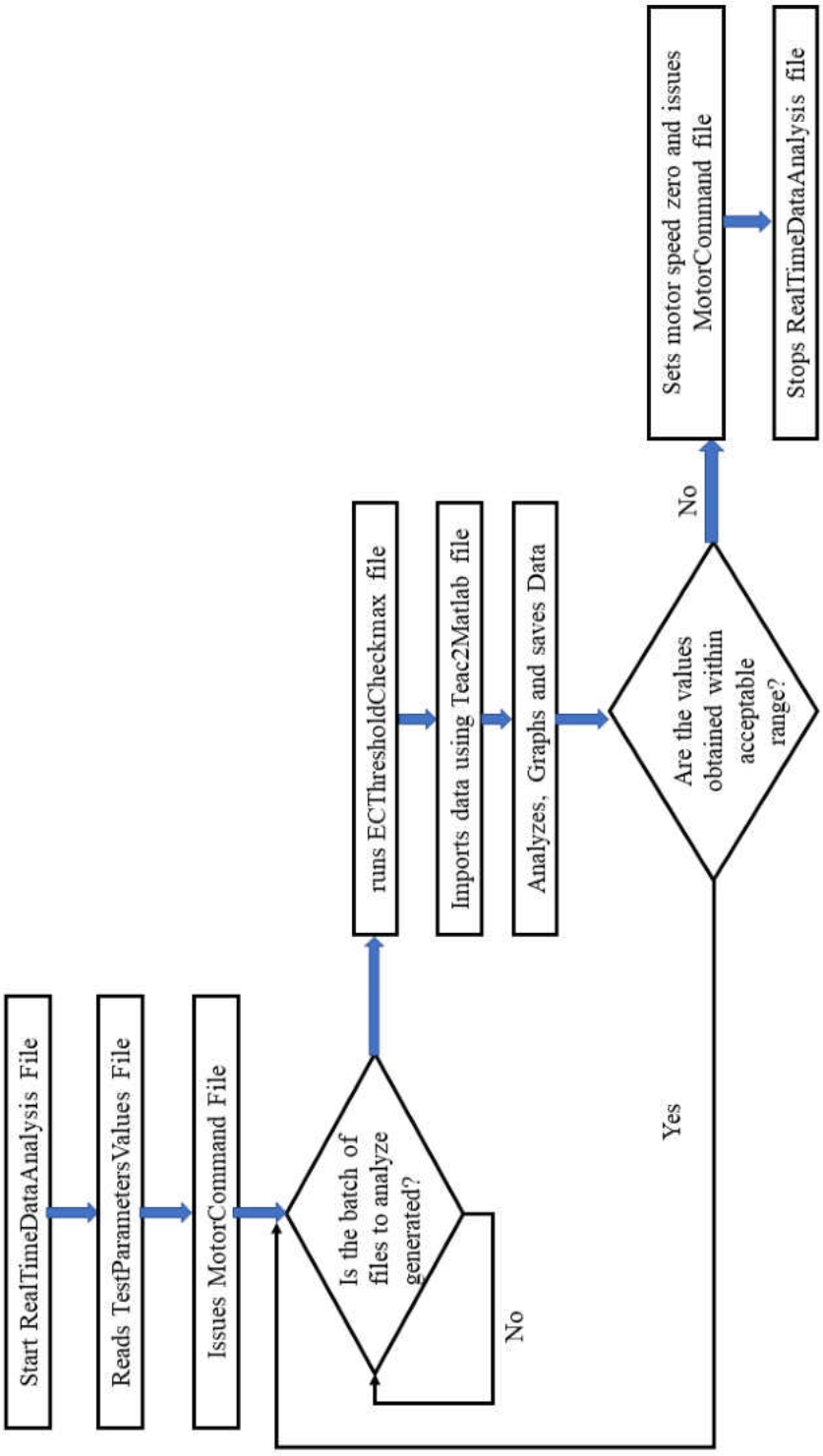

Figure 4.29 Flow Chart for Failure Detection System.

The following MATLAB® files have codes that send input to the motors, receive signals from the eddy current probe, process and analyze the data to generate plots and then send stop signal to the motors once failure is detected.

i. *Teac2Matlab.m* converts and saves data read by the TEAC LX-10.

ii. *TestParamatersValues.m* inputs values and testing parameters for all the files. It sets the specimen motor rpm, slipratio, channel conversion factors, initial values for different channel readings, maximum allowable change in the channel readings and the time interval for real time data analysis.

iii. *ECThresholdCheckmax.m* compares the data generated and plots graphs for different channel inputs continuously until failure is detected.

iv. *RealTimeDataAnalysis.m* loads the saved files from TEAC and then analyses them for the interval time set. It also sends a stop signal to the motors if failure is detected during analysis.

v. *motorcommand.m* sets the conversion between rpm and voltage to the controller and sends input data for the motor controllers.

4.2.3 Experimental Condition and Testing Procedure

The VSR-RCF tester had leakage issues. The machine was thoroughly cleaned and coated with sealing spray on the corner and edges. Once the sealing coat dried, the machine was filled with Transmission oil and the motors were run for an hour to test for leakage. After confirming the complete sealing at the corners, a test specimen was put in the chuck and

then centered using the live center on the other side. After all the components were tightened, the lid was put on and then eddy current probe was set over the specimen surface using feeler gauge. A trial run was performed to check the functioning of the overall machine including the control system, data acquisition and analysis system, hydraulic and mechanical components.

The specimens were heat treated before drilling holes for supporting the live center. Conical area drilled on the specimens weren't enough for holding the live center to center the specimen. This broke the tip of the live center. No replacement for the live center could be found as the manufacturer stopped the production of 1" taper shaft live center that could fit in the provided space. The roller motors were then provided with zero input, meaning the rollers could freely rotate against the rotating specimen.

An adjustment piece was designed and manufactured in-house at UND to fix the end of live center to the specimen as shown in Figure (4.30).

With proper alignment check and adequate cooling over the rolling surface, the specimens were again put to test run. Once the load was applied through the hydraulic cylinders, the frictional resistance due to rolling broke all the grip of the attachment piece over live center causing excessive heating of the specimen and high misalignment of the setup. Thus, no experiment could be completed for the anticipated results. The machine requires a complete redesign of components to ease cooling, alignment and better loading of the specimens.

Figure 4.30 Assembly of Live Center, Attachment and Specimen. (Left) 3D Cad Model (Right) Manufactured attachment in assembly.

4.2.4 Results

No results were obtained from the experiment as the machine could not be run as expected. Even after over 3 months of work, trying to run the machine, alignment and vibration of some components could not be fixed. This led to overheating of the specimens on loading and the specimens would not roll. The machine needs a careful redesign and manufacture of the components.

CHAPTER 5

RESULTS AND DISCUSSIONS

5.1 Overview

This chapter draws conclusions based on the theoretical, finite element and experimental results presented in the preceding chapters. It shows a comparison between the results obtained and validates the research hypothesis. The objectives of research was to examine the effect of hollowness in machine components and define the optimum hollowness of these components as well as Rolling contact components under fatigue loading. This chapter presents the results of the work performed in relation to the set objectives. Finally, it sets further course of action and provides recommendations for the successful testing of specimens.

5.2 Results

From the experiments and finite element simulations, it can be concluded that, hollow specimens have better distribution of stress under normal compressive loading compared to their solid counterparts. Stress distribution in hollow specimens does depend on the shape of the void. For regular concentric voids, stress is better distributed compared to

concentric irregular voids. The specimens with concentric regular voids in them have higher optimum percentage hollowness compared to concentric irregular ones. Hollow specimens under concentrated loadings have higher optimum percentage hollowness compared to hollow specimens under distributed loadings. Comparison between experimental and finite element strain at different locations along Y and X axis have been added in the Appendix E. The results indicate a good agreement between the experimental and finite element strain variation trend with hollowness. It should be noted that comparison between Finite element and Experimental results are merely qualitative. The plots have similar general shape and predict similar optimum hollowness. Quantitative comparison between the experimental and finite element results cannot be made, as there were some errors on the system discussed below. Table (5.1) shows the optimum hollowness percentages for different cases based on strain variation.

Table 5.1 Optimum Hollowness for Specimens under Different Loading Conditions.

Concentric Regular Voids	*Concentrated Loading*							
	Circular Specimens with Circular Holes							
	Y=13mm		Y=19mm		X=13mm		X=19mm	
	EXP.	FE	EXP.	FE	EXP.	FE	EXP.	FE
Optimum Hollowness (%)	42	38	35	27	27	36	36	26
Concentric Irregular Voids	*Distributed Loading*							
	Square Specimens with Circular Holes							
	Y=13mm		Y=19mm		X=13mm		X=19mm	
	EXP.	FE	EXP.	FE	EXP.	FE	EXP.	FE
Optimum Hollowness (%)	19	19	15	18	19	23	17	18

Hollow specimens are better at handling contact stress. Though no experimental result could be obtained, it can be implied from the available literature and the finite element analysis performed, that the peak contact stress is lower for hollow specimens. An optimum hollowness considering contact stress, equivalent stress and total deformation is around 40% by volume for concentric hollowness.

5.3 Sources of Error

The results for strain variation with hollowness from finite element analysis and experiment could not be matched with each other, rather only a qualitative conclusion has been drawn based on the pattern of variation of strain. The experimental strain measurement were made over small areas of the foil grid of strain gages rather than at particular points. Thus, they were the average values measured over an area, unlike the results from finite element analysis, which were measured at specific points. The strain gage modules (SCC-SG01) are built in Wheatstone bridges with quarter bridge configuration. These modules have in-built amplifiers that amplify the voltage readings from the Wheatstone bridge circuit. They are usually connected to a NI PCI-6251 DAQ board for data acquisition and the final readings for strains are directly obtained using LabView® software. The NI PCI-6251 card has a 16-bit resolution, which would not be precise enough to detect and measure the change in voltages observed during the experiments performed. Thus, voltage data from the SCC-SG01 modules were extracted and measured using the Digital Multi Meter of Agilent 34970A Data Acquisition Unit. The amplification factor hasn't been considered in the experimental data analysis as the focus is on the trend of strain variation rather than the exact numbers. This is one of the other sources of error. Since the strain values are obtained from measured voltage values from

the experimental setup. The plots obtained from the calculated strain values, do not necessarily represent the direction of deformation as the voltage readings recorded were zeroed out from the initial readings under no loads. The signs of the measured voltage values were based on the initial readings observed at zero loading.

Normal strain values have been obtained from the experiments. These values only represent strain along the length of the strain gages. Strain values obtained from finite element analysis incorporate the Poisson's effect in the strain measurement, thus strain measured from experiments do not necessarily match the ones obtained from FEA.

Use of 3-element Rosette strain gages could have addressed the effect of Poisson's ratio on strain, but this could limit the number of data points for measurement. A single rosette needs three channels for measurement of strain along three different axes which was not convenient with the available experimental setup. Multiple Wheatstone bridges circuits had to be constructed out of available resistor to use with rosette, which would add more sources of errors in the setup.

5.4 Conclusion

The author does not believe that hollow machine components are stronger than the solid ones but it can be concluded from this research that machine components can be made hollow to a certain extent for a tolerable deformation and stress values. If these components were to be 3D printed, this would definitely save cost, weight and manufacturing lead time.

5.5 Future Work

The intent of the future work is to make use of the results from this research for testing and evaluating the applicability of hollow 3D printed load bearing components. The same approach can be used for testing the hollow load bearing components. The final work would be to actually built 3D printed components and test them.

The RCF tester needs a redesign and manufacture of components. The author recommends the following for redesigning of the machine

1. The existing setup is too compact and has very little room for loading specimen. The space between the live center, chuck and loading plates is very limited, making it is very difficult to tighten the specimen and the other parts too. So, the machine has to be more spacious or have a better specimen fixing mechanism.

2. One of the issues while testing was the self-loosening of one of the rollers. Upon contact loading, the rollers would loosen creating vibration and misalignment of specimen. Even adding spring washers, using set screws to tighten the rollers didn't help. The tightening mechanism for roller needs redesign.

3. Lubricating oil circulation system needs an effective radiator to cool the fluid and maintain a lower temperature during operation of the machine.

4. Bearings on the shafts need replacement. These bearing should either be self-lubricating or there needs to be cooling mechanism in place to deal with the to deal with the heating of these bearings.

The specimens could then be tested for their RCF life to prove the results from FE analysis. Published literatures have used finite element method to find optimum hollowness for cylindrical bearings [23], [24]. If only, these results be validated using experiments, it would open up new vistas for the use of hollow rolling components like gears, bearings, cams, etc. With the advent of Additive Manufacturing (AM), these rolling elements can potentially be manufactured with inside measurable voids or hole, that have longer RCF failure life and are lightweight.

APPENDICES

Appendix A: 2D Fe Models for Strain Investigation

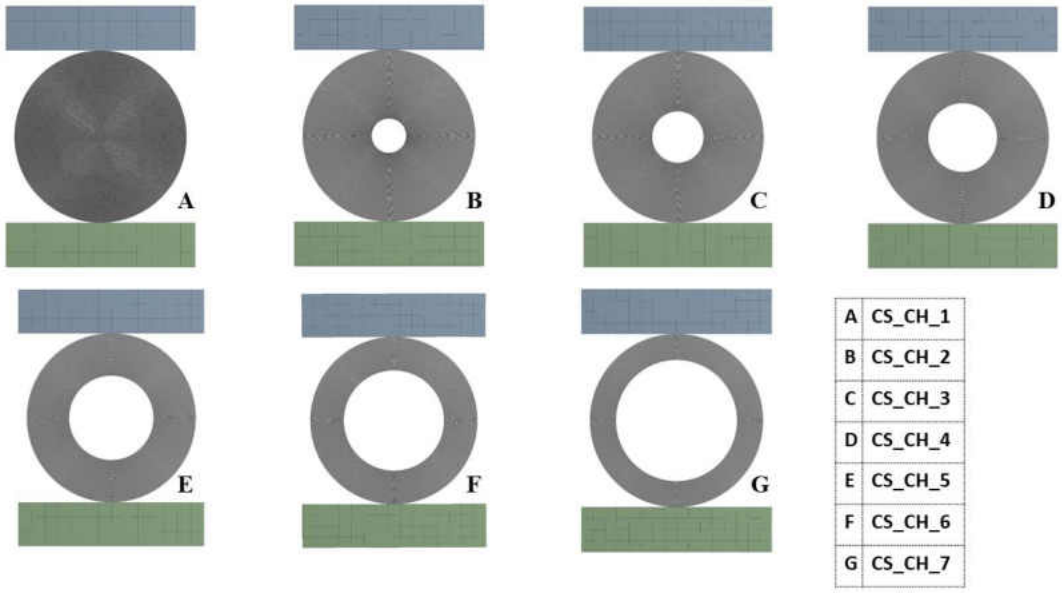

Figure 5.1 2D FE Models for Circular Specimens with Circular Holes.

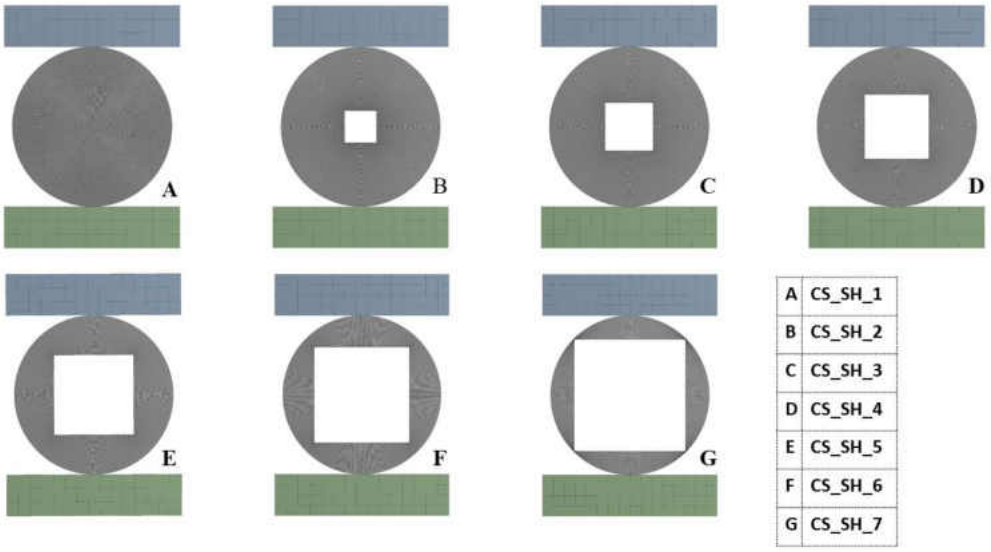

Figure 5.2 2D FE Models for Circular Specimens with Circular Holes.

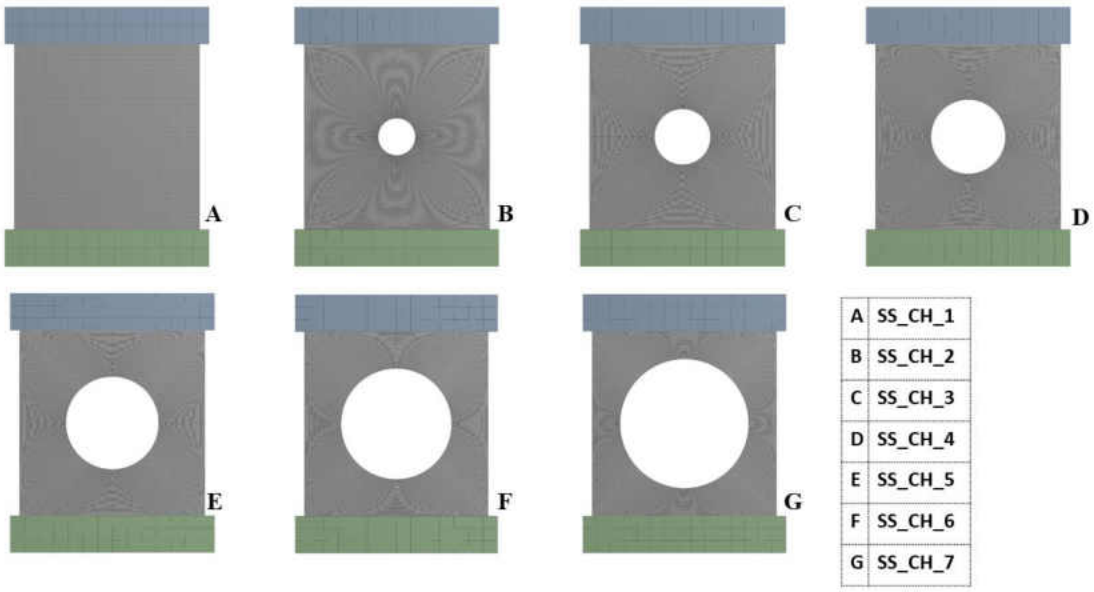

Figure 5.3 2D FE Models for Square Specimens with Circular Holes.

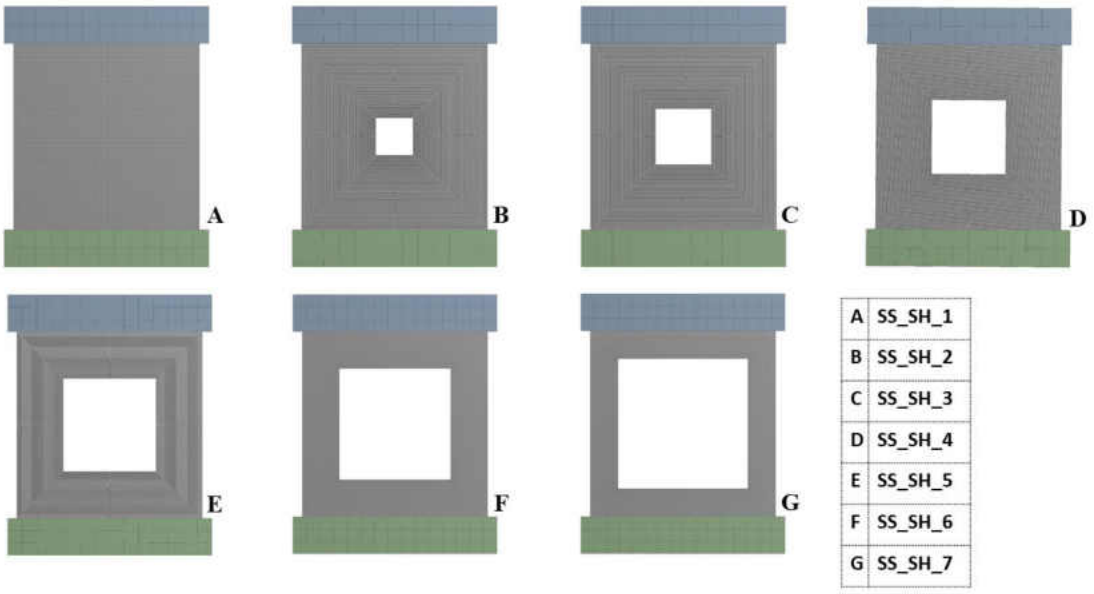

Figure 5.4 2D FE Models for Square Specimens with Square Holes.

Appendix B: Mesh Metrics

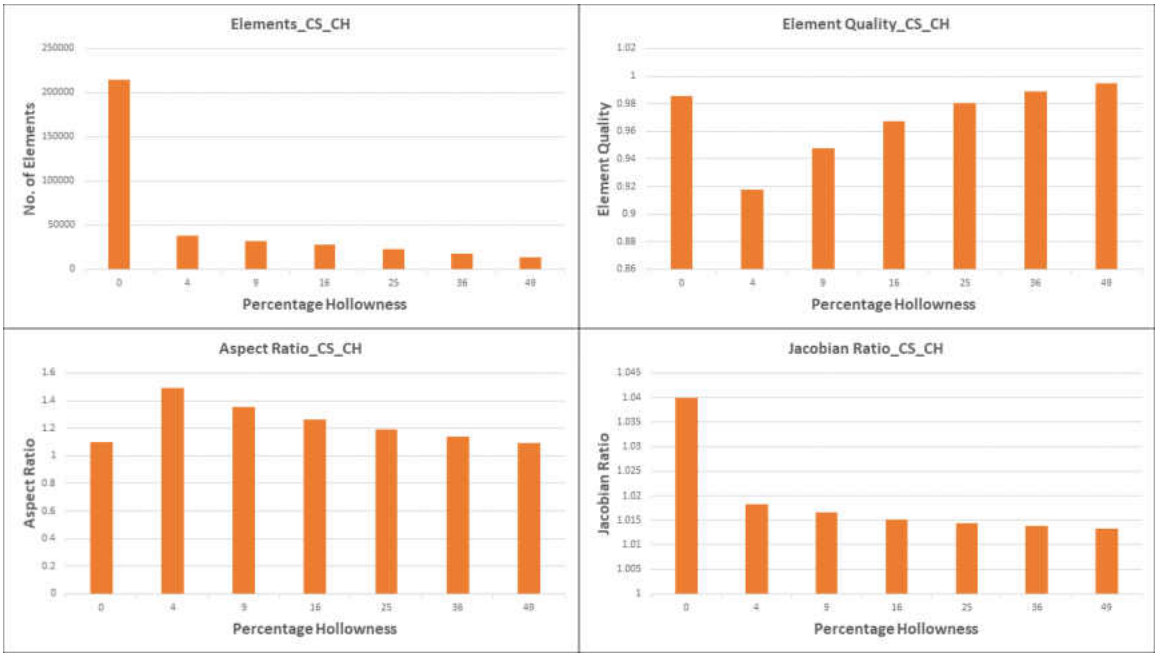

Figure 5.5 Mesh Metrics (1) for Circular Specimens with Circular Holes.

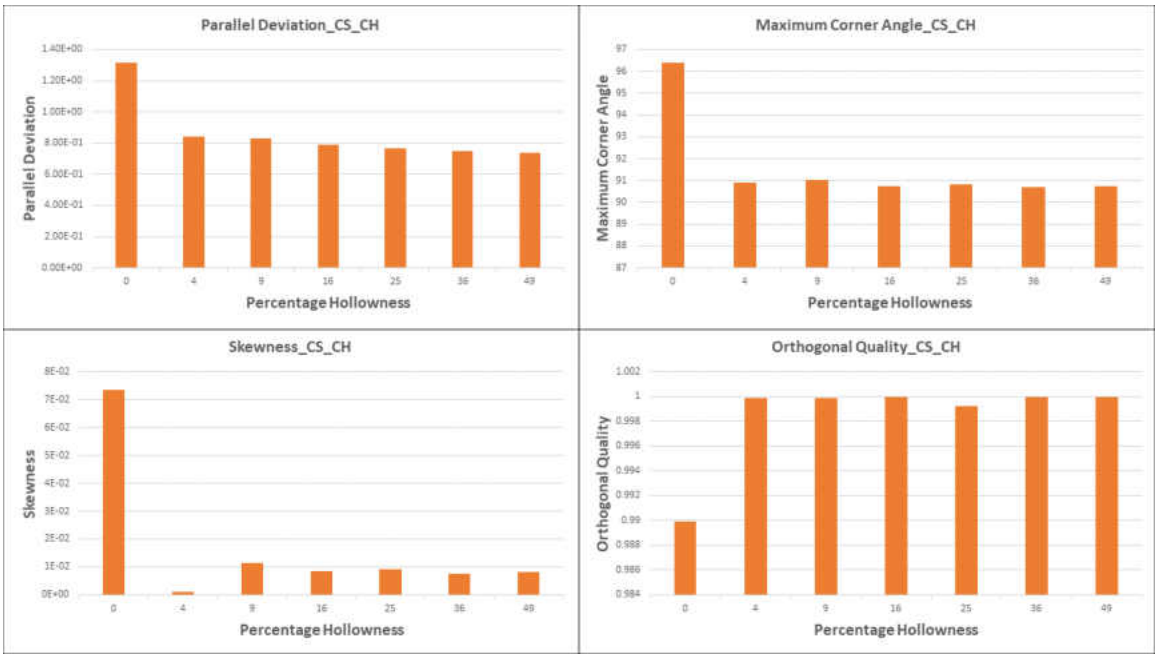

Figure 5.6 Mesh Metrics (2) for Circular Specimens with Circular Holes.

Appendix C: Finite Element Convergence Plots

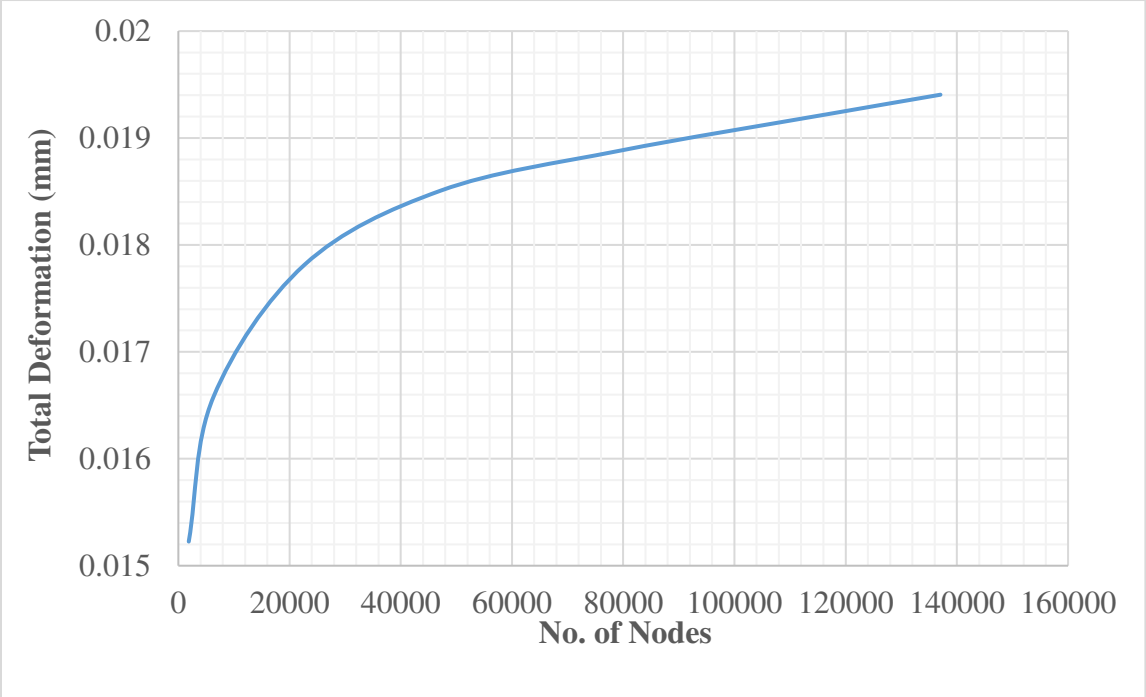

Figure 5.7 Finite Element Convergence Plot for Solid Specimen with 0% Hollowness.

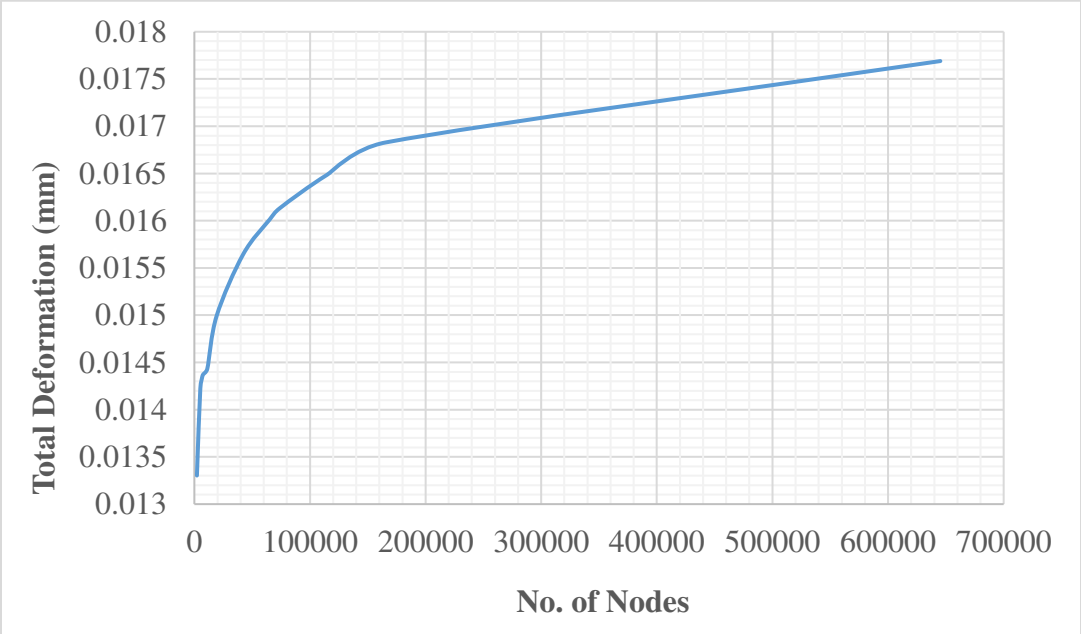

Figure 5.8 Finite Element Convergence Plot for 1% Hollow Specimen.

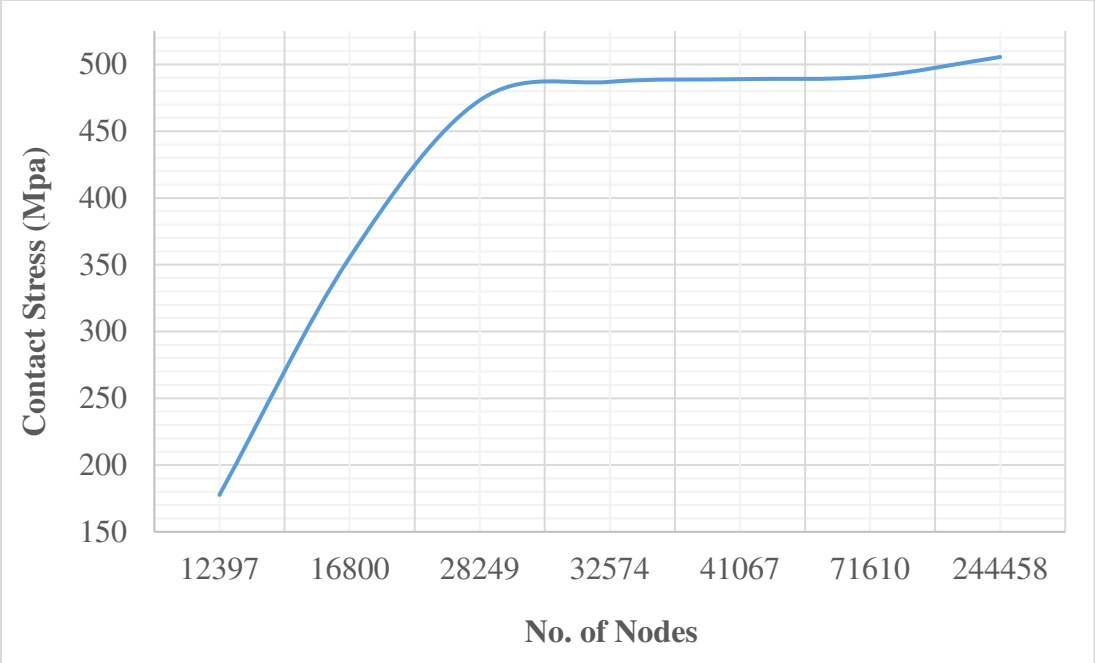

Figure 5.9 FE Convergence Plot for 0% Hollow Specimen in RCF Test.

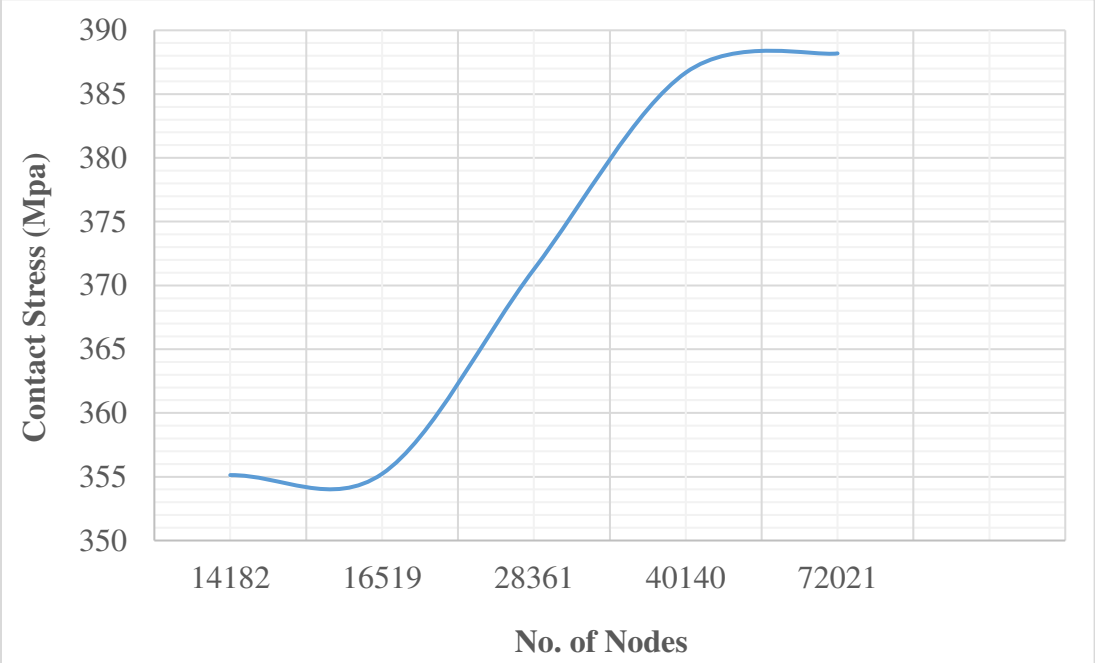

Figure 5.10 FE Convergence Plot for 1% Hollow Specimen in RCF Test.

Appendix D: Manufacturing Drawings for RCF Test

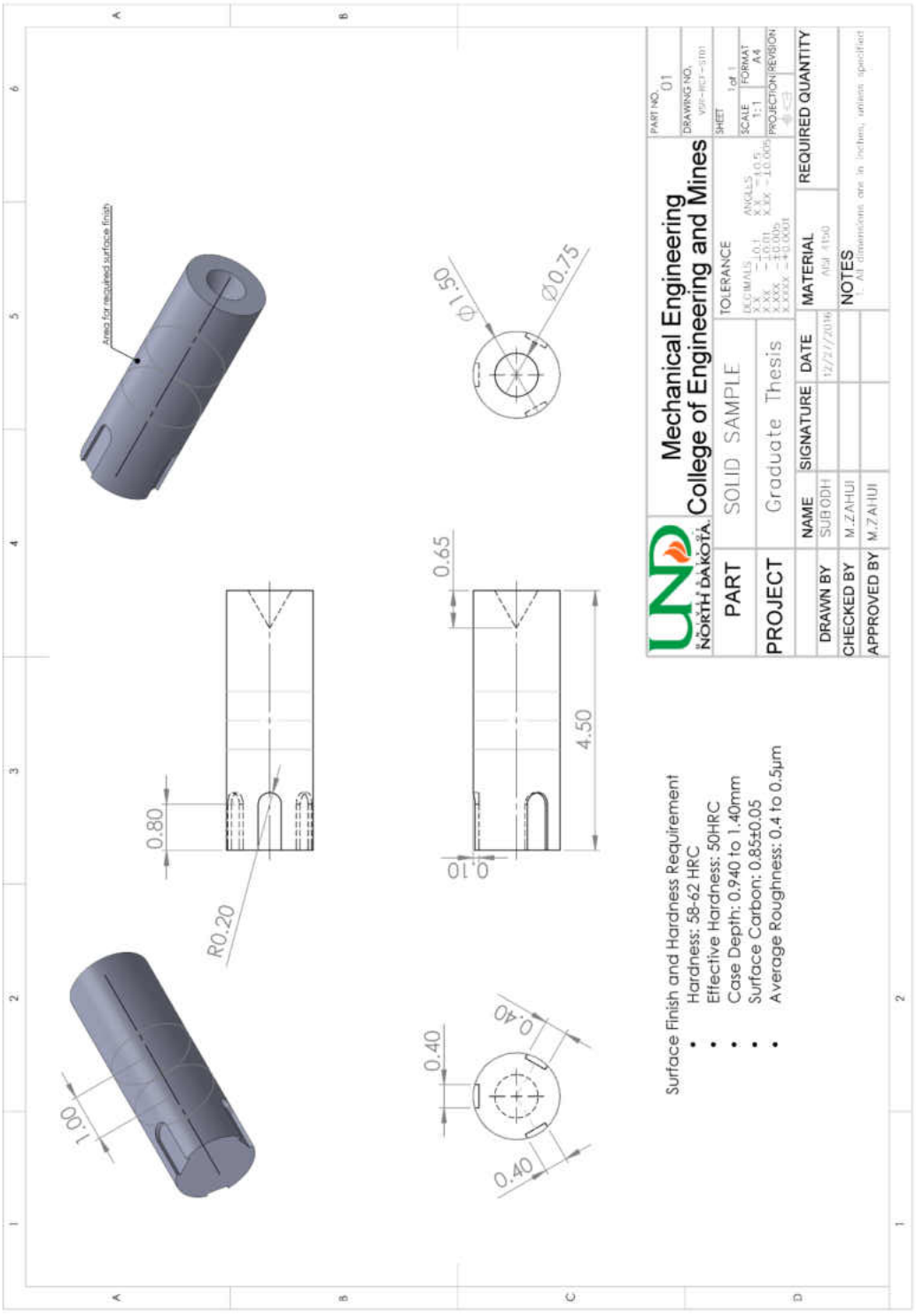

Figure 5.11 Manufacturing Drawing for RCF Testing of Solid Specimen.

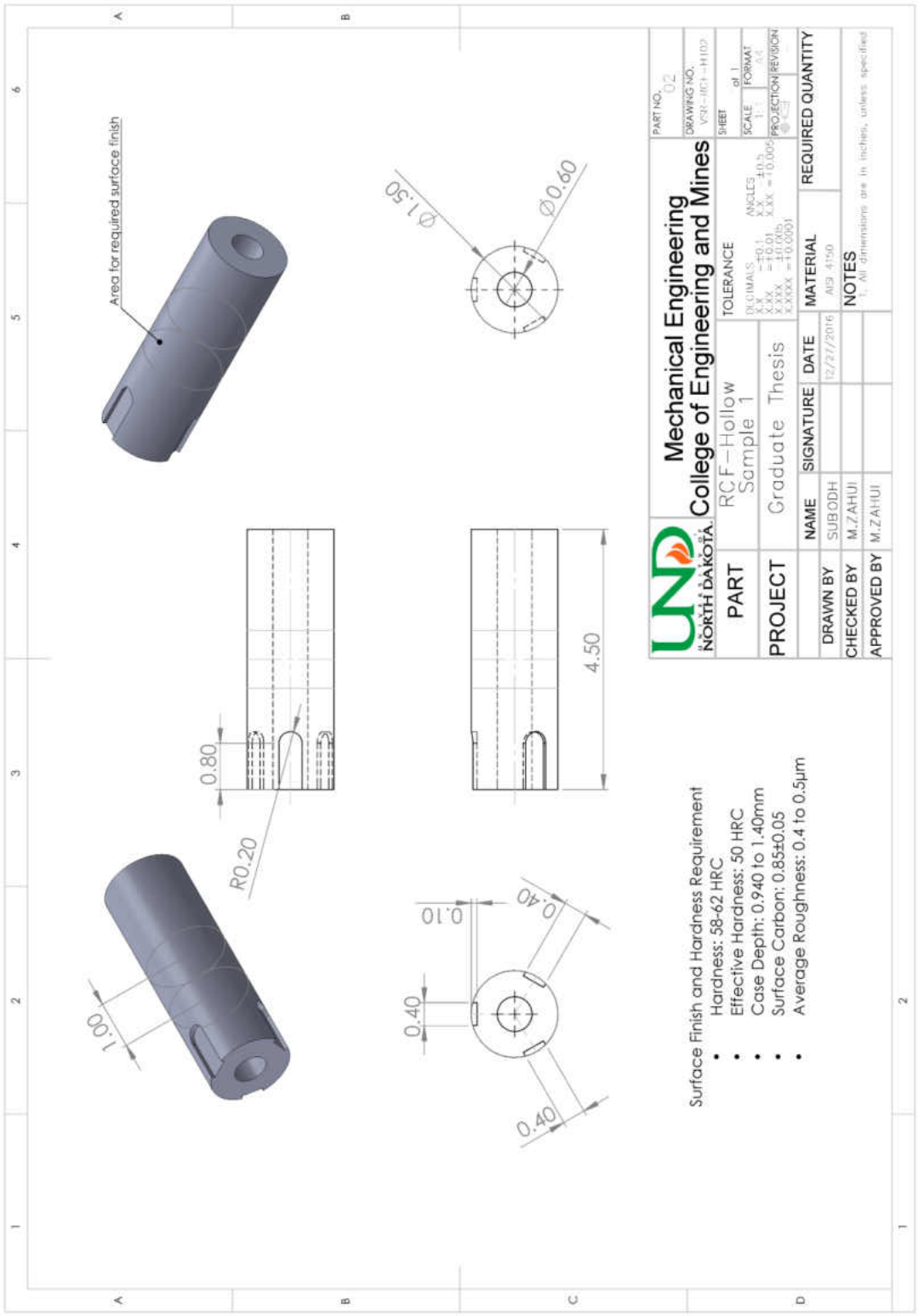

Figure 5.12 Manufacturing Drawing for RCF Testing of 40% Hollow Specimen.

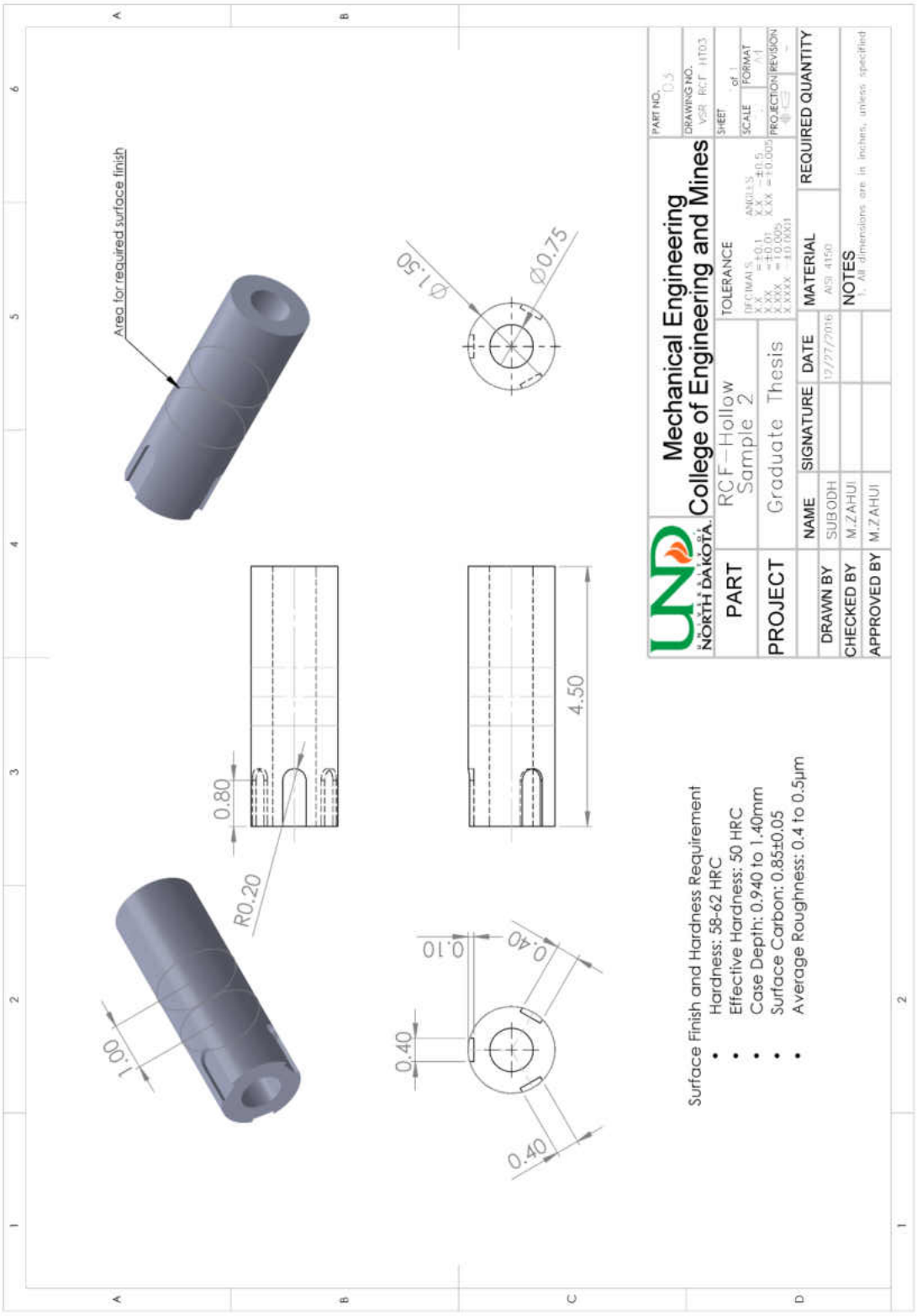

Figure 5.13 Manufacturing Drawing for RCF Testing of 50% Hollow Specimen.

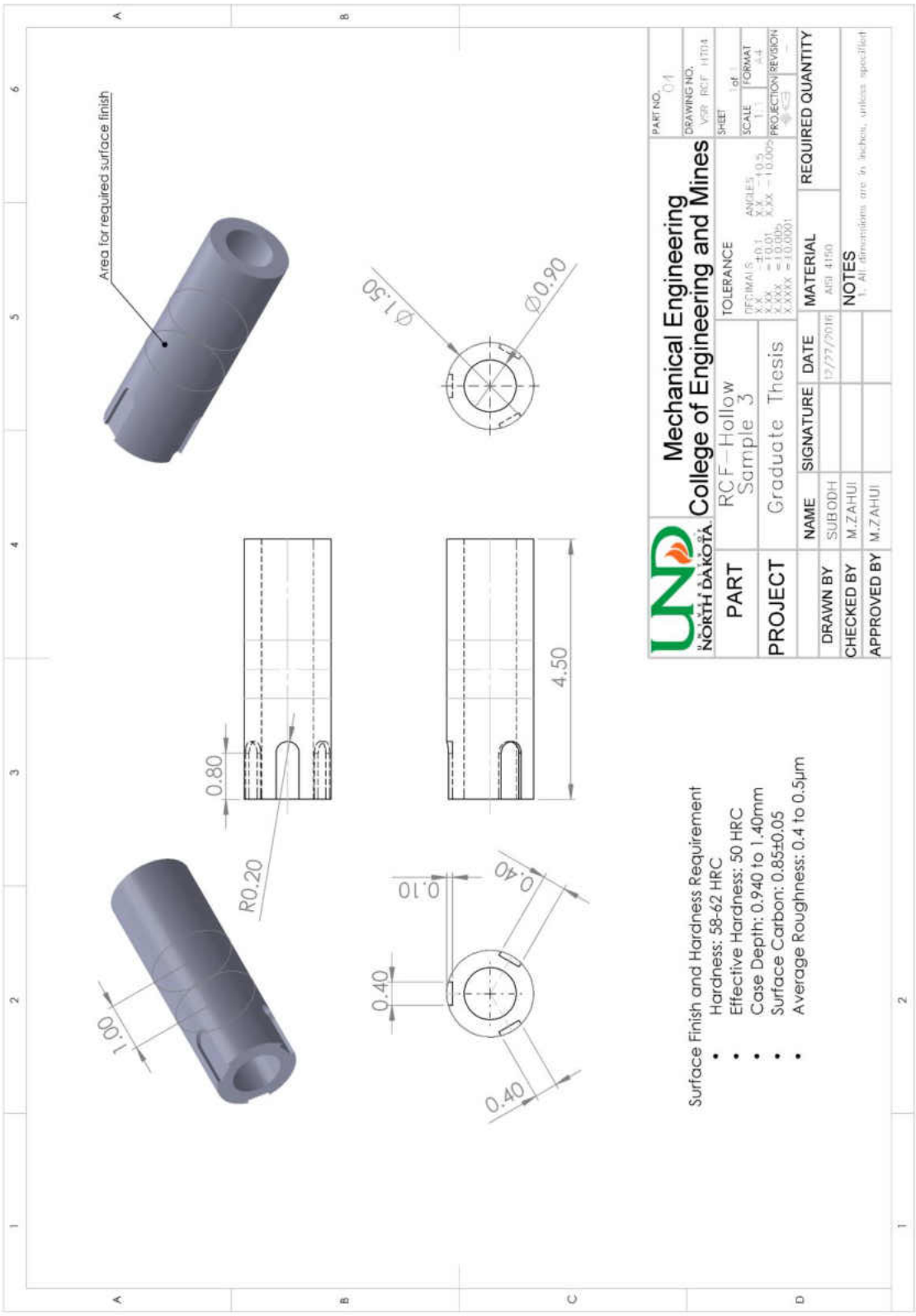

Figure 5.14 Manufacturing Drawing for RCF Testing of 60% Hollow Specimen.

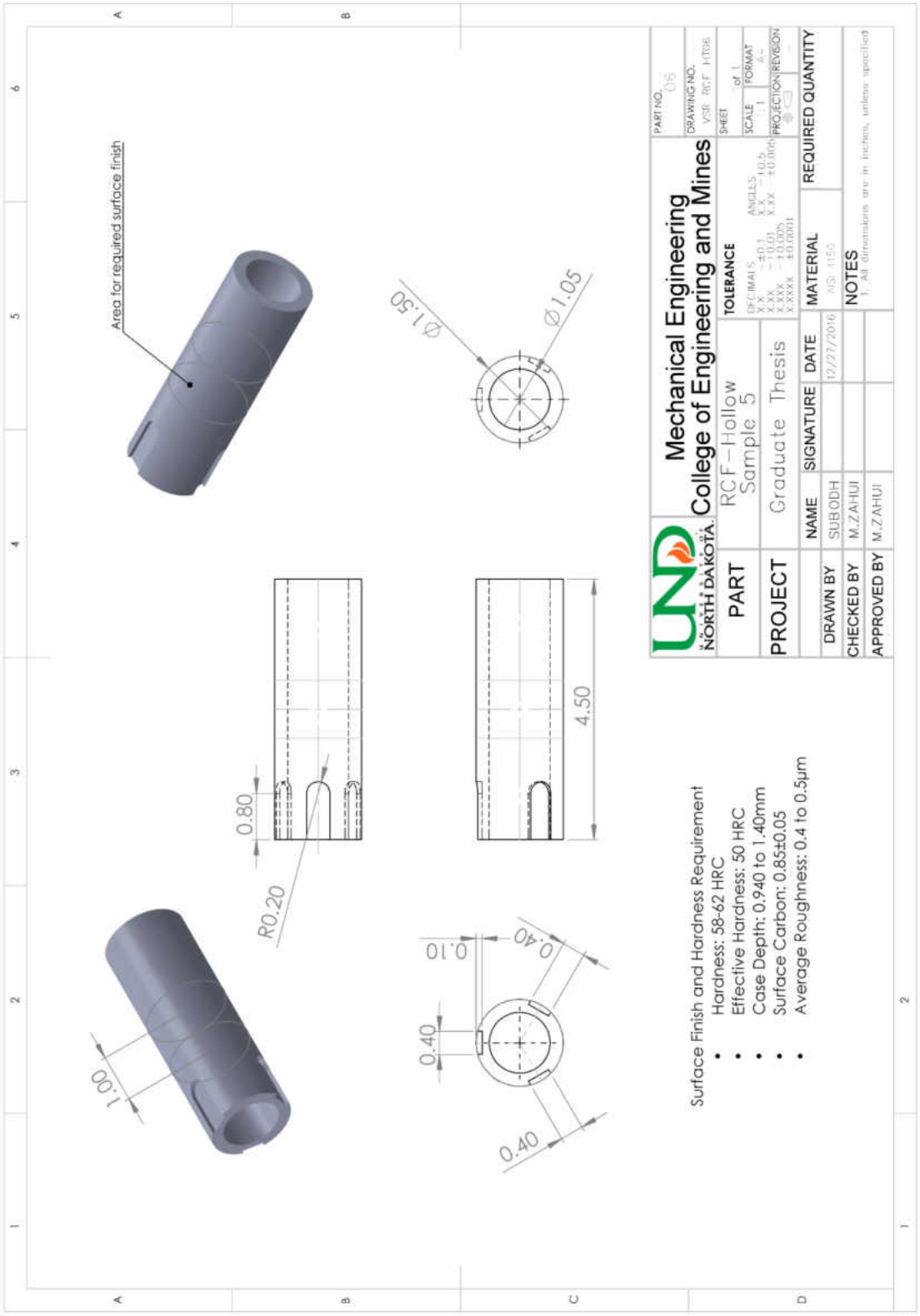

Figure 5.15 Manufacturing Drawing for RCF Testing of 70% Hollow Specimen.

Appendix E: Finite Element vs. Experimental Results

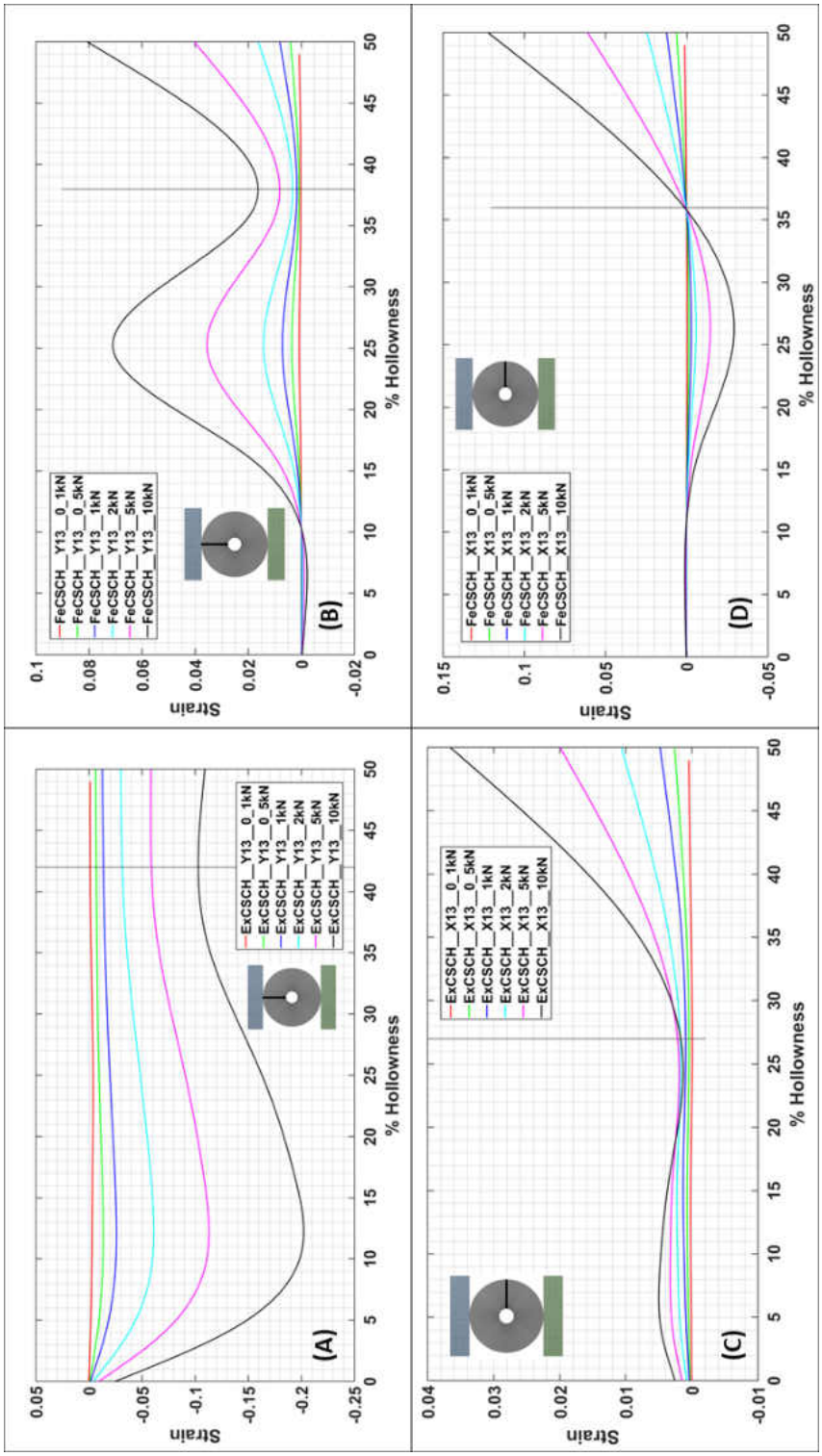

Figure 5.16 Strain Variation at 13mm from the Edge for Circular Specimen. (A)EX_CS_CH_ΔY=13 (B) FE_CS_CH_ΔY=13 (C) EX_CS_CH_ΔX=13 (D) FE_CS_CH_ΔX=13.

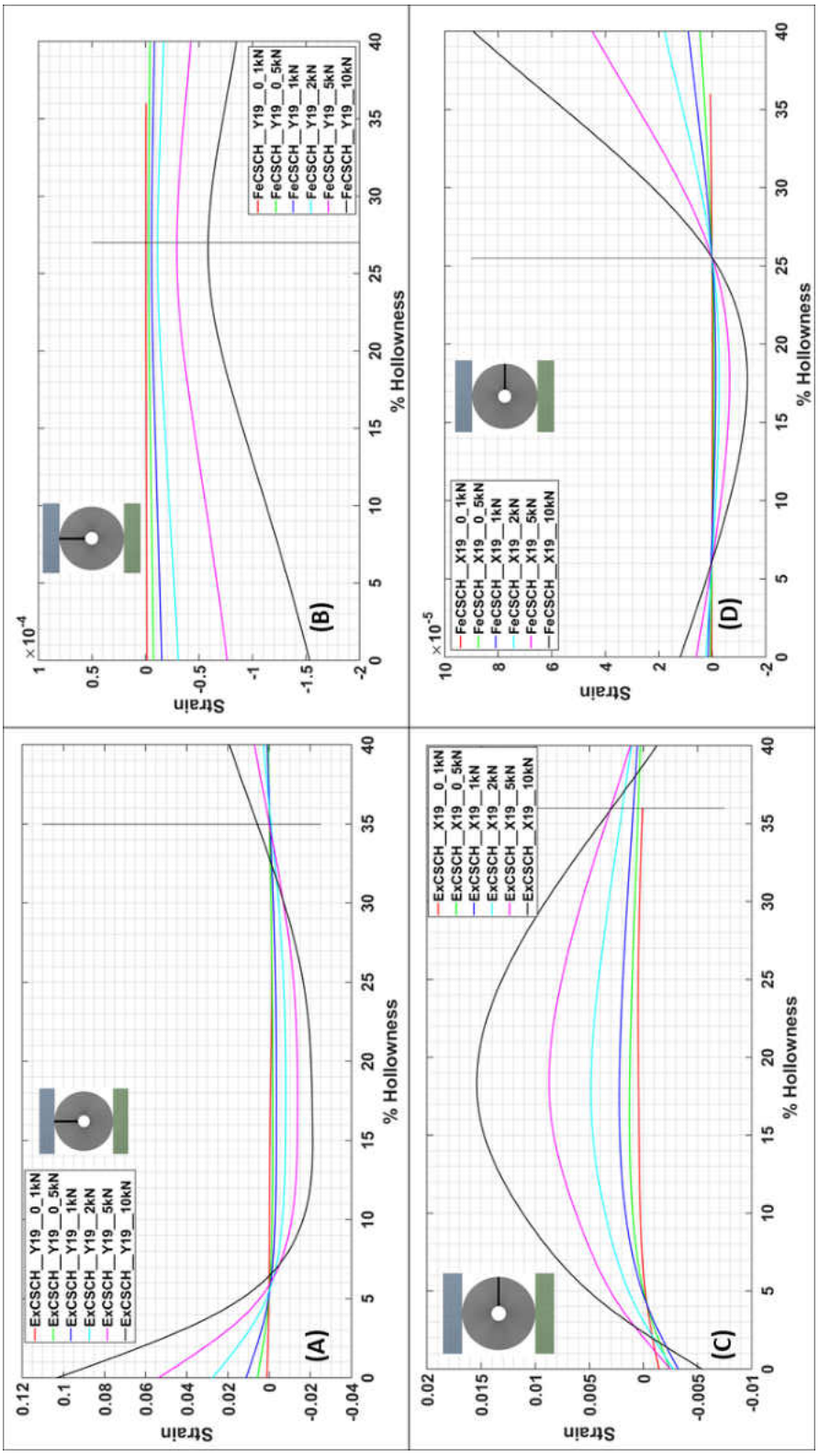

Figure 5.17 Strain Variation at 19mm for Circular Specimen. (A)EX_CS_CH_ΔY=19mm (B) FE_CS_CH_ΔY=19mm (C) EX_CS_CH_ΔX=19mm (D) FE_CS_CH_ΔX=19mm

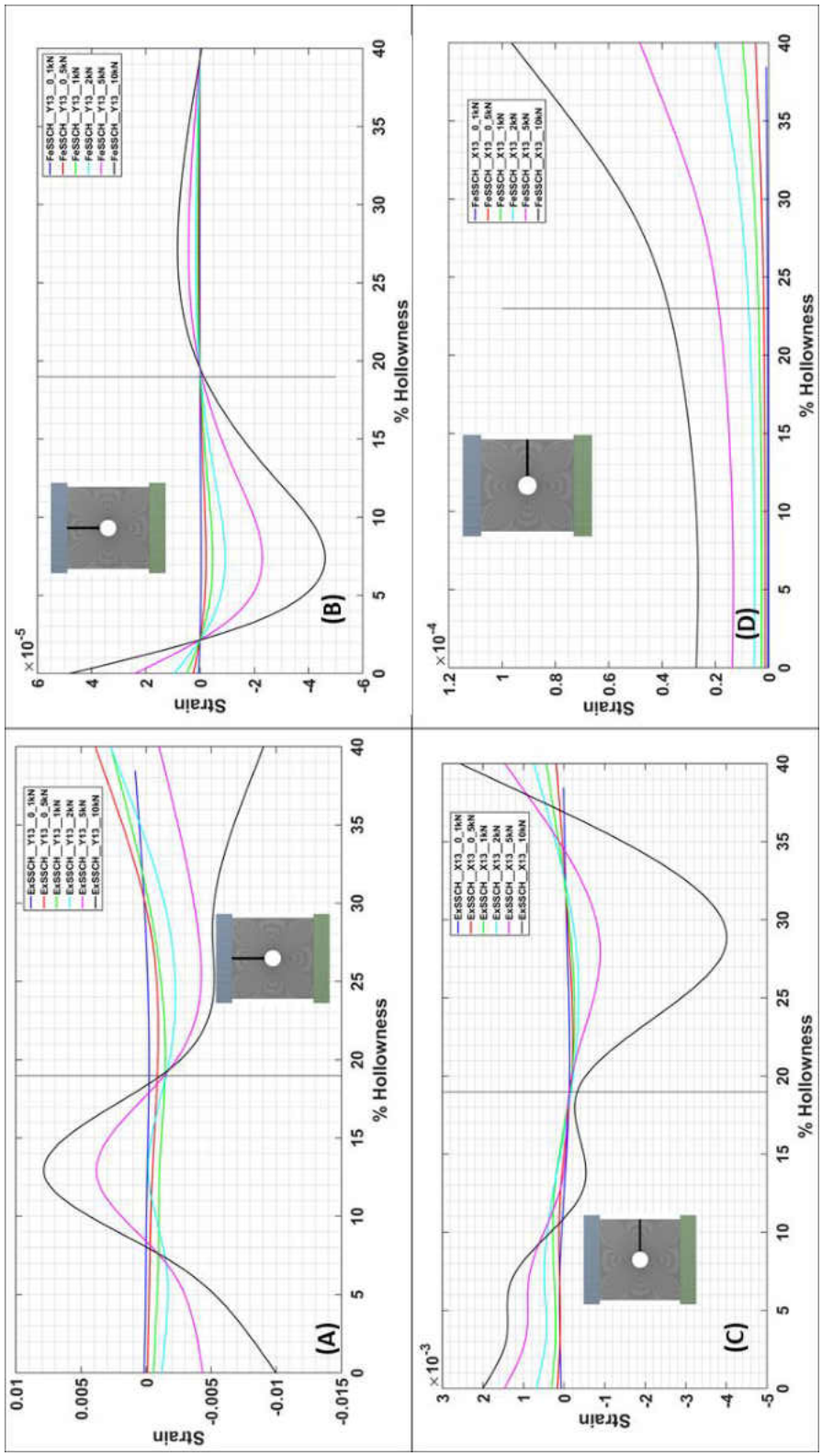

Figure 5.18 Strain Variation at 13mm for Square Specimen. (A)EX_SS_CH_ΔY=13mm (B) FE_SS_CH_ΔY=13mm (C) EX_SS_CH_ΔX=13mm (D) FE_SS_CH_ΔX=13mm

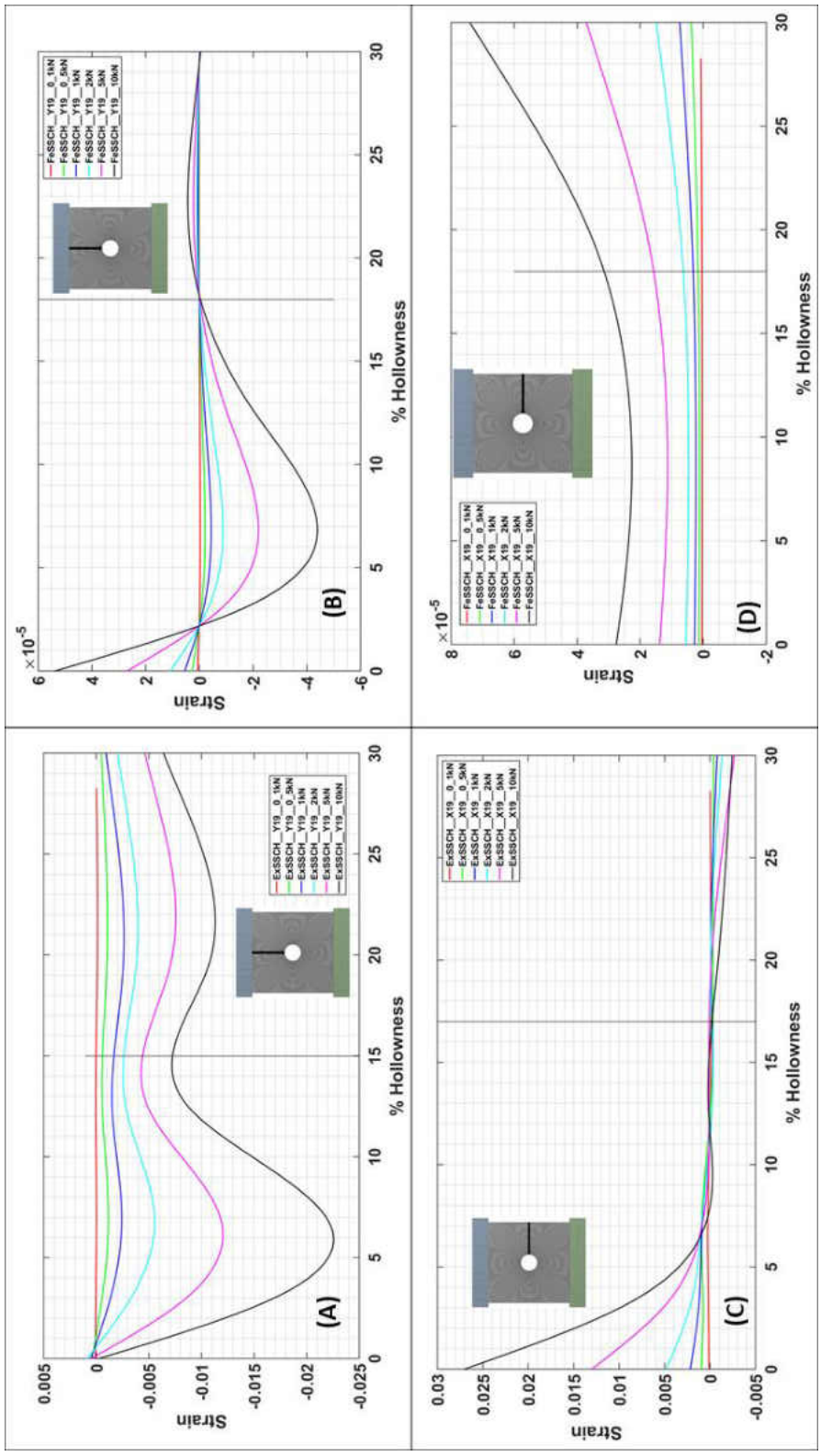

Figure 5.19 Strain Variation at 19mm for Square Specimen. (A)EX_SS_CH_ΔY=19mm (B) FE_SS_CH_ΔY=19mm (C) EX_SS_CH_ΔX=19mm (D) FE_SS_CH_ΔX=19mm

REFERENCES

[1] Thompson M.K. et al, (2016). "Design for Additive Manufacturing: trends, Opportunities, Considerations, and Constraints". CIRP Annals-Manufacturing Technology 65-737-760.

[2] Boothroyd G., (2005). "Assembly Automation and Product Design", 2nd ed. Taylor and Francis, New York.

[3] Poli C., (2001) "Design for Manufacturing: A Structured Approach", Elsevier.

[4] Kuo T C., Huang S, Zhang H C (2001) "Design for Manufacture and Design for 'X': Concepts, Applications and Perspectives", Comput. Ind. Eng. 41(2): 241-260.

[5] Anderson DM., (2014). "Design for Manufacturability: How to Use Concurrent Engineering to Rapidly Develop Low-Cost, High-Quality Products for Lean Production", CRC Press.

[6] Molly E., Yang H., Browne J., (1991) "Design for Assembly within Concurrent Engineering", CIRP Ann. Manuf. Technol. 40(1).

[7] Sohlenius G., (1992). "Concurrent Engineering", CIRP Ann. Manuf. Technol. 41(2).

[8] ASTM Standard, Standard Terminology for Additive Manufacturing Technologies, vol. 10.04.

[9] Diegel O., Singammeni S., Reay S., Withell A., (2010), "Tools for Sustainable Product Design: Additive Manufacturing, Journal of Sustainable Development", vol.3No. 3: September 2010.

[10] Esmaeilian B., Behdad S., Wang B., 2016, "The evolution and future of manufacturing: A review", Journal of Manufacturing Systems 39(2016)79-100.

[11] ISRM (1978), "Suggested Methods for Determining Tensile Strength of Rock Materials", Int J Rock Mech Min Sci Geomech Abstr 15(3):99–103. doi:10.1016/0148-9062(78)90003-7.

[12] ASTM (2008) D 3967-08, "Standard Test Method for Splitting Tensile Strength of Intact Rock Core Specimens", ASTM International, West Conshohocken, USA.

[13] Hobbs D.W., (1965), "An Assessment of a Technique for Determining the Tensile Strength of Rock", Brit. J. Appl. Phys. 1965, Vol.16.

[14] Yanagidani T., Sano O., Terada M., and Ito I., (1978), "The observation of cracks propagating in diametrically-compressed rock discs", Intl J Rock Mech Min Sci Geomech Abstr, 15(5), 225-235.

[15] Chen S, Yue ZQ, Tham LG, "Digital Image-based Numerical Modeling Method for Prediction of Inhomogeneous Rock Failure", Int J Rock Mech Min Sci 41(6):939-957.

[16] Fairhurst C. (1964), "On the Validity of the 'Brazilian' Test for Brittle Materials", Int J Rock Mech Min Sci Geomech Abstr 1(4): 535-546. doi: 10.1520/GTJ103134.

[17] Hooper JA. (1971), "The Failure of Flass Cylinders in Diametral Compression", J Mech Phys Solids 19(4):179-200.

[18] Hudson JA. (1969), "Tensile strength and Ring Test", Int J Rock Mech Min Sci Geomech Abstr 6(1):91-97. doi:10.1016/0148-9062(69)90029-1.

[19] Swab JJ., Yu J., Gamble R., Kilczewsi S., (2011), "Analysis of the Diametral Compression Method for Determining the Tensile Strength of Transparent Magnesium Aluminate Spinel", Int J Fract. doi: 10.1007/s10704-011-9655-1.

[20] Filon L.N.G., (1924) "The Stresses in a Circular Ring, Selected Engineering Papers", The Institution of Civil Engineers, London.

[21] Timoshenko SP., Goodier JN., "Theory of Elasticity". 2nd ed. New York: McGraw Hill, 1951.

[22] Kourkoulis S.K., Markides Ch.F., (2014), "Stresses and Displacements in a Circular Ring Under Parabolic Diametral Compression", International journal of Rock Mechanics and Mining Sciences 71 (2014) 272-292.

[23] Darji P.H., Vadkharia D.P., (2008), "Determination of Optimum Hollowness for Hollow Cylindrical Rolling Element Bearing", Proceeding of IMECE 2008, October 31-Nov. 6, 2008 MA, USA.

[24] Abu Jadayil W., Flugard D., Qamhiyah A., "Fatigue Life Investigation of Solid and Hollow Rollers in Pure Rolling Contact", Proceedings of WTC2005, World Tribology Congress III, Sept.12-16, 2005, Washington D.C, USA.

[25] Raplh I. Stephens, Fatmi R.I., Stephens A.R., & Fuchs H.O., (2001), "Metal Fatigue in Engineering", 2nd Edition, New York, John Wiley & Sons Inc.

[26] "Standard Terminology Relating to Fatigue and Fracture Testing" ASTM Designation E1823, Vol 03.01, ASTM, West Conshohocken, PA, 2000, p.1034.

[27] Campbell F., (2008), “Elements of Metallurgy and Engineering Alloys”, ASM International, Chapter 14 Fatigue.

[28] Loewenthal S.H., (1984), “Factors that Affect the Fatigue Strength of Power Transmission Shafting and Their Impact on Design”, NASA Technical Memorandum 83608.

[29] Final Report: Rolling Contact Fatigue, “A Comprehensive Review (2011)”, US Department of Transportation, Federal Railroad Administration, Office of Railroad Policy and Development, Washington, DC 20590.

[30] Deskhmukh, S. (2014), “Development of 2nd Generation of Variable Slip Ratio Rolling Contact Fatigue Tester”, Graduate Thesis, University of North Dakota.

[31] Voskamp A.P., and Mittemeijer E.J., 1997, “The effect of Changing Microstructure on the Fatigue Behavior During Cyclic Rolling Contact Loading”, Z, Metallkd, 88, pp.310-319.

[32] Dvorak G., Zahui M., Mitton B., “Development of a Sliding Rolling Contact Fatigue Tester”, ASTM International, Journal of ASTM International, Vol. 7, No. 6, June 2010.

[33] ASM International Handbook Committee, “Failure Analysis and Prevention”, ASM Handbook, ASM International, materials park, OH, 2002, Vol 11.

[34] Lundberg G., and Palmgren A., 1947, “Dynamic Capacity of Rolling Bearings”, Acta Polytech. Scand., Mech. Eng. Ser., 1(3), pp.1-52.

[35] Zaretsky E.V.,1994, “Design for Life, Plan for Death”, Mach. Des., 66(15), pp.55-59.

[36] Ioannides E., and Harris T.A., 1985, “A New Fatigue Life Model for Rolling Bearings”, ASME J. Tribol. 107, pp.367-378.

[37] Hanau H., 1965, “New Concepts in Bearing Designs and Applications”, pp. 20-22.

[38] Harris TA et al., “Anti-Skid Bearing”, US Patent #3, 410, 618:1968.

[39] Bowen WL, Bhateja CP., “The Hollow Roller Bearing”, ASME Trans 1980;102 (April):222-8.

[40] Murthy CSC, Rao AR., “Mechanics and Behavior of Hollow Cylindrical Members in Rolling Contact”, Wear 1983;87:287-96.

[41] Barabas S., Fota A., 2011, “Analysis of Hollow Rollers Implementation in Flexible Manufacturing of Large Bearings”, International Journal of Mechanical, Aerospace, Industrial, Mechatronic and Manufacturing Engineering Vol:5, No:8, 2011.

[42] Jadayil W.M.A., Jaber N.M., (2010), "Numerical Prediction of Optimum Hollowness and Material of Hollow Rollers under Combined Loading", Materials and Design 31(2010) 1490-1496.

[43] Spierings Ab, Tarr TL, Wegnere K, "Fatigue Performance of Additive Manufactured Metallic Parts", Rapid Prototyping J 2013:19:88-94.

[44] Pilli H. et al, (2015), "Cost Estimation of Laser Additive Manufacturing of Stainless Steel", 15th Nordic Laser Materials Processing Conference, Nolamp 15,25-27 Autust 2015, Lappeenranta, Finland.

[45] Merklin M., Plettke R., Junker D., Schaub A., and Ahuja B., 2015, "Mechanical Testing of Additive Manufactured Metal Parts", Trans Tech Publications, Switzerland, 2015.

[46] Herzog D., Seyda V., Wycisk E., and Emmelmann C., 2016, "Additive Manufacturing of Metals", Acta Materialia, 117(2016) 371-392.

[47] Luecke W.E., and Slotwinski J.A., 2014, "Mechanical Properties of Austenitic Stainless Steel Made by Additive Manufacturing", Journal of Research of the National Institute of Standards and Technology, Vol. 119 (2014).

[48] Additive Manufacturing Technology, European Power Metallurgy Association, (www.epma.com/am).

[49] Yadollahi A., Shamsaei N., (2017), "Additive Manufacturing of Fatigue Resistant Materials: Challenges and Opportunities", International Journal of Fatigue 89 (2017) 14-31.

[50] Bai J.Y., Fan C.L., Lin S.B., Yang C.L., and Dong B.L., 2017, "Mechanical Properties and Fracture Behaviours of GTA-Additive Manufactured 2219-Al After an Especial Heat Treatment, Journal of Materials Engineering and Performance", 1808 Volume 26(4) April 2017.

[51] Yadollahi A, Shamsaei N, Wells DN, Daniewics SR., "Fatigue Behavior and Failure Analysis of Additive Manufactured Inconel 7018 superalloy" (under preparation).

[52] Want et al. (2004), "The Flattened Brazilian Disc Specimen used for Testing Elastic Modulus, Tensile Strength and Fracture Toughness of Brittle Rocks: Analytical and Numerical Results", Int J Rock Mech Min Sci 41(2):245-253.

[53] ANSYS® Academic Research, Release 16.2, 2016, Help System, Mechanical User Guides, Mesh, ANSYS Inc.

[54] Qin W.J., Guan C.Y., 2014. "An Investigation of Contact Stresses and Crack Initiation in Spur Gears Based on Finite Element Dynamics Analysis", International Journal of Mechanical Sciences 83(2014) 96-103.

[55] Strain Gauge measurement-A tutorial, Application Note 078, National Instruments.

[56] Technical Note TN-505-4, Document No. 11055, Rev. 14-Aug-2014, "Strain Gage Selection: Criteria, Procedures, Recommendations", Vishay Precision Group.

[57] User Guide, SCC-SG Series Strain Gage Modules.

[58] Measuring Strain with Strain gages, National Instruments.

[59] Agilent 34970A Data Acquisition / Switch Unit User Manual.

[60] Agilent 34830A BenchLink Data Logger Pro Software for Agilent 34970A Data Sheet.

[61] Kalpakjian S., "Manufacturing Engineering and Technology", 3rd Ed. Addison-Wesley Publishing Co., 1995.

[62] Deshmukh S., 2014, "Development of Second Generation Rolling Contact Fatigue Tester", Graduate Thesis, University of North Dakota.

[63] Tarn T-J., Chen S-B, Chen X-Q., 2015, "Robotic Welding, Intelligence and Automation", Springer International.

[64] Rockwell Automation, 2013, "PowerFlex® 700S High Performance AC Drive – Phase II Control", Publication 20D-PM001C-EN-P.